



Entwicklung von in vitro Modellen der oberen und unteren Atemwege zum Studium der Aerosolentstehung und der Virusverpackung

Dissertation

zur Erlangung des akademischen Grades

**doctor rerum naturalium
(Dr. rer. nat.)**

von M.Sc. Rasika Murkar

geb. am 20. Februar 1995 in Mumbai, India

genehmigt durch die Fakultät für Verfahrens- und Systemtechnik der Otto-von-Guericke-Universität Magdeburg

Gutachter / innen:

Prof. Dr. rer. biol hum. Heike Walles

Prof. Dr. med. Thorsten Walles

Prof. Dr. Nora Kulak

Promotionskolloquium am 15. April 2025

Eingereicht am :

Bürostempel

Mitglieder des Promotionskomitees:

Vorsitzender: Prof. Dr. Julian Thiele

1. Prof. Dr. rer. biol hum. Heike Walles

2. Prof. Dr. med. Thorsten Walles

3. Prof. Dr. Nora Kulak

Tag des Promotionskolloquiums:

Doktorurkunden ausgehändigt am:

Zusammenfassung

Die Entwicklung physiologisch relevanter 3D *In vitro*-Modelle der menschlichen Atemwege ist aufgrund des komplexen Aufbaus und der sich stark verändernden morphologischen Zusammensetzung sehr schwierig. Die wesentlichen Unterschiede der menschlichen Atemwege werden bedingt durch die variierenden Schichten der unterschiedlichen Zelltypen und der unterschiedlichen Regenerationskapazitäten der oberen, unteren Atemwege und der Alveolen. Diese Komplexität und Variabilität macht die Entwicklung eines biomimetischen *in vitro*-Modells unmöglich. Dies vorliegende Dissertation zielt darauf ab, diese Komplexität in unterschiedlichen Co-Kulturen - Gewebemodellen zu entwickeln und zum Studium der Zell-Zell- und Zell-extrazelluläre Matrix (EZM)-Interaktionen Region-spezifisch - obere Atemwege, untere Atemwege und Alveolar Regionen - einzusetzen.

Ein Schwerpunkt dieser experimentellen Dissertation liegt in der Charakterisierung und vergleichenden Testung unterschiedlicher Trägerstrukturen für den Region-spezifischen Aufbau der Atemwegsmodelle. Basierend auf aktuellen Literaturrecherchen wurden elektrogesponnene Membranen aus biokompatiblen Polymeren wie PCL, PTMC sowie deren Komposit in unterschiedlichen Anteilen, (50:50 und 70:30) und PA hergestellt. Diese Membranen wurden hinsichtlich ihrer mechanischen Eigenschaften charakterisiert, um ihre Eignung als EZM-ähnliche Gerüste für jeden Atembereich zu beurteilen. Diese Charakterisierung der mechanischen Eigenschaften wie Zugfestigkeit und Elastizitätsmodulmessungen ergab, dass PCL:PTMC 50:50 sowie PA ein Gleichgewicht aus Flexibilität und Zugfestigkeit besitzen, das der Elastizität von natürlichem Lungengewebe sehr nahe kommt. Diese Materialeigenschaften machen sie zu vielversprechenden Kandidaten für den Aufbau von Alveolar Modellen. Im Gegensatz dazu wiesen kommerzielle PET-basierte Membranen eine höhere strukturelle Steifigkeit auf. Diese Materialeigenschaft war vorteilhaft für alle Anwendungen, bei denen eine stabile Barriere unerlässlich war; für Alveolargewebemodelle waren sie jedoch ungeeignet.

Der zweite wissenschaftliche Schwerpunkt dieser Dissertation bestand darin, die Zellbesiedlungsstrategien zu optimieren, um die Barriere-Funktion der unterschiedlichen Gewebemodelle physiologischer widerzuspiegeln. Atemwegs Region-spezifische Zellkomponenten wurden ausgewählt, darunter Zelllinien wie Calu-3, A549 für die oberen Atemwegsregionen sowie primäre menschliche Zellen, menschliche Endothelzellen (hEC) und menschliche Atemwegsepithelzellen mit Alveolarepithel Typ 2 (huAEC), um komplexe Co-Kulturen aufzubauen. Zusätzlich wurden menschliche Lungenbiopsien genutzt, um native, aus der menschlichen Lunge gewonnene Fibroblasten, zu isolieren. Die Integration der Fibroblasten aus Lungenbiopsien verbesserte diese Modelle. Diese Verbesserung zeigte sich durch physiologische Zellorganisation und die Umstrukturierung der EZM.

Insgesamt konnte so *in vitro* eine Gewebestruktur aufgebaut werden, die der nativen Lungenarchitektur wesentlich näherkommt. Zwei unterschiedliche Zellbesiedlungsmethoden wurden eingesetzt und den Einfluss dieser auf die Barriere Funktion und Durchlässigkeit (Papp) des resultierenden Gewebes zu untersuchen. Die Verwendung huAEC zeigte eine verbesserte frühe Barriere Integrität auf unterschiedlichen Scaffolds.

Ein weiterer wichtiger Aspekt dieser Arbeit ist die biochemische Charakterisierung, der zellulär in den Gewebemodellen erzeugten, Schleimschicht. Die Charakterisierung von *in vitro* produziertem Mucus (Schleim) ist notwendig, um eine funktionelle Nachahmung des Atemwegsgewebes zu gewährleisten. Bei der Anwendung der Gewebemodelle beispielsweise zum Studium von Virusinteraktionen mit den humanen Atemwegen oder der Aerosolbildung und -einkapselung, kommt es entscheidend auf die physikalischen Eigenschaften wie Oberflächenspannung und Viskosität der Schleimschicht an. Mit einem Rheometer wurden detaillierte rheologische Untersuchungen, einschließlich Oberflächenspannungs- und Viskoelastizitätsanalysen, durchgeführt, um die Stabilität und das Verhalten des Schleims unter Belastung zu beurteilen. In dieser Studie wurden Methoden zur Messung der Oberflächenspannung (ST) der Schleimproben bewertet. Es konnte gezeigt werden, dass die wiederholten zyklischen Messungen stabile und zuverlässige ST-Werte ergaben. Variationen der ST in verschiedenen Umgebungen und Vorbereitungsmethoden unterstreichen die Bedeutung der Feuchtigkeitskontrolle und der Anpassung des Messprotokolls zur Erfassung genauer Schleimeigenschaften. Messungen der relativen Viskosität, die in verschiedenen Umgebungen für Amplituden- und Frequenzdurchlaufanalysen durchgeführt wurden, bestätigten, dass die Schleimschicht scherrverdünnende Eigenschaften aufwies und bei höherer Belastung von einem elastischen zu einem viskosen Verhalten überging. Dies ist ein charakteristisches Verhalten des natürlichen Atemschleims, dass seine Funktion beim Schutz der Epithelschichten unterstützt.

Zusammenfassend konnte in der Dissertation gezeigt werden, dass für die Generierung physiologische Atemwegsmodelle, die Auswahl der Trägermaterialien basierend auf den mechanischen Eigenschaften wie Elastizitätsmodul und Zugfestigkeit getroffen werden muss. Zweitens ist die Auswahl der Zellkomponenten und die Co-kultur für die unterschiedlichen Atemwegsregionen zwingend notwendig. Drittens muss die funktionelle Charakterisierung der Mucusschicht neben den *in vitro*-Modellen durchgeführt werden. Die Mucusproduktion und Barrierefunktion der Region-spezifischen 3D-*in vitro*-Modelle der Atemwege wird in dieser Dissertation in präzisen Protokollen festgehalten. Diese Versuchsbedingung zur Generierung der unterschiedlichen Atemwegsmodelle stellen einen bedeutenden Fortschritt bei der Nachbildung struktureller und funktioneller Komplexitäten menschlicher Atemwege dar. Wichtige Kenngrößen sind die mechanischen Eigen-

schaften der EZM und die zelluläre Heterogenität. Die vorgestellten regions-spezifischen *in vitro*-Modelle, die auf neuartigen synthetischen elektrogesponnenen Polymergerüstmembranen und selektiver Co-Kultur basieren, bieten eine potenzielle Plattform für Anwendungen, insbesondere zur Untersuchung der Aerosolproduktion als Grundlage für das Studium der Virusverkapselung.

Summary

Establishing 3D *in vitro* models for human airway systems exhibits significant challenges, due to the intrinsic heterogeneity and complex cellular composition of respiratory tissues. Different regions in the human respiratory system have diverse cell types, differences in layered structures, and varied regenerative capacities across the upper, lower, and especially alveolar lung. This complicates the creation of biomimetic *in vitro* models. This work is aiming towards addressing these complexities by developing region-specific, co-culture-based models that provide possibilities to replicate better cell-cell and cell-extracellular matrix (ECM) interactions, essential for mimicking the behaviour of distinct areas within the lung, such as the upper airway, lower airway, and alveolar regions.

In this work, one critical challenge was the selection of appropriate scaffold material for biomimetic ECM modelling. Following recent literature reviews, electrospun membranes composed of biocompatible polymers like PCL, PTMC (blended into varied proportions, namely 50:50 and 70:30), and PA were fabricated and characterised with respect to mechanical properties to assess their suitability as ECM-like scaffolds for each respiratory region. Characterisation of the membrane variants for mechanical properties like tensile strength and Young's modulus measurements revealed that the PCL:PTMC 50:50 as well as PA promise to provide a balance of flexibility and tensile strength closely matching the elasticity of native lung tissue, revealing them promising candidates for the dynamic environment of alveolar models. Conversely, standard and commercialised PET-based models exhibit higher structural rigidity, which proved advantageous for static or short-term applications where a stable barrier was essential but inappropriate for alveolar tissue models.

The second vital challenge was to optimise cell seeding strategies to improve barrier function within the models. Tissue region-specific cellular components were selected, including standardised cell lines such as Calu-3 and A549 for upper airway regions, as well as primary human-derived cells, human endothelial cells (hEC), and human airway epithelial cells, including alveolar epithelium type 2 (huAEC), which were used to produce complex co-cultures. Additionally, human lung biopsies were used to isolate native human lung biopsy-derived fibroblasts. The integration of fibroblasts derived from lung biopsies further enhanced these models by promoting layered cell organisation and ECM remodelling, yielding a tissue structure closer to native lung architecture. Two cell seeding sequences were evaluated to examine how cellular arrangement influences permeability (Papp) and tight junction formation. The huAEC-first configuration demonstrated improved early barrier integrity across multiple membrane types, with faster reductions in Papp indicating effective tight junction establishment.

A further critical component of this work involved characterizing the mucus layer generated within these models. Mucus characterisation of *in vitro* airway models is necessary to ensure functional mimicry of respiratory tissue. As an application in further analytical studies such as viral interaction or aerosol formation and encapsulation studies, critically depends on physical properties like surface tension and viscosity of the mucus layer. Detailed rheological assessments, including surface tension and viscoelasticity analyses, were conducted using a rheometer to evaluate the mucus's stability and behaviour under strain. This study evaluated surface tension (ST) measurement methodologies for mucus samples in *in vitro* airway models, demonstrating that repetitive cyclic measurements yield stable and reliable ST values. Variations in ST across different environmental settings and preparation methods underline the importance of humidity control and measurement protocol customisation to capture accurate mucus properties. Relative viscosity measurements explored across varied settings for amplitude and frequency sweep analyses confirmed that the mucus layer exhibited shear-thinning properties, transitioning from elastic to viscous behaviour under higher strains, a characteristic behaviour of native respiratory mucus that supports its function in protecting epithelial layers.

In essence, this thesis will demonstrate ways through which scaffold material selections can be optimised by means of essential mechanical characteristics of elasticity modulus and tensile strength. Secondly, the critical selection of cellular components and cell seeding strategies are presented to accomplish region-specific *in vitro* model generation. And thirdly, the steps of functional characterisation of *in vitro* models as well as, most importantly, mucus using standardised protocols when establishing high-fidelity 3D *in vitro* models of the lung. These models represent a significant step forward in the recreation of structural and functional complexities of human respiratory system regions, based on the mechanical properties of the ECM and cellular heterogeneity. Presented region-specific *in vitro* models based on novel synthetic electrospun polymeric scaffold membranes and selective cell co-culture provide a potential platform for applications, especially to study aerosol production as a basis for virus encapsulation in respiratory research, drug testing, and extended application in Tissue Engineering.

Contents

Zusammenfassung	i
Summary	iv
1 Introduction	1
1.1 Background and Significance	1
1.1.1 Tissue heterogeneity of human respiratory tract	2
1.1.2 Advanced 3D Airway Models: Unlocking Viral Dynamics and Deep Lung Biology	5
1.1.3 Role of Tissue Engineering	6
1.2 Overview of current models and their limitations	8
1.2.1 Advanced scaffold materials and their properties	8
Mechanical properties and thickness	8
Electrospun scaffold materials	9
PCL & PTMC scaffolds:	9
Polyamide scaffolds:	11
Significance of optimized surface coatings	13
1.2.2 Cellular components	14
1.2.3 Rheological and physical properties of mucus / pulmonary surfactant	16
Mucus extraction and characterisation limitations:	16
Physical and rheological characterization	17
Protein characterization	18
1.3 Objectives of Thesis	21
1.3.1 Thesis Approach	23
Selection of appropriate scaffold materials	23
Protein-based coating solution optimization	24
Selection of cellular materials	24
Model characterisation	25
Mucus extraction and characterization	25
2 Materials and Methods	27

2.1	Materials	27
2.1.1	Cell culture materials	27
	Cellular materials	27
	Cells and tissue culture mediums	28
	Supplements for mediums	29
2.1.2	Biological and chemical substances	29
	Enzyme and substrate solutions	32
2.1.3	Reference biomaterials for synthetic scaffold	33
2.1.4	Analytical biological components	33
	Antibody list	33
	Analytical kits	36
	Analytical Solutions and buffers	36
2.1.5	Equipments, Software and Consumables	38
2.2	Methods	41
2.2.1	Scaffold materials	41
	Biological Scaffold material	41
	Production and preparation of synthetic scaffolds	42
	Tensile test of scaffold membrane	43
2.2.2	Isolation, cultivation and characterisation of cells	44
	General cell culture conditions and protocols:	44
	Cell culture of human endothelial cells and human airway epithelial cells	44
	Isolation of pulmonary fibroblasts from human lung biopsy:	46
	Immune fluorescence staining of cells/cell lines	46
2.2.3	Optimisation of region-specific airway models	47
	SIS-muc based models	47
	PET thincert® based models	47
	Establishment of co-culture models with huAEC, fibroblasts, and en- dothelial cells	48
	Electrospun synthetic membrane-based models	51
2.2.4	Histological and functional characterisation	53
	Tissue handling and sectioning	53
	Hematoxylin and Eosin (HE) staining	53
	Alcian Blue (AB) staining	53
	Immunohistochemical staining	54
	Immunofluorescence staining	54
2.2.5	Permeability analysis- FITC dextran assay	55

2.2.6	Protein and mucin content analysis of tissue-derived mucus	57
	Mucus production and isolation	57
	Protein content quantification using Bradford Assay	57
	Westerblot analysis for mucin proteins Muc5AC and Muc5B	58
2.2.7	Physical and rheological methods for mucus characterisation	59
	Surface tension analysis	59
	Viscosity measurement	60
2.2.8	Statistics	62
3	Results	63
3.1	Materials employed as scaffolds	63
3.1.1	Analysis of synthetic polymer-based scaffold membranes	63
3.1.2	Mechanical properties: Tensile strength and Modulus of Elasticity . .	66
3.2	<i>In vitro</i> airway tissue models	68
3.3	Characterisation of <i>in vitro</i> tissue models	69
3.4	Alveolar airway models	73
3.4.1	Alveolar 3D tissue models on PET membrane	73
3.4.2	PCL, PTMC membrane-based <i>in vitro</i> tissue models	75
	Influence of inclusion of native fibroblasts and optimised coating . .	75
3.4.3	PA membrane-based <i>in vitro</i> models	80
3.4.4	Analysis of apparent permeability for electrospun membrane-based tissue models	82
3.5	Characterisation of mucus	87
3.5.1	Visco-elastic behaviour analysis	87
3.5.2	Surface tension analysis for extracted mucus samples	93
4	Publications	97
5	Discussion	100
5.1	3D <i>in vitro</i> airway tissue models	101
5.1.1	Upper airway region:	102
5.1.2	Lower Airway region:	103
5.1.3	Deep lung alveolar region:	104
	Influence of optimised coating solutions in in-vitro tissue models . .	106
	Influence of native fibroblasts on co-culture	107
	Influence of optimised co-culturing strategies	108
5.1.4	Interpretation of scaffold mechanical properties	111
5.2	Standardisation challenges with mucus characterisation methodologies . .	112
5.2.1	Protein quantification and mucin content analysis	112

5.2.2	Physical characterisation methods	113
	Surface tension analysis challenges	113
	Viscoelasticity analysis	114
6	Conclusion	117
6.1	Suitability for <i>in vitro</i> Alveolar Tissue Models Based on Mechanical Properties and Apparent Permeability	119
6.2	Challenges to mucus physical characterization methods	122
7	Future work	124
	Supplementary Figures	127
	Bibliography	129
	Appendix	143
I	List of Abbreviations and Notations	143
II	List of Figures	145
III	List of supplementary figures	147
IV	List of Tables	148
	Declaration of Honor	149
	Declaration on criminal act	150
	List of Publications	151

Introduction

1.1 Background and Significance

Amidst the critical period of viral pandemics, particularly in light of pandemics like COVID-19, pulmonary research inspired in the line of Tissue Engineering has become critically important in viral studies. Understanding the transmission dynamics of airborne viruses has become one of the vital topic in various research groups. Comprehending how airborne viruses spread has emerged as a crucial area of study for numerous research teams. It is well recognized that the respiratory system is the main pathway for many viral airborne diseases, including SARS-CoV-2. The main way that viruses spread was thought to be through droplets and aerosols produced by infected people. Studying these viruses' intricate interactions inside human respiratory tissues as well as their passage via the pulmonary pathway is therefore essential. To create complex human lung models that can replicate this process, in vitro tissue models are crucial [1].

These models are critical for mimicking the human respiratory tract's distinct design, which spans the nasal and tracheo-bronchial airways to the deep alveolar areas. Viral transmission and tissue interaction are influenced by variations in tissue structure, mucus production, and mechanical characteristics such as elasticity and surface tension in these regions[2]. Surfactants and mucus, which cover the respiratory surfaces, are essential for the encapsulation and movement of viruses. The production and stability of virus-laden aerosols are influenced by their rheological characteristics, underscoring the necessity of standardizing methods for examining these characteristics in relation to viral transmission [3].

Comprehending aerosol transmission is essential in examining superspreading situations when little virus particles can traverse extensive distances, hence elevating infection rates. Advanced lung models facilitate the evaluation of these dynamics and provide platforms for testing antiviral treatments and vaccinations, becoming essential instruments for enhancing pandemic preparedness [4]. Given the ongoing global health dangers posed by respiratory viruses, the advancement of human-

relevant *in vitro* systems will be crucial for improving our capacity to respond swiftly and effectively.

1.1.1 Tissue heterogeneity of human respiratory tract

The human respiratory system is a complex system, bifurcated into upper and lower respiratory tracts and characterized by different complex cellular layers, fluids overlaying the cellular layer and forming the barrier to the environment. The upper respiratory tract starts from the nasal cavity to the pharynx and larynx, while the lower respiratory tract comprises of upper lung and lower lung areas. The upper lung area of the trachea, bronchi, and upper bronchioles functions as a gas transport system, while the lower lung area of terminal bronchioles and distal lung alveoli is responsible for air exchange and respiration through the crucial air-blood barrier. Polarised epithelium lining the respiratory tract change tissue architecture and cell types as the airway deepens, i.e., starting from the trachea/bronchi where the epithelium is more pseudo-stratified and prominent cilia presence, bronchioles appear to have cuboidal epithelium. Fig. 1.1 shows the structural differences between upper lung epithelium architecture and lower distal lung epithelium [5].

Upper Airway (Trachea, Bronchus)

The trachea has multilayered ciliated cylindrical epithelium with prominent kinocilia responsible for mucus and airway clearance (as shown in fig. 1.1 (A)). The mucus layer appears to be thicker given the highly frequent mucus-producing goblet cells in the differentiated epithelium in comparison to the lower lung epithelium. Such multilayered epithelium rests on thick lamina propria made of collagen and elastin fibres forming the extracellular matrix (ECM) embedded with immune cells, glands, fibroblasts, and other immune cell types. Similar multilayered ciliated epithelium stacked on top of the smooth muscle layer ECM continues towards the bronchus area. To summarize, upper airway tissue can be distinguished by the main components, like multilayered highly ciliated pseudostratified epithelial cell types, including a higher number of mucus-producing goblet cells and consequently thicker mucus layered on top of the epithelium. The ECM embedded with fibroblasts and other cell types is thicker and can be responsible for overall cellular behaviour, differentiation, and function.

Lower airway (Bronchioles, Terminal Bronchioles, Respiratory Bronchioli)

Descending towards bronchioles, the thicker ECM made of the smooth muscle fibres gets remodelled and no longer is in continuous layered form, as seen in the case of the bronchus, while cartilage and glandular tissues disappear. Here the epithelium becomes a single-layered cylindrical ciliated epithelium, resting over

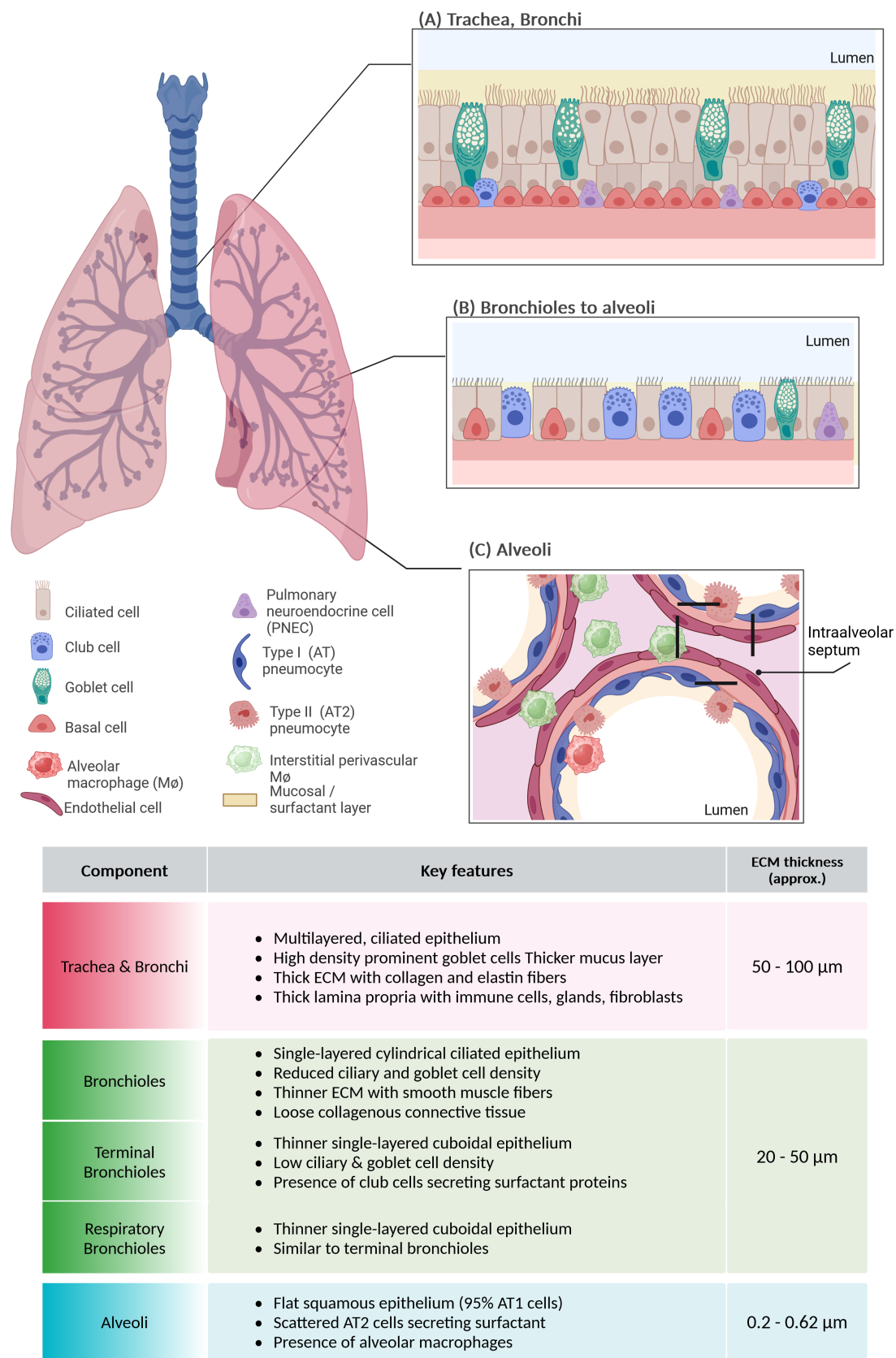


Figure 1.1: Typical tissue architecture for the human respiratory tract

(A) upper respiratory tract with multilayered pseudostratified epithelium and thicker mucus layer and ECM; (B) lower respiratory tract with single-layered columnar epithelium and thinner mucosal layer and ECM; (C) deep lung alveoli network with ultrathin ECM and thinnest surfactant layer. Figure adapted using Biorender.com [6]

the loose collagenous connective tissue layer, while mucus-producing goblet cells are significantly less present than compared to the trachea and bronchus region (as shown in fig. 1.1 (B)). The height of the epithelium layer is greatly reduced in the lower lung area, starting from terminal bronchioles. Terminal bronchioles have single-layered cuboidal epithelium with significantly reduced ciliary density. Epithelial cells increasingly differentiate into club cells responsible for secreting certain surfactant proteins among other lysozymes for the non-specific immune defence, etc. Further down, the respiratory bronchioli are walled with single-layered cuboidal epithelium similar to the terminal bronchiole. To summarise, thinner, remodelled ECM as a result of smooth muscle fibre can be considered one of the main components while developing lower airway tissue models. Besides the single-layered cylindrical epithelium with reduced cilia and goblet cells, it consequently gives rise to a reduced to none mucus lining on top of the epithelium.

Deep lung alveoli

Respiratory bronchioli lead to the alveolar ducts, where they start bifurcating into minute alveolar sacs from a group of alveoli. An alveoli is the basic functional unit of the distal deep lung area. The alveolar sac consists of many grouped alveoli, where neighbouring alveoli just share a single wall known as the intra-alveolar septum. Alveolar epithelium shares an ultra-thin basement membrane (approx. $0.62\ \mu\text{m}$ - $0.2\ \mu\text{m}$) with the endothelial cell layer from the surrounding blood capillaries via the septum [7]. Alveoli perform the crucial role of maintaining air-blood barrier tissue; here the previously thicker ECM is remodelled by fibroblasts to form a thin fibrous network through which blood capillaries pass. As shown in Fig. 1.1 (C), the inner ECM forming the intra-alveolar septum lined by endothelial cells from blood capillaries is overlayed by the ultrathin basement membrane lined by alveolar epithelium on top. Such epithelium is composed of 95 % alveolar type 1 pneumocytes, which form the single-layered flat squamous layer to enable the diffusion of oxygen into the blood and of carbon dioxide into the alveoli via their flat cell body. Distinct cuboidal type 2 pneumocytes are scarcely present, secreting a surfactant layer to maintain crucial surface tension in order to prevent alveolar collapse. The presence of alveolar macrophages in the alveolar epithelium is also found to be crucial in supporting the mitigation, interaction, or removal of virus or dust particles that manage to reach alveoli. These macrophages are able to migrate through the intra-alveolar septum and connect to the lymphatic system of the lungs. To summarise the vital characteristic of deep lung alveoli is the ultra-thin ECM network remodelled by the fibroblasts, which influences the co-culture of epithelial and endothelial cells while maintaining a crucial air-blood barrier at the same time. Besides the epithelium being cuboidal non-ciliated, the scarcely present pneumocytes type 2 responsible

for surfactant production may result in an ultra-thin, layered surfactant layer on top of the epithelium.

1.1.2 Advanced 3D Airway Models: Unlocking Viral Dynamics and Deep Lung Biology

In addition to being a crucial location for gas exchange, the alveolar region also plays a crucial role in the production of virus-laden aerosols during exhalation. Understanding the production of aerosols and how they affect the spread of viruses depends critically on the thin film creation in deep lung alveoli. Aerosols are released into the airways by the rupture and reform of the thin mucus films lining the alveoli. This process, which is fuelled by the mucus's surface tension (ST) and rheological characteristics, produces tiny, virus-encapsulated aerosols that can be released into the atmosphere through coughing or inhaling. Studying this process is crucial for understanding viral propagation, especially during superspreading events when aerosol transmission can result in quickly spreading infections like COVID-19 [3].

Advanced *in vitro* models, especially of the alveolar region, require specific incorporation of both endothelial and epithelial counterparts, along with reproducibility in simulating the distinct mechanical and biological behaviours of the alveolar Secondly, in developing advanced 3D alveolar models for studying viral dynamics, limitation of reproducibility, functional and structural features and human-relevant data generation has been one of many challenges in many research studies [8]. The standardization of scaffold materials that mimic native extracellular matrix (ECM) properties is equally important. These scaffolds provide the structural support necessary for proper cell behaviour and tissue architecture, allowing for the accurate modelling of biological processes such as aerosol generation and viral transport. Scaffolds made from materials like hydrogels, decellularized lung ECM, or synthetic biomaterials must recreate the native lung's mechanical, biological, and physical properties, including ECM thickness and stiffness, which are essential for creating reproducible, human-relevant models [8, 9]. For example, the use of hydrogel-based lung ECM models for studying alveolar dynamics, including viral infections and mucus formation, shows promise but faces challenges in replicating native tissue functionality and ensuring reproducibility [9]. While lung ECM hydrogels derived from decellularized tissues have the potential for advanced alveolar cell attachment and cellular phenotype maintenance, fast changes in mechanical properties and structural stability of the latter badly interfere with consistent modelling of the tissue studied, especially in long-term studies. Besides, while the ECM-derived gels do facilitate some lung-specific functions, maintenance of complex interactions in

mucus formation under viral conditions is one of the important challenges yet to be resolved [8].

Of equal importance is that cellularly relevant materials are employed for the fabrication, such as primary human cells or cell lines, to create physiologically accurate models of tissues. Such models may be biologically more relevant by co-culture of the epithelium and endothelium along with fibroblasts of the lung reproductive cell-cell interaction and tissue dynamics characteristic of the state *in vivo*. Complex co-cultures are just like these, important in replicating this kind of diversified cellular landscape in the alveoli. For sure, these would be imperative in studying viral spread through aerosol encapsulation in the deep lung.

Standardization of scaffold materials and cellular composition is critical in the generation of reproducible models that yield reliable, translatable human data on drug testing and therapeutic development. Further integration of these models with advanced CFD simulations will provide more comprehensive insight into how aerosol formation, transport, and viral load interact as particles travel upward through the respiratory pathway, hence providing insight into how to prevent and manage viral super spread events [4].

1.1.3 Role of Tissue Engineering

Tissue Engineering has revolutionised *in vitro* tissue modelling by providing more realistic models of highly complex human airway systems. Besides, ways like 2D culture, lung-on-chip systems, and organoid culture have added to our knowledge not only about tissue biology but also to the development of *in vitro* systems that can model definite regions of the respiratory tract [10]. Developing 3D *in vitro* models for different airway regions, particularly the deep lung alveoli, is vital for studying respiratory diseases and viral dynamics in a physiologically accurate context. For instance, 3D extracellular matrices (ECM) that replicate the natural structure of lung tissue have been made using hydrogels. Collagen-based hydrogel co-culture systems were created in one study to differentiate airway epithelium under air-liquid interface (ALI) conditions, and they demonstrated notable advancements in simulating the creation of epithelial barriers [11]. Advanced approaches like 3D bioprinting, but also scaffold-based approaches using electrospinning technology, may enable the recreation of the complex architecture of the respiratory system. These models should attempt to reproduce not only the anatomy of the airway but also its mechanical and biochemical environment and then can be applicable for investigating viral transmission, testing medications, and simulating sickness. To

represent the multi-layered complexity of human lung tissue, systems that capture both epithelial and endothelial interactions must be developed for the deep lung, which is the site of gas exchange. Therefore, compared to conventional 2D cultures, these sophisticated models might offer a more accurate depiction of human airway biology, providing insights into the development of respiratory disorders and treatment outcomes.

The selection of essential cell types, co-culture condition optimisation, scaffold selection, and functional validation are important considerations in the creation of these models.

1.2 Overview of current models and their limitations

Despite advancements, existing *in vitro* models still face limitations in replicating the full complexity of human lung tissue. These limitations are categorised based on several factors:

1.2.1 Advanced scaffold materials and their properties

Mechanical properties and thickness

The basal 3D microenvironment of the extracellular matrix is one of the key components in *in vitro* tissue models, which supplies tissue- or region-specific proteins interwoven in collagenous polymer networks for cellular adhesion. This structure is crucial for cell signalling through ECM cell receptors and also houses essential tissue-specific cell types, including subepithelial fibroblasts, endothelial cells, immune cells, and smooth muscle cells, all of which are vital for cell-cell communication [12].

Selection or fabrication of relevant scaffold is one of the crucial aspects given its influence on ECM remodelling and conditioning, cellular and tissue differentiation, cellular attachment, and cell-cell crosstalk. Scaffold interaction with surrounding biological entities as well as the material and the structure may influence cellular and, in the larger context, tissue/organ function. Biomaterials for scaffolds are broadly classified into synthetic and biologically derived materials [13]. Synthetic polymers like PE, PMMA, and PVC as well as natural polymers like collagen, starch, fibrins, etc., are extensively researched because of their attributes of high biocompatibility and bioactivity, as well as mechanical properties including flexibility, etc. [14].

Not only material source but material properties are also seen to influence the cell material interaction through the influence on cellular attachment proliferation and differentiation, for example, porosity, biodegradability, wettability, stiffness, surface roughness, etc.[13]. Many research studies have underscored the importance and influence of mechanical forces and the physical properties of the niche, for example, in stem cell behaviour [15], especially fibre alignment and patterning, which showed a significant role in enhancing cell responses [14]. Among many options for scaffold or ECM substitutes are hydrogels, native ECM, and synthetic biomaterials. Each provides unique advantages, but challenges persist when applied as scaffold material. Application of biocompatible hydrogels or composites using decellularized naive lung ECM promises an innovative technique to mimic the native lung environment [16]. But the limitations concerning differences in, for example, decellularization methods, enzymatic digestion times, and crosslinking

impact mechanical properties and may suggest the lack of mechanical stability required for long-term studies [16, 17]. Developing an ECM-like structure that reflects the native mechanical and biochemical properties of the human lung is crucial, as it influences not only cellular growth but also the function of the tissue [17, 18]. Recent studies have explored hydrogels and solubilised lung ECM in combination with native pulmonary fibroblasts, producing promising outcomes, such as the pseudo-stratification of the epithelium [18, 19]. However, the thinness of the hydrogel ECM remains a limitation, particularly when modelling the deep lung, where ECM thickness varies significantly.

Electrospun scaffold materials

PCL & PTMC scaffolds:

One of the novel scaffold optimisation or modulation studies, such as precision-engineered polymeric nanofibers, has shown promising opportunities to adjust mechanical properties like stiffness and porosity to better mimic *in vivo* environments. Biocompatible polymers like PCL, PLGA, PTMC, and PA are increasingly being explored to enhance cellular adhesion, proliferation, and differentiation, particularly in 3D airway models. These materials not only support the structural formation of the ECM but also influence cell behaviour, tissue formation, and overall model reproducibility [14].

PCL is a popularly known synthetic polymer used in a wide variety of applications known for its biodegradability, structural stability, and mechanical strength [20]. For instance, PCL has provided in many bone Tissue Engineering applications the possibility of tunable mechanical properties, especially in osteogenic differentiation, bone formations, etc [20–22]. PCL, with its ability to provide an optimisation platform via the addition of other composite materials like PLGA, hydroxyapatite (HA), etc., has positively enhanced its application, going from osteogenic towards antibacterial properties with therapeutic potential for alveolar/craniofacial bone regeneration [22]. However, during *in vitro* testing, PCL fibres demonstrated rapid degradation in the presence of enzymatic media [23], leading to increased surface roughness and a reduction in fibre diameter [24]. Additionally, this degradation accelerated changes in Young's modulus and increased crystallinity, which negatively impacted the scaffold's long-term performance [25]. For instance, PCL scaffolds show an increase in crystallinity over time due to polymer recrystallisation, which contributes to an increase in stiffness [26, 27]. In addition to these limitations, it was also seen that higher porosity provided in PCL scaffolds leads to severe loss of weight, molecular weight, and compressive modulus, but also improves cell ingrowth [28].

PTMC is a recently researched biocompatible polymer known for its flexibility and elasticity, making it suitable for applications requiring high elasticity. This implies that it can undergo reversible deformation under stress without permanent damage. PTMC-based membranes have shown potential for lung research with promising co-culture of *in vitro* airway epithelial-endothelial cells given their advantage of flexibility, better mimicking the *in vivo* environments compared to stiff membranes like PET[29]. Moreover, the flexibility provided by PTMC-based membranes may also allow the possibility of cyclic stretch, enabling mechanical stimulation of cells, which is also crucial for mimicking the dynamic environment of the lungs [29, 30].

Pure PTMC was seen to have limited mechanical strength; hence, it is best suited with some reinforcement, typically with PCL, that can enhance its stability [29]. PTMC polymer alone shows low melting point but high flexibility; hence, achieving uniformity in PTMC scaffold thickness is one more challenge to achieve to blend it into a stable scaffold[29]. One of the studies that explored blends of PTMC with block copolymers like PTMC-PCL-PTMC (Polycaprolactone) demonstrated enhancement in the material properties, such as erosion rates and mechanical strength, while remaining suitable for photocrosslinking as well [31].

Blending PCL and PTMC polymers requires more investigation in the direction of scaffolds for tissue models. Not many research studies have explored the wide applicability, but one of the heavily cited studies has put forth the advantages of PCL:PTMC blends providing flexible, elastomeric, and biodegradable networks suitable for Tissue Engineering applications [31]. A study exploring the PTMC blended with PCL in different ratios suggested tuning the mechanical flexibility and degradation properties of the scaffold, providing a balanced combination of mechanical strength and fibre uniformity, although this blend also affects the degradation rate of the scaffold based on molecular weight [32]. For example, a higher PTMC concentration may lead to lower tensile strength but tends to yield softer, more elastic fibres that may support dynamic tissue conditions. In contrast, a greater concentration of PCL improves mechanical stiffness and durability, which could be beneficial for tissues that sustain loads [32]. Despite its potential, the long-term stability of pure PTMC remains an area of ongoing research. Although degradation rates prove challenging in the applicability of these polymers in scaffold-based tissue models, careful blending considerations might impact mechanical properties, tensile strength, flexibility, fibre morphology, and porosity. Thus providing novel synthetic polymer blends highly suited for applications requiring ECM-mimicking membranes in Tissue Engineering.

Table 1.1 below summarises the key characteristics of PCL and PTMC in the context of scaffold development for lung models.

Table 1.1: Qualitative comparison between PCL and PTMC synthetic polymers based on their mechanical properties [6, 33, 34]

Property	PCL	PTMC
Mechanical Strength	Good: high tensile strength and flexibility	Lower : limited load-bearing application
Processing / Fabrication	Easy: electrospinning, solvent casting, etc	Difficult: due to low melting temperature and high flexibility
Biodegradability & degradation rate	Degrades slowly <i>in vivo</i> ; long-term support for tissue regeneration application. But may hinder its application, requiring rapid tissue integration or replacement	Degraded more rapidly, suited for drug release-like applications <i>in vivo</i>
Hydrophobicity	Hydrophobic: surface modifications (specialized coatings) necessary for improved biocompatibility	Similar to PCL
Elasticity & Flexibility	Limited elasticity: unsuitable for dynamic tissue engineering applications, but flexible	Highly flexible and good elasticity

Polyamide scaffolds:

Application of electrospun polyamide scaffolds in lung Tissue Engineering has been a subject of ongoing research. PA scaffolds are known to be able to replicate key aspects of the extracellular matrix, such as a high surface area to volume ratio, tunable porosity, and significant mechanical strengths. In one of the research studies, polyamide-6 was demonstrated as a promising candidate for mimicking the ECM of specific tissues [35]. In the study done by Zhuravleva et al. (2019), PA6 was employed to replicate oesophageal ECM properties and showed that PA6 was able to support mesenchymal stromal cell proliferation, along with mechanical stability. This shows that using PA6 can enable tuning the architecture and mechanical properties of polyamide scaffolds, making them interesting subjects to be used for replicating various tissue environments [36].

Scaffold generated using PA also showed formations of porous structures that allow for essential functions like nutrient and oxygen diffusion, waste removal, and vascularization[37]. However, these scaffolds have limitations when it comes to

allowing cell infiltration across multiple layers of the scaffold. Hence, additional modifications like altering fibre diameters, introducing pore formers, or blending with other suitable biocompatible polymer variants may prove helpful for investigating scaffold permeability and improving their application in complex tissue models [38]. Furthermore, PA has also shown mechanical robustness in one of the application studies for tissues like the oesophagus [35]. This is especially beneficial for tissues that are subjected to mechanical stress, such as human airway tissues.

In a recent study done by Weigel et al., polyamide nanofibers showed versatility for their use across multiple tissue types like skin, bone, and lung [36]. Here, fully synthetic 3D PA scaffolds were designed in order to replace animal-derived materials for stromal tissues, specifically in multilayered skin regeneration. The fibrous structure of PA scaffolds provided the perfect conditions for skin cells to attach and form layers. According to them, this synthetic method provided an added advantage by preventing immunological reactions linked to scaffolds generated from animals and also may be able to address ethical issues regarding animal-derived materials [36]. The challenge persists in creating a 3D scaffold with high porosity, and mechanical stability is crucial [39]. In the above-mentioned study, polyamide scaffolds used to replicate the ECM for *in vitro* co-culture systems demonstrated their ability to support the growth of multiple cell types, like fibroblasts and endothelial cells [36]. Lung Tissue Engineering requires scaffolds with specific features, like flexibility, tensile strength, region-specific elasticity, fine-tuned porosity, and compatibility with the dynamic nature of lung expansion and contraction. Polyamide scaffolds' with their strong tensile strength might also be useful for building reliable alveolar epithelium models needing a strong barrier but with the necessary flexibility and elasticity modulus. But the limitations, like the difficulties of managing pore size and scaffold degradation, also need to be addressed, particularly when trying to represent more intricate tissues like the lung.

Decellularized native ECM hydrogels do provide a biomimetic environment, yet it is often difficult to source standardised methods, along with the limitations regarding tunable stiffness and thickness. Synthetic materials like PCL, PTMC, and PA offer customisable mechanical properties, but they sometimes fail to replicate the necessary biological cues alone. Achieving the correct ECM thickness and elasticity remains a key challenge, as these properties are essential for creating functional, reproducible models that reflect human lung behaviour [1]. While electrospun polymer-based scaffolds like pure PCL and PTMC offer substantial advantages in terms of mechanical strength and structural stability, challenges related to biodegradability and cell attachment must be addressed for their optimal use in lung models. Ongoing research into polymer blending and surface modifications

continues to improve the flexibility and biocompatibility of PA scaffolds, making them increasingly viable for developing advanced 3D *in vitro* lung models [35, 36, 38]

Significance of optimized surface coatings

The second vital characteristic driving the cell-material interaction is surface protein adsorption, which is driven by the wettability of the surface of the particular biomaterial [13]. Surface characteristics such as hydrophilicity, protein adsorption, and roughness are also critical in determining cell behaviour. Properties such as hydrophilicity or hydrophobicity of scaffold membranes influence the wettability, which in turn modulates the protein adsorption on the membrane surface. Since protein adsorption is one of the primary cues for cellular adhesion, it will in turn impact cell attachment, proliferation, differentiation, and finally survival [13, 40]. For example, studies using polycaprolactone (PCL) and PLGA-based scaffolds have shown that varying stiffness can affect mesenchymal stem cell (MSC) differentiation, leading to optimised tissue regeneration [14]. Various studies have suggested hydrophilic surfaces absorbing water-soluble proteins may support a favourable environment for cell proliferation [41]. Proteins have a higher affinity to adsorb more strongly to hydrophobic surfaces than to hydrophilic surfaces, whereas hydrophobic surfaces lead to protein unfolding, potentially causing cellular stress [13, 40].

The above findings hence suggest that by optimising scaffold coatings effectively with essential proteins, one can enable significant improvements in the maturation of co-cultures, yielding more physiologically relevant *in vitro* models for studying tissue function and disease processes. This may also in turn help in improving cell co-culture systems, particularly in promoting tissue maturation in 3D models like the alveolar co-culture of endothelial and epithelial cells. Different coating materials, such as gelatin, VEGF-165, fibronectin, collagen I, and bovine serum albumin (BSA), offer unique advantages. This includes enhancing cell-scaffold interactions and promoting cell adhesion, proliferation, and differentiation. For instance, gelatin coatings can increase hydrophilicity and support cellular attachment; collagen I provide structural support critical for cellular proliferation. VEGF-165 promotes angiogenesis, improving endothelial cell function, especially in vascularised tissues, making it a vital component in co-culture models requiring vascularization [29]. These coatings not only mimic essential components of the ECM but also provide biological cues that guide cell behaviour. The mechanical properties of the scaffold, such as stiffness and surface roughness, significantly influence cell attachment and function.

Therefore, the use of these coating solutions in 3D scaffolds is not only crucial for enhancing cell survival but also for promoting functional tissue development, especially in complex systems such as the alveolar environment.

1.2.2 Cellular components

Selecting the right cellular components is one of the above-mentioned crucial aspects while developing 3D *in vitro* airway models, particularly when simulating region-specific tissues, which possess challenges with their constant regeneration as well as region-specific functional distinction.

Human airway models employing human stem cells and also iPSCs have been widely researched. But also demonstrated limitations, especially in achieving reproducible and biomimetic models. Nevertheless, human iPSCs have shown potential for directed differentiation into airway basal cells in modelling airway diseases, or for instance, iPSC-derived airway organoids, showing feasibility for genetic disease modelling, etc. [42, 43]. Organoids, derived from stem cells, present a promising alternative due to their ability to self-organise into structures that mimic the architecture of lung tissue. These systems offer better physiological relevance but can be limited by issues related to scalability and batch-to-batch consistency [15]. Furthermore, combining organoids with precision-engineered niches and advanced scaffold materials like electrospun nanofibers has been shown to improve tissue formation and cellular differentiation, providing more reliable models for studying airway biology [14, 29].

In vitro airway models, using iPSC-derived alveolar epithelial cells, are indeed advantageous for patient-specific therapies. However, limitations such as the difficulty of large-scale production and functional differentiation persist. iPSCs have also shown promising differentiation into alveolar epithelial type 2 (AT2) cells, which repopulated lung extracellular matrix scaffolds [44]. Upon further characterisation, these iPSC-derived cells displayed markers characteristic of mature lung epithelial cells. But faced limitations towards their applicability for clinical use [44]. Despite many advancements, iPSC-derived models still face challenges in efficiency and reproducibility and require further investigations [45–47]. Moreover, iPSC models can be affected by donor differences, genetic stability, and experimental variability, which can confound reproducible disease modelling [46, 47].

Immortalised or genetically modified cell lines are commonly used to build *in vitro* tissue models due to their reproducibility and ease of culture. They often lack the complexity necessary to fully replicate human tissue functions. For instance, widely used Calu-3 and A549 lung epithelial cell lines for models of upper and lower airways

do provide valuable insights into respiratory barrier function and drug permeability. Calu-3 cells, which are able to simulate bronchial epithelial barriers, demonstrate robust barrier properties but may tend to overexpress tight junction proteins [48]. Calu-3 cells also provide a polarised epithelial structure and mucin production, which makes them suitable candidates for studying respiratory infections, e.g., influenza [49, 50]. Whereas, A549 cells, representing alveolar cells, exhibit higher permeability and lack of sufficient tight junction formation, making them unsuitable for certain permeability studies compared to primary human epithelial cells [51].

However, advanced co-culture models developed were frequently limited to the upper-airway region, combining Calu-3 cells, or the lower airway region, combining A549 cells. But when combined with other cell types, such as macrophages or dendritic cells, they do promise to offer realism in lung studies [52]. For more sophisticated and crucial airway regions, such as alveolar tissues, the use of such cell lines may not fully replicate the integrity of alveolar barriers [52]. In contrast, the probable best option would be to explore primary cells from human lung biopsies that are able to retain tighter epithelial integrity and a more accurate response to environmental agents than either cell line alone. The inclusion of co-cultures involving epithelial, endothelial, and fibroblast cells has been shown to improve the biological relevance of these models [52]. For instance, lung fibroblasts from human biopsies play a critical role in enhancing the differentiation and functionality of co-cultured epithelial and endothelial cells, leading to more physiologically accurate tissue models. Again, the challenges for long-term culture condition optimisations still need to be addressed with the primary cells, as seen with primary alveolar epithelial cells (hAEPs) [12, 52].

1.2.3 Rheological and physical properties of mucus / pulmonary surfactant

Mucus present as a layering lubricant lining the respiratory tract is a critical functional aspect, playing an essential role in protecting the respiratory tract and influencing viral transmission [49, 53]. This makes it one of the necessary components for characterising advanced 3D airway models. Mucus acts as a physical barrier against foreign particles by trapping pathogens and particulate matter and facilitating their clearance [54, 55]. Many studies have underscored the importance of the rheological characterisation of mucus for understanding its physiology, disease pathology, and development of drug delivery systems for mucosal surfaces [55].

In the lower airways, particularly in the alveolar regions, thin surfactant lining has many crucial functions in addition to maintaining airway hygiene. It is responsible for stabilising the air-exposed interface to prevent alveolar collapse during respiratory mechanics by forming interfacial films at the air-water interface and modulating its physical properties, for example, surface tension [56]. It is central to the formation of thin films in the alveoli, which are responsible for aerosol generation, a key process in the spread of airborne viruses. Production and characterisation of synthetic pulmonary surfactants or mucus mimetics have been discussed recently [57]. Application of such systems as mucus mimetics to mimic the aerosol generation process is crucial to attaining a balance of surface elastic behaviour and surface viscous behaviour [58]. To accurately model the thin film rupture to study the aerosol generation in conjunction with *in vitro* tissue systems, it is hence a challenge to replicate the varying physical properties of mucus, such as viscosity and surface tension, which differ across regions of the airway [59]. Rheological as well as biochemical characterisation of the mucus formed using advanced co-culture airway tissue models is the first step necessary to move towards more sophisticated tissue modelling approaches. This would advance our understanding of the interaction between inhaled droplets or aerosols that may contain viral particles and the lung's thin liquid lining after an aerosol lands on its surface, as well as aerosol generation [58].

Mucus extraction and characterisation limitations:

Nowadays, artificial and synthetic mucus models are being explored using polymer-based techniques [57]. Complex mucins make up the important components present in the respiratory mucus, along with the presence of other glycoproteins. Mucin structure plays a crucial role in mucus's mechanical and biochemical properties, which are essential for its diverse physiological roles. Many research studies

still argue over the possibility of synthetic surfactant's ability to completely replicate the properties of natural mucus [60]. Synthetic surfactants or mucus, for instance, Human Lactobacillus Biosurfactants or simplified phospholipid mixtures, etc., have demonstrated promising results in terms of rheological properties and drug delivery but often fall short in mimicking adhesive properties and complex protein interactions [61, 62]. In contrast, applying sophisticated biomimetic tissue models, with their ability to generate functional mucus with necessary mucins, may not only help better recapitulate the *in vivo* microenvironment but also open the platform, allowing for the more accurate understanding of cell interactions within tissues and organs [63–65]. To attain reproducible and standardisable data against human tissue models, it is necessary here to explore efficient methodologies for mucus extraction and characterization. A range of techniques has been employed to study its rheological properties like viscosity, elasticity, and surface tension, which are critical for understanding how mucus behaves under physiological conditions, especially with its protective functions in the airway and its role in pathogen encapsulation and aerosol formation.

A generalised approach for mucus extraction from *in vitro* tissue models includes apical PBS washes in air-liquid interface (ALI) cultures, ensuring minimal contamination and maintaining sample integrity for subsequent analysis. However, forthcoming limitations to this process can include incomplete mucin removal or the alteration of mucus properties during collection. Hence, making it necessary for standardised protocols essential for reliable data.

Physical and rheological characterization

Mucus is categorised as a non-newtonian fluid at the macroscale, while it can be regarded as a low-viscosity fluid at the nanoscale [55]. The importance of understanding mucus physiology concerning disease pathology or in drug delivery systems cannot be neglected [55]. In the research work done by Jory et. al. (2022), they have finally reinstated the possibility of characterising rheological properties of mucus derived from human bronchial epithelial ALI cultures [66]. This pointed to the dual solid-fluid nature of mucus, found in their rheological analysis using a rheometer with a cone/plate geometry [66]. This provides a nice basis for macro-rheological characterisation of mucus samples generated from *in vitro* tissue models. Cone-and-plate viscometers and particle tracking microrheology are commonly used to analyse the bulk viscosity and microviscosity, respectively [66]. These methods reveal how mucus viscosity changes with shear forces, which is crucial for understanding mucus behaviour during respiratory processes, showing its complex flow behaviour through the entire respiratory tract [67, 68].

Another essential property of mucus or pulmonary surfactant is its surface tension, which becomes crucial to maintain, for example, in order to avoid alveolar collapse. Surface tension impacts the stability of mucus films and their role in aerosol formation. The surface tension of the mucus/pulmonary surfactant is known to be dependent on various factors such as mucus hydration, mucin concentration, and surfactant presence, directly influencing how thin films of mucus form and rupture. The surface tension of pulmonary surfactant is additionally affected by the presence or absence of proteins such as SFTP-C or SFTP-B [69, 70]. In contrast to the available detailed physical characterisation of mucus models like hydrogels or mucus mimetics, the characterisation of mucus samples generated from advanced co-culture tissue models may provide a better understanding of the mucus behaviour.

Protein characterization

Characterising mucus substantially, especially from *in vitro* models aimed to replicate lung environments, is one crucial step towards understanding various pathways, including lung diseases, and in turn, developing effective treatments.

For instance, models of engineered synthetic mucus demonstrated the importance of replicating the viscoelastic properties of native mucus collected from asthma patients [71]. The study also showed how altered mucin composition can impact mucus transport and its ability to act as a barrier against pathogens like the influenza virus [71]. The growing research community is now focusing on creating biomimetic models as well as building systematic characterisation methods to generate human-relevant data that can then be applied for drug testing and disease modelling robust situations like those of SARS-CoV-2 pandemic situations.

Mucins form the principal components found in mucus or pulmonary surfactants that are also known to modulate the mucus's physical as well as rheological properties [69, 70]. This makes it critical to quantify and characterise the mucin components found in the mucus samples along with the *in vitro* tissue models. Standard protein analysis techniques like SDS-PAGE gel electrophoresis and Western blotting, which separate proteins based on molecular weight, may challenge to characterise these mucins, which are heavily glycosylated and possess a large molecular weight. Primary mucins found in human respiratory mucus, Muc5AC and Muc5B, with their large size and viscosity, made it difficult to achieve sharp separation due to their high molecular weight in SDS-PAGE [72]. In western blot analysis, it is very likely to achieve incomplete transfer of mucins, hence reducing detection efficiency [73]. Many other limitations, including smearing and poor resolution iSDS-PAGE, especially for heavily glycosylated mucins like MUC7, or poor antibody binding in

cases of excessive glycan presence, may also cause inaccurate quantification [74, 75], hence underscoring the need for refined characterisation approaches.

The scientific literature lacks comprehensive methods for characterising mucus, particularly when it comes to differentiating between mucus-produced *in vitro* and native samples. Generating biosimilar mucus is of crucial importance in studies of drug permeations as well as viral interaction formations, but such mucin solutions often fail to capture the complex biochemistry and nanostructure of native mucus [76]. Advanced methods, such as combining rheology with particle tracking microrheology, may provide insights into the heterogeneity of mucus [55, 66, 77].

Mucus mimicking hydrogel models demonstrate significant advancements by mimicking the protective and dynamic properties of natural mucus, especially in viral trapping and cell protection [57]. These hydrogels promise to create a scalable, anionic barrier that captures pathogens, enhancing their application in tissue models. However, in dynamic environments like lungs, further investigation is necessary on the long-term stability and mechanical optimisation of this hydrogel. Hence, refining biochemical and rheological properties remains a challenge for accurate *in vitro* simulations.

Despite advancements in the characterisation methodologies, mucus characterisation from both *in vitro* and native samples is far from perfect. As pointed out in various studies, careful control of experimental conditions is necessary to achieve reproducible rheological data, particularly regarding temperature, humidity, and evaporation during testing of cystic fibrosis sputum samples [66, 78].

Furthermore, mucus characterisation performed from *in vitro* tissue-derived mucus samples still may face donor-data variability, in addition to the choice of scaffold and cellular materials used in these models developed by Jory et. al. [66]. The models developed using scaffolds like nucleopore transwell membranes and biopsy-derived cellular components lacking complex co-culture may face challenges to closely mimic *in vivo* tissue architecture [66], making further optimisations necessary. Scaffold material characteristics like hydrophilicity and mechanical stiffness are known to influence cell-cell and cell-matrix interactions, which may further modulate mucus constitution as well as formation [13]. Characterisation data generated for mucus properties from these optimised models may help for advanced modelling of mucus flow characteristics using computational fluid dynamics (CFD) simulations. Using CFD may also help to understand the thin film formation, rupture, transport, and behaviour of aerosols within the respiratory system, offering deeper insights into how viruses like SARS-CoV-2 propagate in the airways [4].

In conclusion, developing effective 3D *in vitro* models of the airway with an ability to replicate functional outputs like mucus and surfactant production requires crucial scrutiny with the choice of cellular materials, scaffold materials with their physical and mechanical properties, and standardisable and reproducible methods integration for both mucus as well as tissue models. One singular model construct is deemed insufficient for diverse regions of the human respiratory system, making it necessary for these models to represent the unique cellular and functional characteristics of different airway regions, from the upper airway to the deep lung alveoli, which may finally help provide accurate insights into respiratory disease mechanisms, viral transmission, and potential therapeutic interventions.

1.3 Objectives of Thesis

The overall aim of this thesis is the establishment of new, standardised, and reproducible methods for advanced *in vitro* airway models, in particular deep lung tissue equivalents, by exploring scaffold varieties from synthetic, polymer-based electrospinning techniques. Such optimised *in vitro* models were built with a broader aim in order to study virus infection on human tissue models and the influence of mucus tangible properties on aerosol generation and virus encapsulation and transport. One of the main tasks was focused on the optimisation of co-culture models of the deep lung alveoli tissue with the aim to enable, in the near future, such models to study aerosol generation and virus encapsulation. These models try to overcome shortcomings of the existing systems through the effective recapitulation of morphological and functional heterogeneity of the lung, considering the dependency on the properties of ECM/scaffold-co-cultured cellular biomaterials. 3D *in vitro* models should be developed for all regions, including the deep lung alveoli; the complex and heterogeneous structure of the lung requires region-specific modelling if one is to understand its response to infections, drug delivery, and tissue regeneration. For example, while the upper airway functions mainly as a barrier to prevent the inhalation of pathogens, the deep alveoli perform gas exchange and, therefore, remain highly vulnerable to viral infections like SARS-CoV-2. It is only by accurately modelling such region-specific differences that a detailed study of such varied responses can be done, and they further effective simulation of drug delivery.

In this study, the objective was to analyse the following research questions:

- Why are advanced *in vitro* models crucial for studying human airway biology?
- Why is it necessary to develop 3D *in vitro* model of different airway regions (including deep lung alveolar)?
- Which biological components or functions (barrier, etc.) are important for which study: infection, drug application, regeneration?
- How can we characterise the function of the models: characterisation of scaffolds and mechanical properties; characterisation of tissue models using stainings and other assays?
- Why is it important to evaluate the influence of co-culture of different primary cells and the scaffold properties on the function of different airway models? To investigate that cellular co-culture of primary/stem cells or cell lines has a higher influence on the function of the airway tissue models alongside applied scaffolds.

Advance *in vitro* region-specific models that can generate human-specific data are increasingly becoming significant research topics. This is with an aim for not only studying the human airway but also in infection studies or aerosol-mediated drug efficacy assessments, etc. Here, barrier formation and mucus production are two of the fundamental biological components, critical to research. For example, in infection studies, a strong epithelial barrier serves as a robust defence against pathogen invasion, whereas mucus production is central to viral transmission studies due to its impact on aerosol generation and viral particle encapsulation. Essential extracellular matrix (ECM) properties, such as thickness, tensile strength, and porosity, significantly affect both infection studies and tissue regeneration models by influencing cell behaviour and tissue stability.

The characterisation of scaffolds is crucial for assessing the functionality and reliability of these models. Mechanical properties of the scaffold, such as stiffness and elasticity, directly affect cellular differentiation and tissue development. Tissue characterisation methods, such as cell-specific staining and mucus production (alcian blue staining), as well as functional assays (e.g., apparent permeability via FITC-dextran assay), are used to assess barrier integrity and the tissue's ability to perform *in vivo* functions, such as pathogen prevention.

Secondly, evaluating the impact of co-cultures of primary cells, such as epithelial, endothelial, and fibroblast cells, is essential, as co-cultures closely mimic the native lung environment. Co-culture systems support complex cellular interactions, facilitating accurate tissue maturation and function. Recent studies suggest that combining co-cultures with biomimetic scaffold properties enhances physiological relevance, allowing for a more accurate representation of airway biological processes.

Finally, persistent challenge in infection or viral transmission/interaction studies with airway *in vitro* models involves optimising methodologies for physiological mucus generation, extraction, and characterization. Physical and rheological properties of mucus largely influence the mucosal lining's function. Understanding mucus's role in respiratory defence mechanisms and viral transmission is essential for developing realistic *in vitro* lung models. Such models simulate these properties over time, enhancing their ability to replicate *in vivo* behaviour and generating valuable data for respiratory disease research. Among our objectives was to investigate dependencies on properties like surface tension and viscoelasticity that affect thin film formation and aerosol generation in deep lung alveoli and to optimise methodologies for effective mucus extraction. Protein quantification and mucin characterisation are also vital steps in characterising mucus, specifically identifying Muc5B and Muc5AC mucins present in lung tissue.

1.3.1 Thesis Approach

The aim of this study is to create and optimise functional *in vitro* lung models that mimic the structural and functional differences in the human respiratory system. To do this, we focused on selecting and optimising scaffold materials, considering different key factors. The scaffold materials were carefully selected and optimised based on their physical properties (stiffness, thickness) and their ability to support cell attachment and differentiation. In this study, both biologically derived and synthetic scaffolds were evaluated for their suitability across different regions of the lung, from the upper airway to the deep lung alveoli, such as stiffness, cell attachment, and scaffold thickness. These properties were chosen to ensure the scaffolds could replicate the basement membrane and provide a suitable environment for cell differentiation and tissue formation, particularly for upper and lower airway models.

Selection of appropriate scaffold materials

In this research, we explored two main categories of scaffold types:

Small Intestinal Submucosa (SIS-muc):

A biologically derived scaffold was chosen for upper airway models due to its natural ECM-like properties. Its decellularized structure mimics the ECM found in tracheo-bronchial tissues, providing a supportive environment for epithelial and fibroblast co-cultures.

PET (Polyethylene Terephthalate) Membranes (Thincerts®):

Widely used in Tissue Engineering, PET membranes are known for their stiff structure, controlled pore size, and widespread use in supporting co-cultures on both sides of the membrane. PET (0.4 μm pore size) was used as a standard comparison due to its established role in lung models, particularly in studies requiring barrier formation and permeability assessment. PET's thin structure (22 μm) allowed for optimal cell-to-cell interaction, making it a benchmark for scaffold performance.

Synthetic polymers (PCL, PTMC and PA):

Novel fibre-based scaffolds were fabricated through electrospinning, incorporating three different primary polymers: Poly(ϵ -caprolactone) (PCL), poly-trimethylene carbonate (PTMC), and polyamide [14, 29, 36, 79]. These biomaterials were chosen for their established biocompatibility and mechanical properties. We hypothesise that combining these two polymers could provide a versatile platform for creating thin, flexible scaffolds tailored to different regions of the respiratory tract, effectively

addressing the specific mechanical and biological requirements of Lung Tissue Engineering.

PCL and PTMC were electrospun to form scaffolds with tunable mechanical properties, biodegradability, and flexibility. These materials, upon fine-tuning, may help to develop thin, porous scaffolds for deep lung alveoli models, where a delicate balance between stability and degradation is necessary. Blending PCL and PTMC in different ratios (70:30 and 50:50) allowed for the creation of scaffolds that could mimic the ultra-thin basement membrane required for alveolar co-culture systems. Similarly, electrospun polyamide scaffolds, as generously discussed for their robust mechanical strength, flexibility, and ability to provide a large surface area for cellular attachment and tissue growth, were also selected for tissue model development for the alveolar airway region.

The PA polymer-based membrane was also obtained using the electrospinning process. Proven application of PA scaffolds for *in vitro* alveolar tissue models as well as the synthetic, flexible, and porous properties of PA make it a viable choice to replicate the structure of lung tissues. Hence this was used for creating a scaffold that may enable respiratory cell adherence, growth, and oxygen exchange. We believe that the PA scaffold's biocompatibility and ability to support organised, layered cell structures are particularly useful for modelling alveolar tissue, providing a controlled framework for studying respiratory diseases and drug responses.

Protein-based coating solution optimization

To further optimise cell attachment and functionality, various coating solutions (e.g., human plasma fibronectin, collagen 1, gelatin, VEGF-165) were applied to the scaffolds. These solutions enhanced cell adherence and differentiation, especially in synthetic scaffolds, by mimicking the biochemical environment of the ECM. The performance of these materials was compared with PET membranes to assess their ability to support tissue models.

Selection of cellular materials

Furthermore, lung location-specific cell types were utilised, including cell lines such as Calu3 and A549, which are popularly used in *in vitro* lung test systems widely to build upper lung area *in vitro* models for tracheobronchial regions. Given the requirement of the thickness of the ECM for tissues from the upper lung area, SIS-muc as well as PET were tested for suitable scaffold material for building functional co-culture *in vitro* models as explained in the methods section. Given the various limiting factors posed by the use of cell lines, primary human cells were employed to

design lower lung tissue models. One of the challenges is to model deep lung alveoli tissue models. The influence of endothelial cells and smooth muscle cells in Tissue Engineering in particular for vascularised tissues is significantly highlighted in various studies [80]. Their potential to form functional vascular networks cannot be neglected; moreover, may enhance the cell-cell communication with neighbouring niche components for survival and integration of the engineered tissue models. Our approach for developing a 3D model for human lung alveoli culture conditions was modulated to establish a co-culture between primary human alveolar epithelial cells (huAELVi) obtained from Inscreenex and primary endothelial cells, as well as the influence of primary lung fibroblasts in a triple culture set up to observe the influence of fibroblast remodelling of the ECM.

Model characterisation

Model characterisation in this study included analysing electrospun membranes made from blends of PCL:PTMC (in ratios of 50:50 and 70:30) as well as PA scaffolds. Scanning Electron Microscopy (SEM) was employed to evaluate the scaffold structure, focusing on fibre diameter, alignment, and surface morphology, all of which directly influence scaffold porosity and cell interaction. SEM imaging provided insights into how these structural characteristics impact cell attachment, migration, and nutrient exchange, critical for replicating the extracellular matrix (ECM) and supporting tissue-specific growth [36].

Mechanical characterization through tensile strength and Young's modulus tests on these cell-free electrospun membranes identified crucial properties that must be optimized to align scaffold mechanics with the complex, heterogeneous ECM of native lung tissue. Matching the mechanical properties of the scaffold to those of the native ECM helps to ensure compatibility and functionality under physiological conditions, a key factor for dynamic tissues like the lung.

Functional assays, including the FITC-dextran permeability assay, assessed the barrier integrity of the tissue models. This assay measures the diffusion rate of FITC-labelled dextran across the membrane, indicating how effectively the scaffold supports barrier functions, such as selective transport and tight junction formation. These insights are essential for modelling the barrier properties of respiratory and other epithelial tissues *in vitro*.

Mucus extraction and characterization

A range of methodologies were explored for efficient mucus extraction from the tissue models and their characterisation for rheological viscoelasticity properties as

well as surface tension of the mucus. The methodologies explored in this study for mucus extraction and characterisation were carefully optimised to analyse its physical and biochemical properties. For assessing surface tension, a force tensiometer was used at multiple time points across the lifespan of the tissue model. This approach allows evaluating changes in surface tension over time, offering insights into how mucus properties evolve within the model.

Rheological properties, specifically viscoelasticity, were analysed using a rheometer. The rheometry parameters were optimised to capture mucus viscosity and elasticity accurately, essential for understanding the mechanical resilience of mucus produced by the tissue model. These measurements help relate the functional properties of *in vitro* mucus to physiological mucus, which is vital for creating realistic respiratory models.

Methods for protein quantification and characterisation were employed to evaluate mucus composition. Protein content in the mucus samples was initially measured using the Coomassie Bradford (BCA) assay, which quantifies total protein levels. SDS-PAGE gel electrophoresis was then used for the effective separation of proteins, followed by Western blotting to detect specific mucins, Muc5AC and Muc5B. We performed this analysis to precisely identify and quantify key mucins, essential components of respiratory mucus, further validating the physiological relevance of the tissue model.

These methodologies collectively ensure a comprehensive understanding of the biochemical and physical properties of mucus produced by the *in vitro* models, thereby reinforcing the model's applicability for respiratory studies.

Materials and Methods

The materials utilised throughout this research are systematically summarized in the tables presented in the following sections. Each table provides a comprehensive list of all components integral to the experimental workflow. Categorically arranged tables include information on specific cell lines, essential mediums and supplements. This is followed by the list for biological and chemical substances, and enzyme and substrate solutions. Used reference biomaterials materials are listed separately. The section for analytical biological components includes the list of all antibodies used, including the kit specifications as well as detailed compositions for the reagents employed in analytical detection methods. Finally, a detailed list of lab equipment, devices, software and consumables is specified along with necessary specifications. The methods section that follows is designed to facilitate the traceability and reproducibility of all procedures developed and analyses conducted within this study. Each method has been carefully described to allow for consistent application and verification by other researchers in the field.

2.1 Materials

2.1.1 Cell culture materials

Cellular materials

The following table 2.1 lists the primary cells and cell lines along with their detailed descriptions including specification, ethical vote consent (wherever necessary), provider or manufacturer information, and specific handling conditions to ensure precise replication.

Table 2.1: Tissue & cellular materials

Product	Specification	Manufacturer / Provider	City / Country
Primary human dermal fibroblasts	Local ethics committee of the University of Wuerzburg (182/10)	University clinic Wuerzburg	Wuerzburg, Germany
human Endothelial cells	Local ethics committee of the University of Wuerzburg (182/10)	University clinic Wuerzburg	Wuerzburg, Germany
human Airway epithelial cells	(INS-CI-1015) resembling the alveolar type 1 cell type	InScreenex GmbH,	Braunschweig, Germany
human Lung biopsy fibroblasts	Lung resections obtained under Ethical vote 163/17	Lung resections from University Hospital Magdeburg, utilized for inhouse fibroblast isolation	Magdeburg, Germany
Calu-3	Human adenocarcinoma cell line	American Type Culture Collection (ATCC), Manassas, VA, USA obtained from University clinic Wuerzburg	Wuerzburg, Germany
A549	Human adenocarcinoma cell line AT2 like	DSMZ, EGFR wild-type, KRAS mutated, obtained from University clinic Wuerzburg	Wuerzburg, Germany

Cells and tissue culture mediums

This section details the cell and tissue culture media, along with specific compositions, provider details and catalogue numbers critical for maintaining cellular environments and experimental consistency (table 2.2).

Table 2.2: Cells and tissue culture mediums

Medium	Specification	Application	Product number	Manufacturer / Provider; City, Country
DMEM (high glucose)	4500 mg/L glucose (+) L-Glutamin (+) Sodium bicarbonate	pFb medium	D5796	Merck; Darmstadt, Germany
MEM Glutamax	L-Glutamin (+) Earle's Salts (-) HEPES	Calu-3 medium	11095080	Thermo Fisher Scientific; Schwerte, Germany
Endothelial cell growth medium MV	according to provider's website	hEC and LbFb cell culture medium	C-22120	Promocell; Heidelberg, Germany
huAEC growth medium	according to provider's website	huAEC cell culture medium	INS-ME-1013	Inscreenex; Braunschweig, Germany
RPMI1640	(+) L-Glutamin	Stop medium	21875034	Thermo Fisher Scientific; Schwerte, Germany
DMEM Nutrient mixture F-12 Ham	(+) L-Glutamin (+) Sodium bicarbonate (-) HEPES	A549 medium	D8062	Merck; Darmstadt, Germany

Supplements for mediums

The following table 2.3 outlines the supplementary components incorporated into cell and tissue culture media. Each supplement is detailed with its specific concentration and purpose within the medium to ensure optimal cellular conditions and experimental consistency.

Table 2.3: Cell and tissue culture supplements

Supplement	End concentration	Application	Product number	Manufacturer / Provider; City, Country
Endothelial supplement mix for growth medium MV	30 ml for 500 ml medium	Endothelial cells culture medium	C-39225	Promocell; Heidelberg, Germany
Fetal Bovine Sera (FBS)	10%	growth supplement for Calu-3, A549, pFb	SUPERIOR stabil® FBS.S 0615	Bio & Sell ; Feucht, Germany
huAEC supplement mix	30 ml for 500 ml medium	human Airway Epithelial cell culture medium	INS-ME-1013BS	Inscreenex; Braunschweig, Germany
Dimethylsulfoxide (DMSO)	10%	Freezing medium	D2650	Merck; Darmstadt, Germany
			A994.2	Carl Roth; Karlsruhe, Germany

2.1.2 Biological and chemical substances

This table provides an overview of the biological and chemical reagents employed in the experiments, including their concentrations, suppliers, and catalogue numbers essential for maintaining consistency in experimental results.

Table 2.4: Biological and Chemical substances

Substance name	Specification	Product number	Manufacturer; City, Country
Acrylamide	500 g	A3553	Merck; Darmstadt, Germany
Alcian Blue 8GX		A357	Merck; Darmstadt, Germany
Ammonium persulfate (APS)	25 g	A3678	Merck; Darmstadt, Germany
Bovine serum albumin	50 g	A2153	Merck; Darmstadt, Germany
Bromophenol blue solution (0.04% wt in H_2O)	500 ml	318744	Merck; Darmstadt, Germany
Chromoline DAB substrate buffer	100 ml	PC136R100	DCS diagnostics; Hamburg, Germany

Table 2.4: Biological and Chemical substances

Substance name	Specification	Product number	Manufacturer; City, Country
Coomassie Brilliant blue G 250	25 g C.I. 42655	1.15444	Merck; Darmstadt, Germany
DMSO (Dimethyl sulfoxide)	50ml	D2438	Merck; Darmstadt, Germany
ROTI® Histokitt (Entellan) ready-to-use	500 ml	6638.2	Carl Roth; Karlsruhe, Germany
Eosin B (C.I. 45400)	M 624.09 g/mol	0306.3	Carl Roth; Karlsruhe, Germany
FITC-dextran (1:250)	50 mg/ml avg.MW 4000	46944	Merck; Darmstadt, Germany
Fluoromount-G, with DAPI (Invitrogen)		00495952, E139612	Thermo fisher scientific; Waltham, Massachusetts, USA
Gelatin	2%	646.1	Carl Roth; Karlsruhe, Germany
Glycerin (Chemsolute)		2039.1	Th. Geyer; Renningen, Germany
Glycerol	100 ml	G5516	Merck; Darmstadt, Germany
Glycine	250 g	50046	Merck; Darmstadt, Germany
Grease pencil			Daido, Japan
Hämalaun solution from Mayers		T865.2	Carl Roth; Karlsruhe, Germany
Hematoxylin acc to Mayer		51275-1	Merck; Darmstadt, Germany
huAEC coating solution		INS-SU-1018	Inscreenex; Braunscheig, Germany
Human plasma fibronectin (Gibco)	5 mg	33016-015	Thermo fisher scientific; Waltham, Massachusetts, USA
Hydrogen Peroxide		800768-07	Paul W Beyvers GmBh,; Berlin, Germany
Isopropanol			UCHEM, OvGU; Magdeburg, Germany
N,N'-methyl bisacrylamide		M7279	Merck; Darmstadt, Germany
Nuclear fast red - Aluminium-sulphate solution 0.1 %		N069.2	Carl Roth; Karlsruhe, Germany

Table 2.4: Biological and Chemical substances

Substance name	Specification	Product number	Manufacturer; City, Country
Paraformaldehyde	4%	256462	PanReac Applichem; Darmstadt, Germany
Ponceau S solution		33427.01	Th. Geyer; Renningen, Germany
Penicillin-Streptomycin		P0781	Merck; Darmstadt, Germany
Phalloidin 488 conjugate		ab176753	Abcam , ; Cambridge, UK
Phosphate buffered Saline (PBS-)	without Ca++ / Mg ++(10X)	X0515	BioWest/ Th. Geyer; Nuaille, France
Roti-Mount FluorCare DAPI	antifade mounting medium with DAPI	HP20,1	Carl Roth, ; Karlsruhe, Germany
Sodium dodecyl sulfate (SDS)	1000 g	L3771	Merck; Darmstadt, Germany
Sodium Pyruvate (Gibco)	100 ml	11360039	Thermo fisher scientific; Waltham, Massachusetts, USA
Tetramethyl ethylenediamine (TEMED)	100 ml	T9281	Merck; Darmstadt, Germany
Thiazolyl Blue Tetrazolium Bromide	1000 mg	M2128	Merck; Darmstadt, Germany
Tissue-Tek O.C.T Compound		4583	Sakura, Finetek USA, ;
Tris (base)		1070896001	Roche; Basal, Switzerland
Tris-Base	500 g	648310	Millipore-Sigma; Darmstadt, Germany
Tris-HydroChloride (Tris-HCl)	1000 g	648317	Millipore-Sigma; Darmstadt, Germany
Trypan Blue		15250-061	Thermo fisher scientific; Waltham, Massachusetts, USA
Trypsin	1 %	59429C	Merck; Darmstadt, Germany
Trypsin-EDTA	0.05 %	25300054	Thermo fisher scientific; Waltham, Massachusetts, USA
Tween 20	250 g	9127.1	Carl Roth; Karlsruhe, Germany

Table 2.4: Biological and Chemical substances

Substance name	Specification	Product number	Manufacturer; City, Country
VEGF-165 (Proteintech)		HZ-1038	Chromotek GmbH; Munich, Germany
Xylenes		214736	Merck; Darmstadt, Germany
10X TBS (Tris buffered saline)	10X	1706435	BioRad; Munich, Germany
2-mercaptoethanol (β -Mercaptoethanol)	25ml	M3148	Merck; Darmstadt, Germany
Ethanol	96%		UCHEM, OvGU; Magdeburg, Germany
Alcian Blue 8GS (C.I. 74240)	10 g	3082.1	Carl Roth; Karlsruhe, Germany
Accutase® cell detachment solution	in DPBS w/o Ca ²⁺ , Mg ²⁺	426201	BioLegend; California, USA

Enzyme and substrate solutions

The table 2.5 below provides a comprehensive list of enzyme and substrate solutions utilized in cell culture preparation and maintenance. This includes details on freezing medium composition, essential for cell preservation, as well as the specific concentration of trypsin used for cell dissociation.

Table 2.5: Enzyme & substrate solutions

Enzyme / substrate	Composition	Application
Freezing medium	20% DMSO in FBS (end concentration to 10% DMSO adjusted)	Freezing cells
huAEC coating solution	(1 ml per T75 flask)	huAEC flask pre-coating
Human Plasma Fibronectin	5 μ g/ml	optimized coating solution
Penicillin-Streptomycin	1 %	Antibiotic biopsy incubation
Sodium Pyruvate (1X)	1 %	Calu-3 medium
Stop Medium	20% FBS in RPMI1640	stop reaction of trypsinization
Trypsin-EDTA	0.03%	Cell passaging / trypsinization
VEGF-165	0.5ng/ml	hEC medium

2.1.3 Reference biomaterials for synthetic scaffold

The following table summarizes the reference biomaterials employed in scaffold construction and related applications. This includes details on scaffolds and polymers purchased specifically for the fabrication of electrospun membranes. Additionally, the table lists commercially available membrane inserts and biologically derived scaffold materials that were also incorporated in this study for their compatibility with Tissue Engineering applications. Each biomaterial entry includes supplier information and material specifications. Relevant preparation or processing notes are followed in the methods section 2.2 to ensure consistency in scaffold production and experimental use [36, 39].

Table 2.6: Reference biomaterials for synthetic scaffold

Biomaterials	Specification	Product number	Manufacturer/ Provider; City, Country
Poly-e-caprolactone (PCL)	electrospun (14%)	440744	Merck; Darmstadt, Germany
Poly-tri-methylene carbonate (PTMC)	electrospun (at 14% polymer) in mixture with PCL	900293	Merck; Darmstadt, Germany
Polyamide (PA)	electrospun (12%)	9620.2	Carl Roth; Karlsruhe, Germany
(Polyethyleneterephthalate (PET) thincert®)	12-well; pore diameter 0.4 μm	665641	Greiner; Frickenhausen, Germany

2.1.4 Analytical biological components

Antibody list

The table below provides a detailed overview of the antibodies utilised in this study, encompassing both primary and secondary antibodies, as well as controls. Each entry includes critical information such as antibody concentration or dilution used, specific clone identifiers, and catalogue or order details, along with the provider's information. Additionally, antibodies conjugated with fluorophores for fluorescence-based assays are highlighted, specifying the application method (e.g., IHC, IF, WB) in which each antibody was applied.

Table 2.7: Primary and secondary antibodies

Antibody	Specification	Fluorophor	Application	Dilution	Product number	Manufacturer/ Provider; City, Country
Anti-mouse IgG	secondary antibody, host: goat; stock: 1mg/ml	FITC	IF	1:50	F0257, SLCF3963	Merck; Darmstadt, Germany
Anti-rabbit IgG (H+L)	secondary antibody, host: goat; stock: 2mg/ml	TRITC	IF	5 µg/ml	SAB4600084	Merck; Darmstadt, Germany
CD155 / PVR	rabbit-polyclonal; A549 nucleoplasm	without	IF / IHC	IF: 1:100 IHC: 1:500	C106450	Merck; Darmstadt, Germany
CD31 (Proteintech)	clone: 3F8E2 endothelial cell marker	without	IF / IHC	IF: 1:50 IHC:1:100	66065-2-Ig	Chromotek GmbH; Munich, Germany
E-Cadherin	rabbit-polyclonal epithelial cells / adherent junctions	without	IF / IHC	IF: 1:100 IHC: 1:500	SAB4503751	Merck; Darmstadt, Germany
IgG Mouse	negative control against primary antibodies with host mouse	without	IHC	acc. to host specific primary antibodies	I8765	Merck; Darmstadt, Germany
IgG Rabbit	negative control against primary antibodies with host rabbit	without	IHC	acc. to host specific primary antibodies	I8140	Merck; Darmstadt, Germany
Pan-Cytokeratin (Invitrogen)	clone: C-11; Epithelial cytoskeleton	without	IF / IHC	IF: 1:100 IHC: 1:300	MA5-12231	Thermo fisher scientific; Waltham, Massachusetts, USA
Vimentin	clone: V9; fibroblasts	without	IF / IHC	IF: 1:100 IHC: 1:500	V2258	Merck; Darmstadt, Germany
ZO-1 (Invitrogen)	clone: ZO1-1A12 Epithelial cells / tight junctions	without	IF / IHC	IF: 1:100 IHC: 1:500	33-9100	Thermo fisher scientific; Waltham, Massachusetts, USA
PageRuler™ Plus Prestained Protein Ladder	10 to 250 kDa	without	WB		26619	Thermo fisher scientific; Waltham, Massachusetts, USA
Muc5AC (Invitrogen)	clone 45M1; monoclonal; 0.2 mg/ml; host mouse	without	WB / IF	IHC (P) 1-2 µg/mL; ICC/IF 2-3 µg/mL; WB 1:2000	MA512178; XC3544999A	Thermo fisher scientific; Waltham, Massachusetts, USA
Muc5B (Invitrogen)	clone 5B19-2E; monoclonal; 0.5 mg/ml; host mouse	without	WB / IF	(ICC/IF) 2 µg/mL, WB 1:2000	37-7400; WI336448	Thermo fisher scientific; Waltham, Massachusetts, USA
AEC2 N1N2 nterminal	host rabbit; 1.66mg/ml	without	IHC / IF	IHC 1:1000	GTX101395, 44006	Genetex; California, USA
SFTPC (Invitrogen)	polyclonal; host rabbit; 1mg/ml	without	WB/ IF	WB 1:2,000; IHC (P) 1:200 ; ICC/IF 1:500	PA5-102493	Thermo fisher scientific; Waltham, Massachusetts, USA
Goat anti-Mouse secondary antibody (Invitrogen)	host goat; (1:1 diluted prior with glycerol)	HRP	WB	WB 1:10000 to 1:5000 (8 µl in 20ml TBST)	31430	Thermo fisher scientific; Waltham, Massachusetts, USA

Goat anti-rabbit secondary antibody	host goat; (1:1 diluted prior with glycerol)	HRP	WB	WB 1:10000 to 1:5000 (8 μ l in 20ml TBST)	31460	Thermo fisher scientific; Waltham, Massachusetts, USA
--	--	-----	----	---	-------	--

Analytical kits

The following table includes all reagents and components used in the analytical detection methods, with concentrations, suppliers, and preparation notes for optimal assay reproducibility.

Table 2.8: Analytical kits and components

Product	Composition		Application	Product number	Manufacturer/ Provider; City, Country
Super Vision 2 HRP kit	HRP polymer	LD520R050	IHC	PD000KIT	DCS diagnostics; Hamburg, Germany
	Polymer enhancer	LD510R050			
	DAB Chromogen	DCI35C006			
	DAB substrate buffer	PC136R100			
Bradford Protein assay Kit	Bradford protein assay reagent	950 ml	Bradford assay	23200	Thermo fisher scientific, Rockford, USA
	Albumin standard	10 x 1 ml		23209	
ECL Western Blotting substrate Kit	Detection reagent 1, peroxide solution	25ml	Western Blotting	32109	Thermo fisher scientific; Rockford USA
	Detection reagent 2, luminol enhancer solution	25ml			

Analytical Solutions and buffers

The following table details the various analytical solutions and buffers used throughout this study, including essential washing and blocking buffers. Each solution is specified with its composition and purpose, such as washing buffers used to remove unbound reagents during staining or analytical procedures and blocking buffers designed to prevent non-specific binding in assays. The table also includes preparation details and applications, ensuring reproducibility and consistent performance in all analytical applications.

Table 2.9: Analytical solutions and buffer compositions for various applications

Solution	Composition	Application
1X PBS-	50 ml PBS- (10x) + 450 ml ddH ₂ O	cell culture/ IHC/ IF
Antibody dilution buffer	1 % BSA + 0.05 % Tween 20 in 1x PBS-	IF (adherent cells)
Antibody dilution buffer	0.5 % BSA in 1x PBS-	IHC
Blocking buffer	1 % BSA + 0.2 % Tween 20 in 1x PBS-	IF (adherent cells)
Blocking buffer	0.5 % BSA in 1x PBS-	IHC
Blocking buffer	5 % FBS + 1 % BSA in 1x PBS-	IF (tissues)

Table 2.9: Analytical solutions and buffer compositions for various applications

Solution	Composition	Application
Permeabilization buffer	0.5 % Tween 20 in 1x PBS-	IF (adherent cells)
washing buffer	0.5 % Tween20 in 1x (PBS-)	IHC/ IF
Tris HCL 2M pH:6.8	315.2 g in 1 L ddH ₂ O	WB
Tris HCL 1.5M pH:8.8	236.4 g in 1 L ddH ₂ O	WB
Tris HCL 0.5M pH:6.8	78.8 g in 1 L ddH ₂ O	WB
Transfer buffer (1X)	3g Tris base + 14.4 g glycine + 200 ml methanol for 1 L ddH ₂ O	WB
TBS (10X)	24g Tris base + 88g NaCl in 900 ml ddH ₂ O (for 1 L) (Adjust pH to 7.6 with 12 N HCl (H1758). Adjust final volume to 1 L with Milli-Q® Water; Prepared TBS is stable at 4 °C for 3 months.)	WB
TBS (1X)	100 ml TBS(10X) in 900 ml ddH ₂ O	WB
30 % Acrylamide	29.22 g Acrylamide+ 0.78 g bisacrylamide + 100 ml water	WB
1X TBST	100 ml TBS(10X) + 1 ml TweenT® 20 in 900 ml ddH ₂ O	WB
1X PBST	100 ml PBS minus(10X) + 1 ml TweenT® 20 in 900 ml ddH ₂ O	WB
10X Running buffer	30 g Tris base +144.0 g Glycine +10 g SDS in 1 L ddH ₂ O	WB
1X Running buffer	100 ml running buffer (10x) in 900 ml ddH ₂ O	WB
APS 10 %	1g for 10 ml ddH ₂ O	WB
APS 20 %	2g for 20ml ddH ₂ O	WB
SDS 10 %	1g for 10 ml ddH ₂ O	WB
SDS 20 %	2g for 20ml ddH ₂ O	WB
10 % 2-mercaptoethanol	5ml for 50ml laemmli buffer	WB
20 % 2-mercaptoethanol	10ml for 50ml laemmli buffer	WB

2.1.5 Equipments, Software and Consumables

The table below provides a comprehensive list of the equipment, software, and consumable materials utilised in this research. This includes details on laboratory instruments essential for experimental procedures, along with software tools used for data acquisition, analysis, and visualization. Additionally, consumables such as pipettes, culture plates, and tubes are listed to ensure complete documentation of all materials required for reproducibility. For each item, specifications, model information, and supplier details are provided, supporting consistency and traceability in experimental setup and data processing.

Table 2.10: Equipments

Equipment	Specification	Manufacturer/ Provider; City, Country
Autoclave	LABAUTOKLAV 55-195	SHP steriltechnik AG; Wolfratshausen, Germany
Cell culture CO2 incubator	BBD 6220	Thermo fisher scientific; Waltham, Massachusetts, USA
Centrifuge	Heracus Megafuge 4R	Thermo fisher scientific; Waltham, Massachusetts, USA
ChemiDOC	XRS+	BioRAD; Munich, Germany
Cryomicrotome	CM 1950	Leica; Wetzlar, Germany
EVOS light microscope (Invitrogen)	XL Core, 4x, 10x, 20x, 40x	Thermo fisher scientific; Waltham, Massachusetts, USA
Fluorescence microscope	Axio Observer	Zeiss; Oberkochen, Germany
Bubble pressure tensiometer	BP100	Krüss scientific; Nuremberg, Germany
Force transducer	50N, Xforce HP	Zwick roell; Ulm, Germany
Plate shaker (Stuart, BioCore)	SeeSawrocker SSL4	Fisher scientific; Schwerte, Germany
Table top eppendorf centrifuge	5415 C	Eppendorf; Hamburg, Germany
TECAN microplate reader	SPARK	TECAN; Männedorf, Switzerland
Vortexer	Lab dancer	IKA; Staufen, Germany
Water bath (Gesellschaft für Labortechnik)	Typ 1113, 10600218A	Fisher scientific; Schwerte, Germany
Weighting balance	ADB	Kern & Sohn GmbH; Balingen, Germany
Trans-Blot transfer system	Turbo TM	BioRad; Munich, Germany
Power Source	250V	VWR; Dresden, Germany
Thermomixer	F1.5	Eppendorf centrifuge; Hamburg, Germany

Table 2.10: Equipments

Equipment	Specification	Manufacturer/ Provider; City, Country
pH measurement device	pHenomenal (TM)	VWR; Dresden, Germany
Pipette helper (boy)	9281090	VWR; Dresden, Germany

Table 2.11: Softwares

Software	Version	Use	Manufacturer/ Provider; City, Country
Advance krüss	V 1.14	Surface tension measurement / static fore measurement	Krüss scientific; Nuremberg, Germany
Fiji ImageJ	V 2.16	Image processing	Image J, National Institutes of Health (NIH); Bethesda, USA
ImageLab BioRAD laboratories	V 6.1	Western blot / gel electrophoresis	BioRAD laboratories ; Munich, Germany
MS Excel	Office 365	Data analysis (FITC / ST / Rheometry)	Microsoft corporation; Redmond, USA
Origin Pro	2019	Data analysis (FITC)	Origin Lab corporation; Northampton, USA
SparkControl	3.2	Microplate reader software for SPARK	TECAN; Männedorf, Switzerland

Table 2.12: Lab consumables

Material	Specification	Product number	Manufacturer/ Provider; City, Country
Cell culture plates	6 well / 12 well	657160; 665180	Greiner Bio one, Frickenhäusen, Germany
Cell culture flasks	T75	7696782	Th. Geyer
Parafilm		291-0557	VWR; Dresden, Germany
Microscope slides SuperFrost (R) plus	25x75x1.0mm	631-0108	VWR; Dresden, Germany
Chamber slides	8 μ well	177402	Nunc Lab-tek
Pasteur pipettes	Glass, 150mm, 230mm		Brand / Kimble; Germany
Pipettes	5000, 1000, 200, 10 μ l		Eppendorf; Hamburg, Germany
Centrifuge tubes	50ml	7696719	Th. Geyer; Renningen, Germany
Eppendorf spitzen	0.1 - 10 μ l	9409410	Th. Geyer; Renningen, Germany
Eppendorf spitzen	0.2 - 200 μ l	10248621	Fisher scientific; Schwerte, Germany
Serologisch pipettes	10ml	612-5541	VWR; Dresden, Germany
Serologisch pipettes	25ml	VWRI612-5544_P	VWR; Dresden, Germany

Serologisch pipettes	50ml	612-5546	VWR; Dresden, Germany
Eppendorf spitzen	50-1000 μ l	613-3505	VWR; Dresden, Germany
Coverslips	24 x 50		Menzel gläser
Pipette boy	Accujet Pro		Brand GmbH; Wertheim, Germany
Microwell plates	96 well flat bottom	10216341	Fisher scientific; Schwerte, Germany
Microwell plates	96 well black	353219	Corning; Kaiserlautern, Germany
Trans-Blot Transfer Pack	Midi format 0.2 μ m PVDF	1704157	BioRAD; Munich, Germany
Trans-Blot Transfer Pack	Mini format 0.2 μ m PVDF	1704156	BioRAD; Munich, Germany
Mini Protean space plates	1.0 mm	1653311	BioRAD; Munich, Germany
Mini Protean Comb 15 well	1.0 mm, 26 μ l	1653360	BioRAD; Munich, Germany
TissueTek(R) Cryomold (R)	25x20x5mm	4557	Science Services, Munich, Germany
SuperPAP pen liquid blocker		N71310_N	Science Services; Munich, Germany

2.2 Methods

2.2.1 Scaffold materials

Biological Scaffold material

SIS-muc derived after the decellularization process of porcine jejunum segments, thoroughly sterilised, is transferred under the biosafety cabinet sterile environment [81, 82]. The tube-like segment is opened to expose the inner mucosal tissue layer. Sterilised metal cylindrical cell culture inserts (meta cell crowns)—both the inner insert and the outer part are used to mount the SIS-muc membrane in a step-by-step process [49, 83].

To initiate the preparation of SIS-muc scaffolds, we carefully removed the material from its container with sterile tweezers and spread it onto a petri dish. Initially, the SIS-muc scaffold appears in a tubular structure that requires an opening. A scalpel was used to make a longitudinal cut along the length of the tube. Tweezers were then used to pull and flatten the scaffold, exposing the inner mucosal layer facing upwards. Next, sterile cell crowns were prepared. The inner crown was placed over the scaffold, and a square section was cut with a scalpel, leaving a margin of at least 1 mm around the crown. The inner crown was then inverted so that the wetted surface faced upwards. Using tweezers, the cut scaffold was carefully lifted and flipped over onto the crown, ensuring that the mucosal surface faced downwards inside the crown. The scaffold was arranged to completely cover the crown's surface without leaving gaps. An outer cell crown was positioned over the inner crown using tweezers, securing the scaffold tightly between the two crowns. These models were carefully flipped and placed into the wells of a 12-well plate. Once the models were placed in the plate, 1200 μ l of the cell-specific medium was added to the basolateral side of each well. Care was taken to remove any air bubbles formed during the addition of the medium. Inside the insert, 500 μ l of the same medium was added, and the plate was incubated for at least 2 h before cell seeding.

Production and preparation of synthetic scaffolds

PCL, PTMC, and PA polymer materials were used to develop flat membrane-like scaffolds using the electrospinning technique. The electrospinning procedure for all the materials was kindly done by Tobias Weigel from Fraunhofer Translational Centre for Regenerative Medicine, Fraunhofer ISC, Wuerzburg, Germany.

Production of PCL, PCL:PTMC in 70:30 and 50:50 mixture proportions:

Electrospinning is a widely known technology used to produce porous scaffolds. PCL semicrystalline polyester polymer and PTMC, a flexible polymer, were dissolved to form a polymer solution using HFP solution. Spinning solution was prepared using 14 % (m/v) total polymer concentration (example: 1.4 g polymer + 10 ml solvent). In addition to pure PCL (100:0), polymer solutions were also mixed in 50:50 and 70:30 PCL:PTMC ratios correlated to the mass. The spinning solution was homogenised overnight under agitation at 4 °C and immediately electrospun on the next day. Briefly, a rotating cylinder target was suspended in the centre of the electrospinning setup while two syringe pumps filled with polymer solutions were placed on either side. While the collector was rotated at a speed of 100 rpm, increasing voltage in the range of 6.8 – 9.5 kV was applied to the capillary tube filled with polymer solution held at the tip of the capillary. Initially, due to the applied electric field, mutual charge repulsion is formed in the polymer solution, opposing its surface tension, but increased voltage in the later stage induces jet formation of the polymer solution when the electrical charge overcomes the solution surface tension, hence evaporating the solvent completely. The solution feeding rate was maintained at 1 ml/h, and polymer jets were deposited randomly into a fibre form on the collector surface.

Production of PA scaffold membrane: Production of PA scaffold followed the same procedure as described above, with some exceptions. Here, a 12% m/v polymer solution was prepared using HFP solvent. Similar spinning parameters were used as described above, with a feeding rate of 0.6 ml/h.

Preprocessing of membranes

PCL:PTMC 50:50 / PCL:PTMC 70:30:

Briefly, the membrane scaffolds obtained after the electrospinning and the UV sterilisation process were handled under sterile conditions under the biosafety cabinet. Similar to SIS-muc membrane cut procedure, the membranes were cut into appropriate sizes for the metal cell crowns. These cut membranes were then transferred each into a 6-well plate and immersed in sterile filtered 70% ethanol overnight (3 ml / well). On the next day, the ethanol is discarded carefully without

disturbing the membrane, and the plate is sealed using parafilm and sterilised under UV for 2 h inside the biosafety cabinet. After the membranes were again washed 3 times with PBS- (3 ml per wash), an extra membrane sample was also tested for bacterial growth using agar plates after 3 days of incubation with hEC medium. The membrane cuts were then ready to be mounted on the metal cell crowns.

PA membranes:

PA electrospun membrane sheets were obtained in sterile conditions and packed in aluminium foils. These were transferred under the sterile biosafety cabinet and cut into appropriate dimensions suitable for metal cell crowns. The cut membrane pieces were then transferred to a sterile cell culture bottle (250 ml) containing 150 ml of 1x sterile PBS-. These bottles were then autoclaved using standard autoclave protocol for buffers (121°C). After sterilisation, the membranes transferred to 6-well plates were extra UV sterilised before use for the establishment of *in vitro* models using metal cell crowns.

Pre-coating solutions for membranes:

Initially, 2 % gelatin coating for endothelial cells (on basal side) and huAEC coating for alveolar epithelial cells (apical side) was used. To enhance the cellular attachment, further optimisations were made by adding human plasma fibronectin (5 µg/ml) and VEGF-165 protein (0.5 ng/ml) for endothelial cell coating solution (further referred to as optimised coating solution).

Tensile test of scaffold membrane

A uniaxial tensile test was performed on the manufactured synthetic scaffold variants PCL:PTMC 70:30, PCL:PTMC 50:50, and PA. The specimens from the sterile membranes were cut uniformly to a width of 3 cm. The measuring area was adjusted to approximately 1.8 mm^2 . All the tensile tests were carried out according to the defined ASTM D638 standard. Briefly, crosshead speeds of 5 mm/min were set, and a 50 N force transducer was used on a Zwick Roell Type XForce HP testing machine. All scaffolds were measured at room temperature. The raw data generated was utilised to plot a graph of strain vs. standard force. The initial linear region was then used to calculate the slope and hence Young's modulus.

2.2.2 Isolation, cultivation and characterisation of cells

General cell culture conditions and protocols:

Standardised cell culture protocols were used for general 2D cultivation of all cells and cell lines. 2D culture of all the cells and cell lines was maintained in a humidified incubator at 5 % CO_2 , 37 °C, and 98 % humidity to provide a controlled environment for optimal growth. Furthermore, mycoplasma testing was conducted quarterly on all cell lines to prevent contamination and maintain the quality of the cultures. All the cells and cell lines are handled under sterile conditions, and all general cell culture steps as well as model development are performed inside a sterile biosafety cabinet. Cell culture growth mediums and cell culture buffers are prewarmed in the water bath before use, unless specifically specified for other methods. All cells and cell lines were cultivated until 80% confluency, and the medium was exchanged three times per week. Cells were cultivated until passage number 7 and utilised for the establishment of *in vitro* models until maximum passage of 15 unless otherwise stated. Cells/cell line was grown and maintained in continuous culture using a standardised cell detachment protocol. Briefly, tissue culture flasks containing adherent cells were washed 3 times with 1x concentrated PBS- buffer and incubated with an appropriate amount of 0.025 % Trypsin-EDTA solution for 4 min. Cellular detachment was controlled under the microscope, and the trypsinization reaction was halted by the addition of a double volume of stop medium. This cell suspension was collected in a centrifuge tube and centrifuged at 2500 rpm at 4 °C for 5 min. The remainder cell culture supernatant is discarded, and the cell pellet is utilised after thorough cell counting according to standardised protocol using a Neubauer chamber and appropriate trypan blue dilutions.

Cell lines including Calu-3, A549, primary human endothelial cells (hEC), human airway epithelial cell line (CI-huAEC), primary dermal fibroblasts (pFb), and primary lung biopsy-derived fibroblasts (LbFb) were cultivated in respective culture mediums (as summarised in the table 2.13) under standard conditions (37 °C, 5 % CO_2).

Cell culture of human endothelial cells and human airway epithelial cells

Human primary endothelial cells (hEC) were cultured on 2 % gelatin-precoated cell culture flasks in 2D culture in similar conditions as above in their respective human endothelial medium prepared as directed in Table 2.13. Human airway epithelial cell lines (CI-huAEC) resembling the alveolar type 1 cell type were obtained from InScreenex GmbH, Braunschweig, Germany (INS-CI-1015). (Later on, the cells

CI-huAEC were rebranded by InScreenex under the new name CI-huAELVi, hence, in further instances, we will refer to them with "huAEC.") The cells were cultured in the adherent cell culture flasks precoated with huAEC coating solution for a minimum of 2 h (to overnight in the incubator). huAEC were cultured in 2D until 80% confluency using a manufacturer-supplied huAEC medium kit suitable for alveolar cells and passaged as explained in the paragraph section above using standard cell passage protocols. For respective cell media composition, please refer to table 2.13 below. Both the cell types were used in the passage number from 4 to 14.

Table 2.13: Cells or cell line-specific culture medium composition

Cells / cell line	Specification	Medium composition
Calu-3	human bronchial epithelial cell line isolated from lung tissue derived from a 25-year-old, White, male patient with lung adenocarcinoma	MEM FBS : 10% NaPyr : 1% (Calu-3 medium)
A549	human lung adenocarcinoma cell line with Type II alveolar epithelium (ATII)	DMEM / HAM F12 FBS : 10% (A549 -medium)
pFb	Primary human dermal fibroblasts	DMEM (high glucose) FBS : 10% (pFb medium)
hEC	Human primary endothelial cells	Endothelial growth medium MV : 470ml Endothelial supplement : 30ml mix MV (manufacturer's protocol) (hEC medium)
huAEC	Human alveolar epithelial cells	huAEC medium : 470ml huAEC supplement : 30ml mix (manufacturer's protocol) (huAEC medium)
LbFb	Human Lung biopsy derived fibroblasts	hEC medium

Isolation of pulmonary fibroblasts from human lung biopsy:

Lung biopsies were obtained from patients undergoing lung resections at University Hospital Magdeburg after they signed informed consent [ethical vote 163/17]. Fibroblasts were isolated according to the established standardised protocols. Briefly, the lung biopsies were carefully cut and washed thoroughly with PBS- supplemented with penicillin and streptomycin in 1 % concentration. Minced biopsy pieces were then incubated with 1 % trypsin for 2 h at RT and centrifuged, and the cell pellet obtained was suspended in a cell culture flask while the supernatant was centrifuged and cultured in new flasks. Obtained fibroblasts were kept in cultivation until passage 5 to 8 and characterised as vimentin-positive fibroblasts before use in the *in vitro* models.

Table 2.1 specifies the details of the cells or cell lines utilised in this study, along with the medium composition used for 2D cultivation (refer table 2.13). All the media were prepared under sterile conditions in a biosafety cabinet.

Immune fluorescence staining of cells/cell lines

Cells were tested for cellular integrity using cell-specific marker using immune-cytofluorescence staining for adherent cells according to the standardised protocols. Cell specific markers included, Calu-3 – ZO-1; A549 – CD155; huAEC – E-cadherin; hEC – CD31) in their respective dilutions as provided by manufacturer protocols along with respective negative IgG controls as described in the table 2.7.

Adherent cells were grown in a cell culture flask until reaching 90 - 95% confluency. Cell trypsinization and counting were performed according to standard operating procedures (SOPs) to detach and quantify the cells. 8 μ -well chamber slides were unpacked within a sterile biosafety cabinet, and $1 - 5 \times 10^4$ cells (depending on cell-specific doubling rates) were seeded per well, with 250 μ l of cell-specific medium added to each chamber. The chamber slide was covered and incubated at 37 °C in a 5% CO₂ atmosphere for at least 3 h or overnight to allow cell attachment. Cells were cultured until they reached 50 - 60% confluency, with medium changes every second day.

For staining, the cell culture medium was aspirated, and the cells were washed with 200 μ l PBS- per well, ensuring that the well surface was not directly touched. Cells were fixed with 200 μ l of 4% formaldehyde per well for 10 min at room temperature (RT), followed by three PBS- washes. This was followed by the permeabilization step by adding 200 μ l of permeabilization buffer to each well and incubating for 10 min at RT. The permeabilization buffer was aspirated, and the cells were washed again

with PBS- three times. Cells were blocked by adding 200 μ l of blocking buffer per well, incubating for 30 min at RT, and then aspirating the blocking buffer. Primary antibodies as listed above were diluted in antibody dilution buffer and added to the wells (150 μ l per well). Incubation occurred either for 2 h at RT or overnight at 4 °C. Following this, cells were washed with blocking buffer, and secondary antibody conjugates were prepared and added to the wells in the dark for 2 h at RT. After secondary antibody incubation, cells were washed twice with blocking buffer and stained with an antifade mounting medium containing DAPI. The slides were stored at 4°C in the dark until imaging, though it is recommended to proceed with imaging immediately to avoid degradation of signal quality over time.

2.2.3 Optimisation of region-specific airway models

SIS-muc based models

SIS-Muc Calu-3 with pFb co-culture:

Fibroblasts were cultured in 2D until 70 to 80 % confluency and then trypsinised and were seeded 5×10^4 cells per crown onto the SIS-Muc. Medium was exchanged every second day. On the 3rd day, Calu-3 cells were trypsinised and seeded on top with the cell density of 1×10^5 per crown and cultured under immersed culture conditions with 500 μ l Calu-3 medium in the apical region and 1500 μ l of 50 % Calu-3 and 50 % fibroblasts medium in the basal region for 7 days. ALI culture was started after 7 days of immersed co-culture by aspirating out the medium from the apical region and making it exposed to air while the nutrient-rich medium in optimised proportion was supplied via only the basal region (1:1 Calu-3 and fibroblasts medium). The culture was carried out for a maximum of 4 weeks with intermittent medium exchange every second day. Tissue models were embedded in Tissue-Tek O.C.T Compound (Sakura, Finetek USA, Torrance Canada 4583) on weeks 1, 2, 3, and 4 and stored in -80 °C. The experiments were repeated thrice.

Similarly, steps were again repeated to setup co-culture models of A549 with pFb. These experiments were repeated thrice under the same conditions.

PET thincert® based models

For the co-culture of Calu-3 cells with fibroblasts (Calu3-pFb) and A549 cells with fibroblasts (A549-pFb) on PET membrane, the following approach was established. Like the process above, 5×10^4 fibroblasts were first seeded on the bottom side of the insert by simply inverting the inserts and placing them inverted in a 6-well plate and seeding with fibroblasts overnight in the incubator. Humid conditions were

maintained by adding a culture medium to the well. Fibroblasts adhered to the membrane overnight, and the inserts were transferred back into a 12-well plate and were cultured in fibroblast medium both in the apical and basal regions for 2 days. On the 3rd day, 1×10^5 Calu-3 cells (1×10^5 A549 cells for A549-pFb co-culture models) were seeded per insert from the top (in the apical region), and immersed culture was carried out for 7 days. On the 7th day of co-culture, ALI was started and continued until 4 weeks. Medium exchange was performed on every second day using optimised co-culture medium only from the basal region; for Calu-3-pFb culture: 50 % Calu-3 and 50 % fibroblasts medium; for A549-pFb co-culture: 50 % A549 and 50 % fibroblasts medium. Again, models were fixed after weeks 1, 2, 3, and 4 in 4% paraformaldehyde for 10 min at RT, followed by paraffin embedding and cut for further histochemical analysis.

Establishment of co-culture models with huAEC, fibroblasts, and endothelial cells

For the establishment of co-culture of hEC with huAEC, various optimisations were carried out. Membranes were pre-coated using the respective coating solution (refer fig. 2.1), overnight on the bottom side of the Thincert® to avoid seeping of endothelial cells through the pores of the PET membrane in addition to the huAEC coating on the top side of the membrane. Briefly, the membrane models (PET thincerts® and metal crown-mounted synthetic membrane models) were inverted and placed in a sterile 6-well cell culture plate, and 100 μ l of the respective coating solutions (according to the co-culture model type as listed in table 2.1 below) were spread over the membrane surface. Following the overnight incubation, the inserts were inverted back into position, transferred to 12 well plates, and coated with the respective coating solution on the apical side (at least for 2 h in the incubator).

Following fig. 2.1 summarises the setup of different co-cultures based on synthetic membrane variants, along with their timeline and cell seeding schemes, specific mediums, and start point for ALI cultures.

Co-Culture Model	Membrane Type	Coating	Cell Seeding (Day/Location)	Co-Culture Medium	ALI Culture start
A  huAEC-hEC	PET, PCL:PTMC 50:50, PCL:PTMC 70:30	– Apical: huAEC coating medium – Basal: Optimized coating solution	– hEC: 1.5×10^5 (Day 1, basal side) – huAEC: 2.5×10^5 (Day 3, apical side)	2:1 hEC:huAEC medium with 0.5 ng/ml VEGF165	Day 7
B  huAEC-LbFb	PET Thincerts®	– Apical: huAEC coating medium	– LbFb: 5×10^4 (Day 1, basal side) – huAEC: 2.5×10^5 (Day 3, apical side)	1:1 LbFb:huAEC medium	Day 7
C  huAEC-LbFb-hEC (Mattek Approach)	PET	– Apical: Special huAEC coating – Basal: 2% gelatin	– LbFb: 5×10^4 (Day 1, apical side) – hEC: 1.5×10^5 (Day 3, basal side) – huAEC: 2.5×10^5 (Day 7, apical side on fibroblast monolayer)	1:1 hEC:huAEC medium with 0.5 ng/ml VEGF165	Day 10
D  huAEC-hEC-LbFb	PCL:PTMC 50:50, PCL:PTMC 70:30, PA	– Apical: huAEC coating medium – Basal: Optimized coating solution	– hEC: 1.5×10^5 (Day 1, basal side) – huAEC: 2.5×10^5 (Day 3, apical side) – pFb: 5×10^4 (Day 1, wells; triple culture start at day 5)	2:1 hEC:huAEC medium with 0.5 ng/ml VEGF165	Day 7
					

Figure 2.1: Summarized co-culture models establishment timeline for synthetic scaffold-based models [6].

To establish a suitable co-culture medium for the co-culture of hEC with huAEC and LbFB, pilot experiments were carried out on hEC and huAEC cell types cultured on 2D 12-well cell culture plates. Cell viability was assessed using a standard MTT assay protocol according to lab-standardised SOP. Briefly, each cell type was cultured in duplicates on a separate 12-well plate. Culture mediums were mixed in different proportions namely: hEC:huAEC 1:1, 1:2, 2:1 respectively, supplemented with 0.5 ng/ml VEGF-165 and without VEGF-165. MTT assay was performed at different time points of medium incubation, namely, after 3 days, 1 and 2 weeks of cellular incubation separately for hEC and huAEC. Upon analysis, a 2:1 hEC:huAEC medium mixture with 0.5 ng/ml of VEGF-165 was used in the co-cultures of hEC-huAEC-LbFb.

PET co-culture models

PET membrane was used to co-culture huAEC (apical) on hECs (basal side) after respective precoating of the membrane, as summarized in the table 2.1 above. The pre-coated membrane models were inverted in a fresh 6-well plate and seeded with 1.5×10^5 cells (in 100 μ l) per model. 1 ml of hEC medium is added in the well to maintain the required humidity. The plate is closed tightly and placed in the incubator for 2 h. The models are inverted back into position and transferred to respective 12-well cell culture plates filled with 1200 μ l of hEC medium supplemented with 0.5 ng/ml VEGF-165 in the well. On the next day, 500 μ l of the fresh medium is added inside the insert. On the third day, medium from the apical as well as basal region is discarded and 2.5×10^5 huAEC cells are seeded in the apical side with 600 μ l of huAEC medium and 1200 μ l of hEC medium in the basal region of these models. On the immediate next day, the medium is refreshed using the optimised co-culture medium of 2:1 proportion hEC (plus 0.5 ng/ml VEGF-165): huAEC medium, 1200 μ l in the basal region, and 600 μ l in the apical region. ALI culture was started on the 7th day and these models were cultured until day 12. The models were then embedded in Tissue-Tek OCT compound after days 7, 10 and 12 of ALI, and stored at -80 °C, until further processing.

Similar models were constructed for co-culture of huAEC with LbFb (basal side), where instead of hEC cells, 5×10^4 LbFb fibroblasts were seeded on the basal side after basal coating of 2 % gelatin, on day 1. This was then followed by huAEC cell seeding 2.5×10^5 cells per model on day 3. The co-culture was carried out using a 1:1 mixture of hEC and huAEC medium and ALI was started on day 7. Models were maintained until day 12, with medium exchange performed on every second day.

Mattek-based approach:

Mattek EpiAlveolar model approach was replicated, and co-culture of huAEC-LbFb-hEC was established using PET membrane Thincert® as described in detail in the table 2.1 above. Briefly, precoated with 2% gelatin solution on the basal side, and huAEC coating on the apical side were first seeded with LbFb fibroblasts in the apical region (5×10^4 cells / model) on day 1. The models were maintained in hEC medium on both apical (600 μ l) and basal sides (1200 μ l). This was followed by hEC cell seeding, 1.5×10^5 cells per model dissolved in 100 μ l of hEC medium on the basal side by inverting the inserts in a fresh 6-well plate. The plate was closed carefully and incubated for at least 2 h in the incubator. The inserts were inverted back into the right orientation and transferred to their respective wells in a 12-well cell culture plate with 1200 μ l (basal) of hEC medium (plus VEGF-165). On the next day, 600 μ l of the same medium was also added in the apical region of these models. On day 7, the culture medium from the apical side was discarded carefully without touching the membrane, and the basal region medium was refreshed with fresh hEC medium (plus VEGF-165). huAEC cells were seeded, 2.5×10^5 cells per model, in the apical region with 600 μ l of huAEC medium. On the next day, mediums from both regions were replaced with an optimised co-culture medium consisting of a 1:1 mixture of hEC medium and huAEC medium supplemented with 0.5 ng/ml VEGF-165 and maintained in an immersed culture. ALI culture was started on the 10th day and cultured for 4 weeks. The models were then embedded in the Tissue-Tek OCT compound after days 10, 12 of ALI, and stored at -80 °C, until further processing.

Electrospun synthetic membrane-based models

Complex co-cultures using hEC, huAEC and LbFb were setup using electrospun membrane variants, namely on PCL:PTMC 50:50, 70:30, PA, and PCL membranes, as described in the table 2.1 above. Briefly, the membrane cuts obtained after sterilisation and preprocessing, as described in the section above, were mounted as tightly as possible in the sterilised metal cell crowns. Parallel models for each membrane were also prepared in separate 12-well plates for FITC assay negative control models without cells.

Following a similar cell seeding timeline as described above, first hEC cells were seeded on the basal side of the membranes mounted on the metal cell crowns by inverting them in a separate sterile 6-well cell culture plate. After 2 h of hEC cell seeding in the inverted position, the crowns are placed back in the correct orientation in the respective 12-well plate with 1200 μ l of hEC medium (plus VEGF-165) on the basal side and medium in the apical region on the immediate next day. On the

same day, fibroblasts isolated from lung biopsies were seeded into the wells (5×10^4 cells/ well) in a separate 12-well plate, required later on for establishing the triple culture (during the start of co-culture). This additional step was included in order to investigate the influence of the presence of fibroblasts on the establishment of co-culture of huAEC with hEC. On day 3, huAEC cells were seeded on the apical side of the membrane with 600 μ l of huAEC medium in the apical region and refreshed with the hEC medium in the basal region. Mediums in both apical (600 μ l) and basal region (1200 μ l) were replaced with the optimised co-culture medium of 2:1 proportion of hEC (plus VEGF-165):huAEC medium. Immersed co-culture was carried out until day 7. ALI was started on day 7, and the models were also transferred to the wells pre-seeded with LbFb fibroblasts for the rest of the culture timeline. For all the co-culture models, the respective culture medium was exchanged three times a week. The models were then embedded in the Tissue-Tek OCT compound after days 7, 10, and 12 of ALI, and stored at -80°C .

An alternative cell seeding approach was additionally explored to assess if there is an influence of factors associated with huAEC on the migration of hEC inside the membrane, especially for PA and PCL:PTMC 70:30 membrane variants. Here the cell seeding scheme was altered such that huAEC cells (2×10^5) were seeded first on day 1 and cultured for 5 days solely, and on day 5 hEC cells (1.5×10^5) were seeded on the basal side by inverting the model. Such immersed culture was further carried out with the same optimised co-culture medium for more than 3 days, followed by ALI culture. Similar to the above, the co-culture models were transferred to wells pre-seeded with LbFb fibroblasts on the start day of ALI and cultured for 12 days. The models were then embedded in the Tissue-Tek OCT compound after days 7, 10, and 12 of ALI and stored at -80°C .

All experimental models were repeated thrice using exact same conditions and cell seed numbers.

2.2.4 Histological and functional characterisation

Tissue handling and sectioning

Tissue samples were either cryo-embedded or paraffin-embedded for histological analysis. For cryosectioning, tissue samples were embedded in Tissue-Tekcryomolds, and frozen at -80 °C. The frozen tissue was sectioned into 10 μm slices using a Leica Kryostat CM1950 and mounted on glass slides. Paraffin embedding was primarily used for PET models co-cultured with Calu3 and A549 cells. After formalin fixation, samples were incubated at 60 °C for 1 h to melt the paraffin and deparaffinized using two rounds of xylene (10 min each). Rehydration was carried out through a series of ethanol solutions: 96 %, 70 %, and 50 % (three dips each), followed by rehydration in distilled water. This was necessary for both frozen and paraffin-embedded tissue, ensuring the sections were adequately prepared for staining.

Hematoxylin and Eosin (HE) staining

Haematoxylin and eosin (HE) staining was used for general tissue morphology assessment. The slides were first incubated in haematoxylin for 5 min, staining the nuclei dark blue. After thorough rinsing under running water, the slides were differentiated with a 1-second dip in acid alcohol and immediately washed in water. Eosin was applied for 2 min to stain the cytoplasm pink. The slides were subsequently dehydrated through a graded ethanol series (50 %, 70 %, and 96 %) and cleared using two rounds of xylene for 5 min each. It is critical that after each staining step, the slides were drained properly to avoid cross-contamination between the reagents. Once the slides were clear of excess xylene, they were mounted using a permanent mounting medium and left to dry for analysis under light microscopy (EVOS XLCORE, Invitrogen).

Alcian Blue (AB) staining

Alcian blue staining was performed to highlight acidic mucins in the tissue sections. First, the slides were briefly wetted in ddH_2O and then immersed in Alcian blue solution for 30 min at room temperature. Alcian blue binds to negatively charged sulfated proteoglycans. After staining, the slides were washed 2–3 times in fresh water ddH_2O to remove any excess dye. The slides were counterstained with nuclear fast red for 5 min to stain the nuclei. Following a ddH_2O wash, the slides were dehydrated through a series of ethanol solutions (70 % and 96 %) and isopropanol, with each step lasting between 2 - 5 min. Finally, the slides were cleared using two

xylene baths, each for 5 min, and mounted with entellan. The slides were dried overnight in a fume-hood and analysed using light microscopy.

Immunohistochemical staining

Immunohistochemical (IHC) analysis was conducted using the Super Vision 2 HRP Kit. Following deparaffinization and rehydration, the slides were incubated in a blocking buffer (0.5 % BSA in PBS) for 1 h at room temperature to block non-specific antibody binding. The primary antibodies were applied to the tissue sections, and negative controls were included by using mouse or rabbit IgG at the same concentrations as the primary antibodies. After primary antibody incubation, the slides were washed three times in PBS to remove any unbound antibodies. The secondary HRP-conjugated antibodies were applied, and detection was performed using DAB substrate, which develops a brown signal for antigen detection. It is important to note that the DAB kit components, including yellow and red polymer solutions, are light-sensitive, and these steps were conducted in low-light conditions to prevent degradation of the reagents. Following DAB development, the slides were counterstained with haematoxylin, dehydrated through the ethanol series, cleared in xylene, and mounted for brightfield analysis under a light microscope.

Immunofluorescence staining

Immunofluorescence was performed for specific proteinlocalisationn within tissue sections. The tissue was first fixed in 4 % paraformaldehyde for 10 min and washed three times in PBS. Blocking was carried out with a 5 % FBS and 1 % BSA solution in PBS for 1 h. Primary antibodies were diluted in 0.5% BSA in PBS and incubated with the sections overnight at 4 °C. The slides were washed three times in PBS containing 0.5 % Tween-20 to remove unbound primary antibodies. Fluorescent-labeled secondary antibodies were applied for 1 h at room temperature. Since fluorescently labeled antibodies and DAPI (used for nuclear staining) are light-sensitive, these steps were performed in the dark. After washing, the slides were mounted using antifade DAPI mounting medium and imaged immediately using a ZEISS Axio Observer fluorescence microscope. Immediate imaging was critical, as prolonged storage could lead to a reduction in fluorescent signal intensity.

These comprehensive protocols ensure that tissue morphology, mucin composition, and specific protein localisation can be accurately assessed, providing a detailed understanding of the 3D tissue models used in this study.

2.2.5 Permeability analysis- FITC dextran assay

Fluorescein isothiocyanate-dextran (FITC-dextran) permeability assay

FITC-dextran permeability assay was performed selectively for alveolar co-culture models of hEC-huAEC-LbFB, established on both variants of PCL:PTMC at days 7, 10, 14, 21, 28, 32; PCL:PTMC 50:50 membrane-based models; for PA models at days 7, 10, 14, 21, 28 and for PET-based models at days 7, 10, 14 of ALI cultures. Additionally, the same assays were also performed for Calu-3 - pFb and A549 - pFb co-culture models on PET membrane on days 9, 11 and 14. Briefly, a sterile solution of 50 mg/ml was prepared in *ddH₂O* to form a stock solution according to the manufacturer's protocol. The Working solution was at a concentration of 1 mg/ml FITC-dextran (avg. mol. wt. 4000, FITC:Glucose = 1:250) in the respective co-culture medium. Membrane models were transferred to a new well plate, and 0.6 ml of FITC-dextran working solution was added to the inserts on top of the membranes and 1.2 ml of respective co-culture medium was added underneath. The plate was covered in foil to be secured from light exposure and incubated in the incubator for 60 min (37 °C, 5 % CO₂, 98 % humidity). Afterwards, 300 μ l samples from the medium underneath the models were plated in 96-well black, clear bottom plate in triplicate for analysis. The membrane models with cells were then washed once with the medium and transferred back to their respective wells with the fresh medium underneath. For negative control, the pure co-culture medium was also plated alongside the samples in triplicates, along with a concentration series of FITC-dextran solutions going from 1 mg/ml to 7.8215 μ g/ml as reference. The fluorescence was measured in Tecan SPARK microplate reader with respective software, with excitation and emission wavelengths optimised at 482 / 525 nm. Each experiment was minimally repeated twice for FITC-dextran assessments with additional controls of the membranes without cells. The data were corrected for the fluorescence values of the pure medium and a calibration curve was plotted using the standard concentration series of FITC-dextran in co-culture medium, to translate the fluorescence intensity values to FITC-dextran concentrations. Non-linear curve fitting was performed using Origin-pro 2019 software to generate a standard curve and unknown FITC-dextran concentrations were calculated by the software at 99 % confidence interval. The apparent permeability was calculated using formula below.

$$P_{\text{app}} = \frac{\frac{dQ}{dt}}{C_0 A}$$

dQ - accumulated FITC-dextran in mg in the acceptor compartment (i.e., the well)
 dt - duration of the assay in seconds (3600 sec)

C_0 - initial concentration of FITC-dextran in the donor compartment (the insert) in mg/cm^3 ($1\ mg/cm^3$)

A - the surface area of the membrane, i.e., $1.12\ cm^2$ (for PET membranes)

2.2.6 Protein and mucin content analysis of tissue-derived mucus

Mucus production and isolation

Tissue models using co-culture of Calu-3 and pFb were separately set up in parallel for mucus extraction at the end of weeks 2, 3, and 4. Various methods were explored to isolate mucus without disrupting the inner cellular layer on the scaffold.

Mucus isolation using Acetylcysteine (ACC) solution incubation:

The ACC tablet contained 600 mg of acetylcystein, which was dissolved in 20 ml of 1x PBS-. In the pilot experiment, to access an appropriate time point for mucus dissolution, 500 μ l of this working solution was incubated over the tissue models for varied time points of 5, 10, 20, 30, and 60 min. The mucus, hence dissolved, was stored at -20 °C in clean reaction tubes until further use.

Mucus isolation using PBS- solution incubation:

PBS- solution in 1X concentration was warmed in a water bath to a temperature of 37 °C. In the pilot experiment to assess the appropriate volume of PBS- solution to dissolve the thick mucus fibrous strands, varying volumes were analysed, and 400, 500, and 1000 μ l were incubated for 20 min. To retain mucus void of extra water content, after extraction of all the mucus from models in a 15 ml centrifuge tube, the solution was centrifuged at 2500 rpm at 4 °C for 5 min, and the supernatant water was collected separately for further analysis.

Protein content quantification using Bradford Assay

The Bradford assay using Coomassie Brilliant Blue G-250 was performed according to the standardised SOP. Briefly, the dye binds to the proteins present in the sample. This photometric method quantifies the protein concentration in the sample in proportion to the measured dye absorption. Protein concentrations in mucus samples were determined using a modified Bradford Assay in a 96-well plate format. Bovine Serum Albumin (BSA) standards ranging from 3000 to 0 μ g/ml were prepared using [ACC] and PBS- as the diluent to match the conditions of the mucus samples. Samples and standards (5 μ l) were added to the wells, followed by 250 μ l of Bradford reagent. The plate was shaken for 30 seconds and incubated at room temperature for 45 min. Absorbance was measured at 595 nm using a microplate reader. Blank wells were prepared using the same dilution buffers as used in the sample preparation.

Westerblot analysis for mucin proteins Muc5AC and Muc5B

After protein quantification via Bradford assay, samples were subjected to SDS-PAGE. Initial optimisation involved testing different gel concentrations: 4 - 7 %, 4 - 8 %, and 4 - 5 % (1 mm thickness), with 4 - 5 % gel yielding optimal results. Laemmli buffer (5x) was prepared using Tris-HCl (pH 6.8), SDS, glycerol, bromophenol blue, and β -mercaptoethanol, added fresh before use. Gel electrophoresis was run at 85V for 20 min followed by 105V for 1 h 20 min. Following SDS-PAGE, proteins were transferred to PVDF membranes using the Trans-Blot Turbo system. Two settings were optimised: 7 minutes for mixed molecular weights (5 - 150 kDa) and 10 minutes for high molecular weights (>150 kDa). Membranes were blocked in 3% BSA/TBST and incubated with primary antibodies: Muc5AC (mouse, 1:1000), Muc5B (mouse, 1:1000), and SFTPC (rabbit, 1:1000). After an additional blocking step, detection was performed using HRP-conjugated secondary antibodies and ECL substrate. The membranes were visualised using a Bio-Rad ChemiDoc system. Samples were collected from ACC-incubated mucus proteins dissociated at various time points (5, 10, 20 min...60 min).

2.2.7 Physical and rheological methods for mucus characterisation

Surface tension analysis

In order to measure the surface tension of the mucus produced from the tissue samples, in two different ways. One with the mucus samples extracted from the tissue models and within intact tissue models with a mucus layer, in varying thickness from week 2 to week 4. All measurements were performed using force tensiometer (Krüss, BP100 tensiometer). To adjust the humidity inside the instrument, a special 3D-printed circular vessel mould designed containing a specific salt solution to increase the humidity was used and measured using a humidity sensor. The sample holder was heated to a 37°C temperature. The measurement was performed with the help of preset settings for Du Noüy ring surface tension measurement method, using software provided by the manufacturer, ADVANCE KRÜSS, for the small ring RI02 measurement probe. Samples measured include Airway tissue models (1 week to 4 weeks), *ddH₂O*, SDS 50 mM, SDS 20 mM, S1- Mucus ex. 400 μ l PBS-, S2-Mucus ex. 500 μ l PBS- (17x samples), S3-Mucus ex. 1 ml PBS- (4 Wk 15x models), and lung lavage. Briefly, the below modifications were done in the measurement presets according to the designated measurement parameters.

Static Force Measurement:

To determine the appropriate lamella height for surface tension measurements, static force measurements were initially performed using the small RI02 ring on the Krüss BP100 Bubble Pressure Tensiometer. In this procedure, the lamella height was pre-stretched to 2 mm while the ring remained stable, and the base plate was slowly moved away. The force exerted over the lamella was recorded until rupture. This step provided insights into the optimal lamella height and other critical parameters for subsequent surface tension measurements. The sample holder used had a 15 mm diameter with a PTFE bottom, and a sample volume of 200 μ l was consistently maintained. Pre-wetting of the sample was performed for 5 seconds before each measurement to ensure consistency.

Surface Tension Measurement:

After determining the optimal lamella height, surface tension measurements were carried out using the Du Noüy ring method. For these measurements, the RI02 ring was repetitively immersed in the mucus samples. The sample volume was maintained at 200 μ l, and the same 15 mm diameter sample holder was used. During the measurement process, the software plotted the force represented as the weight of a mass measured in grams over time (seconds) until the lamella broke. Irregularly high initial values were discarded and only stable, repetitive measurements were

considered. The average surface tension (ST) for each sample was calculated from multiple repetitions (at least three per model), with data analysed in MS Excel. Measurements were performed for mucus isolated from tissue models at various time points (weeks 1 to 4), as well as control samples such as *ddH₂O* and SDS at 20 mM and 50 mM.

For surface tension, a data plot of weight (g) vs. elapsed time (s) until the lamella break was plotted by the software. Random high values lacking repetition at the start of the measurement were not considered for taking an average of ST values for the sample. ST values only for the repetitive periodic measurements are considered, and average ST is calculated for each model and respective repetition, and ST was measured automatically by the software. Each model variant was repeated at least three times for measurements. Such ST data going for mucus isolated from week 1 to week 4 models were measured and calculations were made using MS Excel software.

Viscosity measurement

Given the non-Newtonian nature of mucus, relative viscosity measurements were performed using a stress-controlled rotational rheometer (MCR 301, Anton Paar). Non-Newtonian fluids, like mucus, display variable viscosity depending on the stress applied [84]. The mucus samples used in this experiment were extracted with PBS at various volumes (1000 and 500 μ l) from tissue models at weeks 3 and 4. The first set of measurements conducted was an amplitude sweep, designed to evaluate the deformation (strain) percentage across a range of 0.1 % to 10 %. This process was performed using circular plates of 50 mm in diameter [66, 84]. The experiments were conducted at two different temperatures, 25 °C and 36 °C, to simulate conditions relevant to biological systems. The second set of measurements was a frequency sweep, which examined the response of the samples over an angular velocity range of 0.1 to 100 rad/s. Several parameters were analysed during the rheological testing. In the oscillatory rheological measurements, the storage modulus (G') and loss modulus (G'') are measured. The storage modulus (G') reflects the elastic, or solid-like, behaviour of the mucus, indicating its ability to store energy when subjected to deformation [84]. The higher the G' value, the more the sample behaves like a solid. The loss modulus (G''), on the other hand, represents the viscous, or liquid-like, behaviour of the sample, describing the energy dissipated as heat during deformation [66, 84]. The viscosity of non-Newtonian fluids can depend on shear rate or shear strain and can be time-dependent or stress-dependent. Hence while studying the rheological behaviour of fluids in oscillatory shear conditions (i.e., when subjected to a time-varying stress or strain), calculating

the magnitude of complex viscosity can prove particularly relevant in the context of viscoelastic fluids like mucus that have both viscous and elastic characteristics [84]. The complex viscosity (η^*) as a function of shear rate was calculated as it combines both elastic and viscous components, giving a comprehensive measurement of the material's overall resistance to deformation under oscillatory shear conditions [84].

- G' (Pa) (Storage Modulus): elastic (solid-like) behaviour of the material
- G'' (Pa) (Loss Modulus): viscous (liquid-like) behaviour of the material

Complex Viscosity $\eta^*(\omega)$:

For non-Newtonian fluids, particularly viscoelastic materials, the relationship between stress and strain is more complex [84]. When the fluid undergoes oscillatory shear, its response can be decomposed into elastic and viscous components. The complex viscosity is used to characterise the combined effect of these two behaviours [84].

$$\eta^*(\omega) = \eta'(\omega) + i\eta''(\omega) = \frac{G^*(\omega)}{\omega}$$

where,

$$G^*(\omega) = G'(\omega) + iG''(\omega)$$

and $\eta'(\omega)$ known as effective shear or dynamic viscosity in Pa. s can be calculated using:

$$\eta'(\omega) = \frac{G''(\omega)}{\omega}$$

Amplitude sweep measurements repeated for different angular frequencies (1, 5, 10, 50, 100 rad/s) were used to generate respective plots for G' (Pa) vs. strain amplitude (%), G'' (Pa) vs. strain amplitude (%), and plots for shear viscosity vs. strain amplitude (%) using MS Excel software. After determining the optimal linear range, frequency sweep was also repeated for different strain amplitudes (1, 2, 5, 10 %) and data plots for G' (Pa), G'' (Pa) and calculated dynamic viscosity were plotted.

In the next step, the loss angle delta was calculated using frequency sweep data for storage and loss modulus using the formula:

$$\delta = \arctan\left(\frac{G''}{G'}\right)$$

Initially, tangent δ was calculated using the ratio of G'' to G' at each frequency value for different strain amplitudes. To calculate the loss angle δ , arc-tangent was calculated from the tangent δ values. These δ values in radians were then converted to degrees and plotted against the shear rate (frequency).

2.2.8 Statistics

All the respective models were repeated thrice for FITC-dextran measurements and mucus thickness measurements. FITC-dextran was averaged over the three repetitions with 4 technical replicates. Non-linear curve fit analysis was performed on FITC data to obtain the standard curve and the unknown concentrations using OriginPro 2019. Mucus thickness was determined using ImageJ Fiji. For this, three alcian blue staining images were selected randomly for each model, and the thicknesses were then averaged over. Representative images are shown in the results. Membranes without cells were tested for Young's modulus twice under the same conditions, and the average value as well as the standard deviation were obtained using MS Excel. Statistical calculations for all the rheological measurements for the mucus samples were performed using MS Excel, and the graphs were plotted using OriginPro 2019 software. The frequencies/shear rate, G' and G'' scales are depicted in logarithmic scales, while strain amplitudes are kept in linear scale.

3

Results

3.1 Materials employed as scaffolds

To design a biomimetic ECM, the influence of the scaffold composition on the cellular function and the specific cell types was explored. Therefore, in the first step, different biological and synthetic materials were manufactured into plane scaffolds and characterised. These included the widely known biological scaffold small intestinal submucosa with mucosa (SIS-Muc), commercially available artificial scaffolds, 2D membrane scaffolds using PET as well as fibrous scaffolds made of PCL and PTMC.

SIS-Muc:

The decellularization procedure and characterisation of a porcine jejunum segment using sodium deoxycholate and perfusion of an intact vessel network within the intestinal wall were published [81]. characterisation revealed that the scaffold with a thickness of 0.2 ± 0.01 mm was comprised of approximately 5 % elastin and 92 % cross-linked collagen fibres.

3.1.1 Analysis of synthetic polymer-based scaffold membranes

Pure PTMC polymer was challenging to prepare as solutions for the electrospinning settings and hence was mixed in two different proportions with stabilising PCL polymer. PCL polymer at a 14 % concentration was also electrospun into thin membrane sheets and showed a distinctive porous structure as shown in fig. 3.1. Given the brittleness, high Young's modulus, and less flexible behaviour of the PCL membrane fibre, as a result, electrospun pure PCL (14 % (m/v) total polymer concentration) membrane was seen degrading while in co-culture with epithelial cells and endothelial cells leaving it unsuitable in its pure form. Hence, when mixed with PTMC polymer, after electrospinning, PCL:PTMC 70:30 mix membranes appeared to have irregular fibrous structures with variable porous formations, as

seen in fig. 3.1. PCL:PTMC 50:50 was seen having homogenous fibrous strands and dense fibrous networks when compared to that of the previous membrane mix as depicted in fig. 3.1.

Fig. 3.1 (G-H) show SEM images taken for PA polymer membrane synthesised using a similar electrospinning method (12 % polymer concentration). The polymer fibres appear to have almost the same thickness and diameter. the fibre arrangement can be seen as randomised, providing non-uniform pore structures and sizes. The fibre diameter and thickness appear uniform and homogeneous when compared with PCL:PTMC 70:30 membrane (fig. 3.1 (E-F)). Compared to PCL:PTMC 50:50 membrane (fig. 3.1 (C-D)), PAG membrane polymer fibres appear to have nicely curved structures, whereas for PCL:PTMC 50:50 they are with almost straight fibre structures overlaying randomly. Noticeably, PA membrane structures, as shown in fig. 3.1 (H), have comparatively minute porous formations than in PCL:PTMC 50:50 (fig. 3.1 (D)) and PCL:PTMC 70:30 (fig. 3.1 (F)).

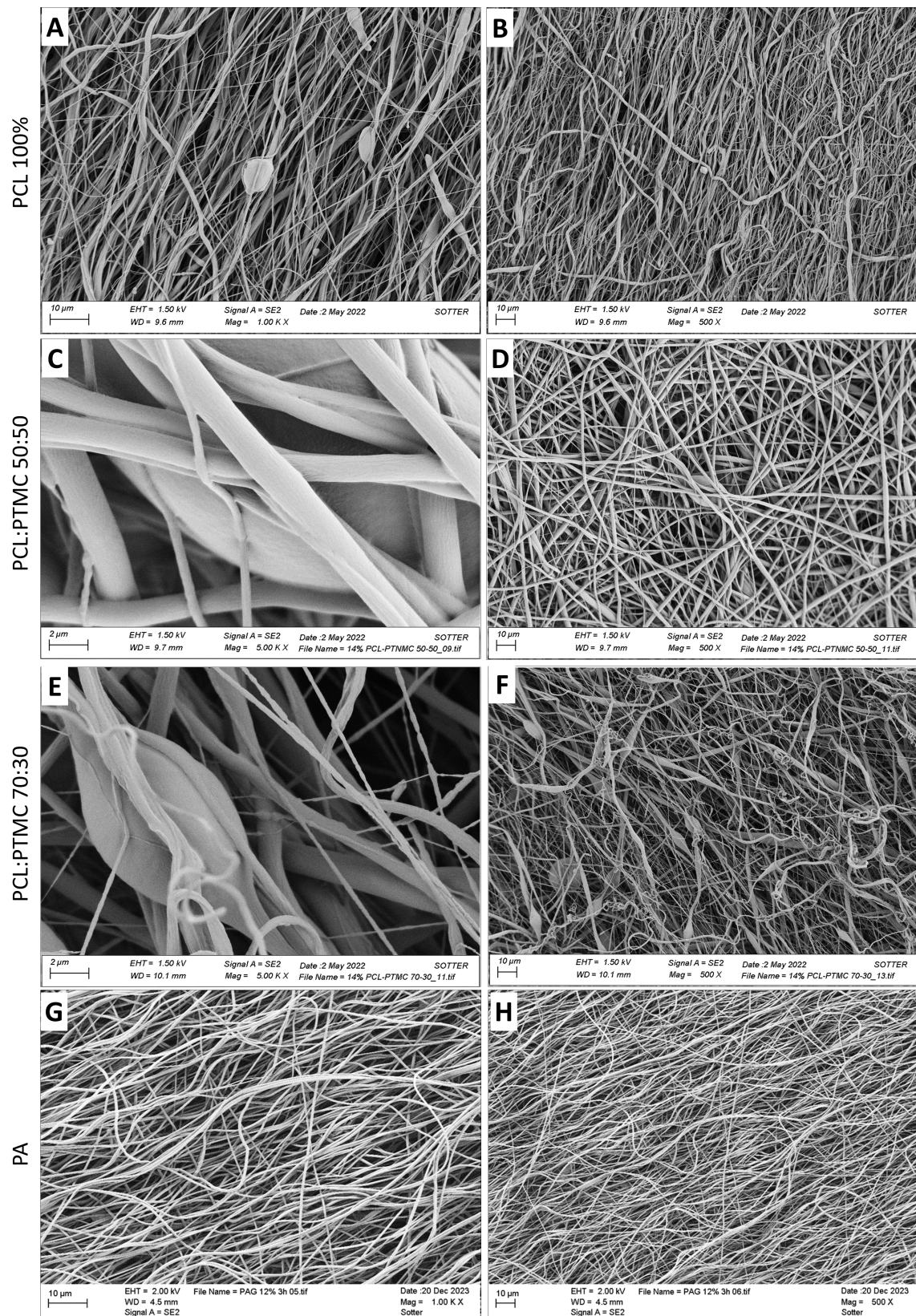


Figure 3.1: SEM images of the polymeric scaffold structures; pure PCL (A,B), PCL:PTMC 50:50 (C,D), PCL:PTMC 70:30 (E,F), PA (G,H) [6].

Figures depict differences observed in the porous structures generated through randomised fibre alignment as well as variations seen in the fibre structure. (A, C, E, G) are the magnified images of the respective electrospun polymer membranes in the (B, D, F, H) [6].

3.1.2 Mechanical properties: Tensile strength and Modulus of Elasticity

The measurements for assessing the mechanical properties of three membrane types—PA, PCL:PTMC 50:50, and PCL:PTMC 70:30—were repeated twice using two different sample pieces cut from the provided membrane sheet cut out from two diagonally opposite corners. The measurement area was kept consistent, having a consistent width of 3 cm and length of 4 cm. These measurements were used to calculate parameters such as Young's modulus of elastic and tensile strength. This data helps to further discuss the membranes' potential suitability for tissue modelling applications. Tensile strength values (σ) were also measured for each membrane by the preset software from the force transducer equipment, reflecting the membrane's resistance to breaking under tension. Finally, the average tensile strength values were calculated from each measurement session.

PA membrane:

Average Young's modulus of elasticity was calculated to be 0.6667 MPa in the first measurement with a standard deviation of 0.0308 indicating low variability in the measurements. In the second measurement, the average Young's modulus decreased to 0.5095 MPa. The measured tensile strength values were 3.228 MPa and 3.187 MPa for the 1st and 2nd samples, respectively. Overall, Young's modulus of elasticity for the PA membrane was averaged to be 0.5881 MPa with a minimum standard deviation of 0.0786, showing minimal variability within this test. PA membrane samples exhibited an average tensile strength of 3.2075 MPa, with a standard deviation of 0.0205.

PCL:PTMC 50:50:

In the same conditions for measurement 1, PCL:PTMC 50:50 membrane showed the average Young's modulus at 0.1794 MPa, with a standard deviation of 0.00995, showing relatively consistent readings. In measurement 2, the average Young's modulus for the PCL:PTMC 50:50 membrane was slightly lower at 0.1695 MPa, and the standard deviation was only 0.0067 suggesting even greater consistency within this test series. The measured tensile strength values were 0.145 MPa and 0.5000 MPa for the 1st and 2nd samples, respectively. Overall, Young's modulus of elasticity for PCL:PTMC 50:50 membrane was averaged to be at 0.174475 MPa, with a standard deviation calculated of only 0.0049. PCL:PTMC 50:50 membrane samples exhibited an average tensile strength of 0.3225 MPa, with a higher standard deviation of 0.1775.

PCL:PTMC 70:30:

PCL:PTMC 70:30 membrane, a blend with a higher proportion of PCL (70 %) and a lower proportion of PTMC (30 %), displayed a broader range of Young's modu-

lus values across the two measurement samples. Under the same measurement conditions as the previous membrane measurements, here the average Young's modulus was calculated to be 0.1371 MPa, with a standard deviation of 0.00285, indicating low variability. In measurement 2, however, the Young's modulus for the PCL:PTMC 70:30 membrane dropped to an average of 0.04495 MPa, while having a very low standard deviation of 0.00015, showing a high level of consistency within this test session. Observable hollow pores were seen before measurements in the cut membrane sample during the second measurement, suggesting variability produced during the electro-spinning process. This led to unexpected breakage near the hollow points during the measurement run, hence questioning the reliability of measurement 2 values. The measured tensile strength value was 0.153 MPa and 0.183 MPa for the 1st and 2nd samples respectively. Overall, Young's modulus of elasticity for PCL:PTMC 70:30 membrane was averaged to be at 0.09105 MPa, with a standard deviation calculated of only 0.0461. PCL:PTMC 70:30 membrane samples exhibited an average tensile strength of 0.183 MPa, with noticeably no standard deviation.

The tables below summarise the key values obtained for each membrane variant analysed for mechanical properties, namely modulus of elasticity and tensile strength. The highlighted yellow values correspond to unexpected variations, which may lead to errors in further analysis of the membrane properties.

Table 3.1: Calculated Young's modulus of elasticity and tensile strength for each synthetic electrospun membrane variant

Membrane	Measurement 1 (std. dev) MPa	Measurement 2 (std. dev) MPa	Young's modulus (Average) MPa	Standard deviation (MPa)
PA	0.6667 (0.0308)	0.5095 (0.0332)	0.5881	0.0786
PCL:PTMC 50:50	0.1794 (0.0099)	0.1695 (0.0067)	0.1745	0.0049
PCL:PTMC 70:30	0.1371 (0.0028)	0.0449 (0.0001)	0.0910	0.0461
Membrane	Measurement 1 (std. dev) MPa	Measurement 2 (std. dev) MPa	Tensile strength (Average) MPa	Standard deviation (MPa)
PA	3.228	3.187	3.2075	0.0205
PCL:PTMC 50:50	0.145	0.500	0.3225	0.1775
PCL:PTMC 70:30	0.153	0.183	0.183	0

3.2 *In vitro* airway tissue models

The human airway system depicts heterogeneity and can be roughly divided into upper, lower, and alveolar regions. The regions exhibit distinct architectural, cellular, and functional properties, driven by both their cellular composition and basement membrane characteristics. As shown in fig. 1.1, these regional variations include differences in epithelial cell types, histological structures, and basement membrane thickness, which is critical for functions ranging from mucus production to gas exchange. To assess the impact of scaffold material on tissue development and cellular behaviour, various co-cultures were established, each representing distinct lung regions. These model configurations, including cell types and scaffold specifics, are summarised in table 3.2 below.

Table 3.2: Overview of biological and polymeric scaffolds for culturing different lung tissue locations. Upper lung location comprised of trachea/bronchi (conducting airways) and lower lung location consisting of terminal bronchioles and Alveolar locations (gas exchange area) [6]

Scaffold material	Lung location	In vivo thickness (reqd.) (μm)	Co-culture cell composition
SIS-Muc	Upper	~50 - 100	Calu-3 + fibroblasts
PET	Upper	~50 - 100	Calu-3 + fibroblasts
	Lower	~10 - 50	A549 + fibroblasts
	Alveolar	~10 - 0.2	huAEC + fibroblasts (lung biopsy)
	Alveolar	~10 - 0.2	huAEC + endothelial cells
PCL	Alveolar	~10 - 0.2	huAEC + hEC + fibroblasts (lung biopsy)
PCL:PTMC (70:30)		~10 - 0.2	
PCL:PTMC (50:50)		~10 - 0.2	
PA		~10 - 0.2	

For the upper airway model, SIS-Muc scaffolds were seeded with Calu-3 epithelial cells and co-cultured with primary human fibroblasts to develop an epithelium typical of the trachea and bronchi. PET membrane Thincerts® were used to construct models of both upper and lower airway structures using Calu-3 and A549 cells with fibroblasts, respectively. To capture the unique features of alveolar tissue, electrospun synthetic polymer-based scaffolds PCL:PTMC (50:50 and 70:30 ratios) as well as PA were used to model the alveolar basement membrane, along with co-cultures of human alveolar epithelial cells (huAECs) and human endothelial cells (hECs). LbFb fibroblasts were also incorporated to support the epithelial-endothelial interface.

The following sections will describe the in-depth investigation of scaffold influence on tissue-specific cell behaviour and organisation across different *in vitro* tissue models.

3.3 Characterisation of *in vitro* tissue models

Upper airway region

3D *in vitro* tissue models for the upper airway (trachea and upper bronchial region) were modelled using thicker biological scaffold material SIS-Muc with a co-culture of Calu-3 and pFb. Alcian blue staining illustrated the mucus formation over time, starting from 1 week to 4 weeks after ALI culture initiation (fig. 3.2 (A-D)). After 1-week culture, epithelial cells formed a monolayer over the SIS-Muc while the fibroblasts started to migrate into the scaffold (fig. 3.2 (A)). Simultaneously, a very thin layer of mucus of approximately $30 \pm 5 \mu\text{m}$ was present, covering the epithelial monolayer (fig. 3.2 (A)). Similar observations were found after 2- and 3-weeks ALI culture (fig. 3.2 (B, C)). It was observed that the mucus stained in blue gradually increased to approximately $80 \pm 5 \mu\text{m}$. After 4 weeks of ALI cultures, epithelial cells were forming multiple layers (2 - 3 layered) (fig. 3.2 (D)), while an approximately $505 \pm 5 \mu\text{m}$ thick layer of mucus (N=3) was present.

Lower airway region

To compare cellular behaviour concerning the thickness of the scaffold and progression of mucus production, similar models were optimised using PET Thincerts® $22 \pm 3 \mu\text{m}$. Culture conditions were set similarly to those described above for models using SIS-Muc, with fibroblasts in the bottom part of the Thincert® membrane in contact with the co-culture medium and epithelial Calu-3 cells on the apical part, which was exposed to air. Fibroblasts adherent on the bottom side of the Thincerts® formed a confluent monolayer (fig. 3.2 E - I). At the end of the second week, a mono-layered epithelial layer of Calu-3 cells was observed (fig. 3.2 (F)). Similar progressive mucus formation was observed from week 1 to week 4 using alcian blue staining (fig. 3.2 (E-H)). The mucus layer thickness increased from approximately $41 \pm 5 \mu\text{m}$ at week 2 to $128 \pm 5 \mu\text{m}$ at week 4.

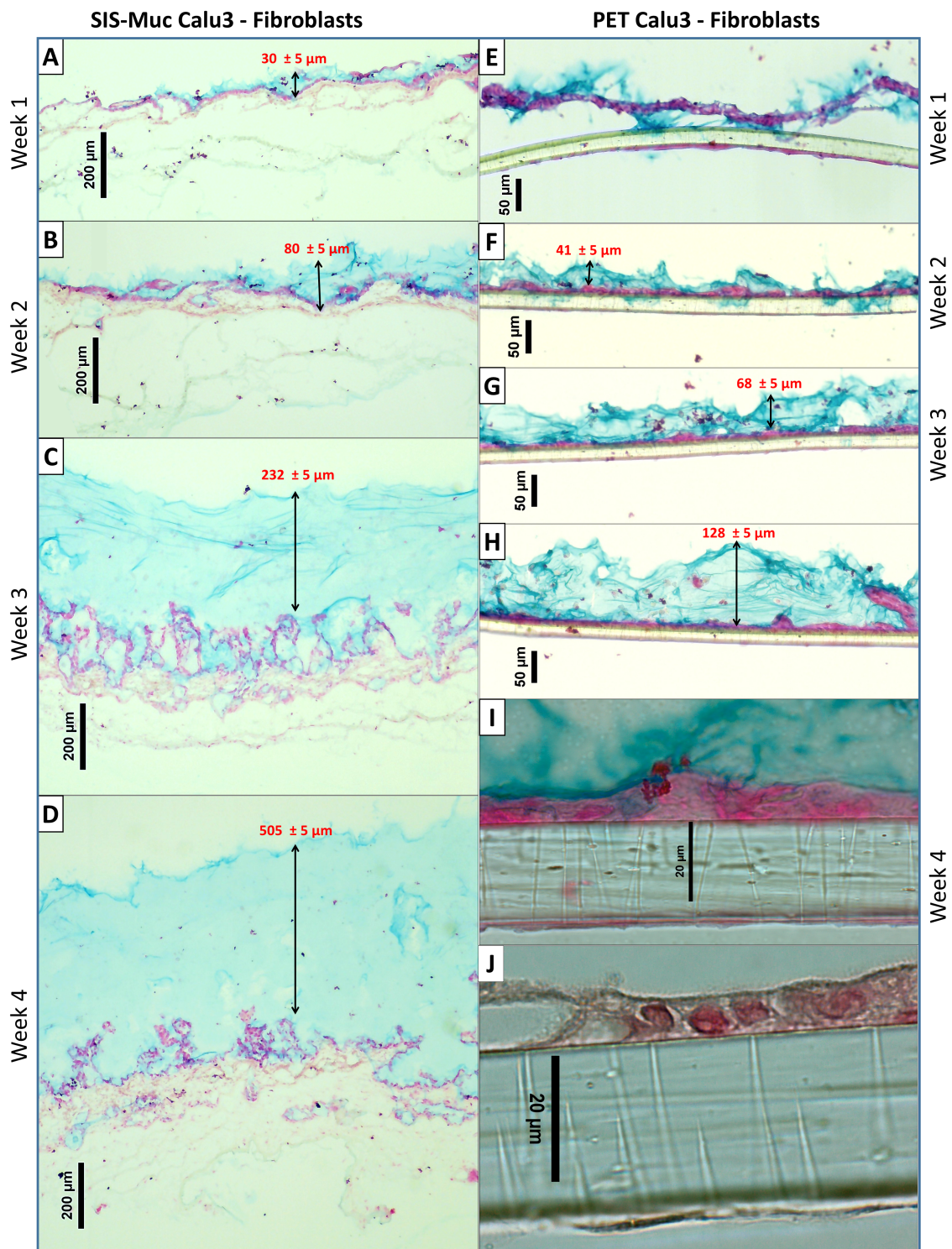


Figure 3.2: 3D airway models using Calu-3 cells and human primary fibroblasts cultivated over 4 weeks *in vitro* on SIS-Muc scaffold (A-D) and PET Thincerts® membranes (E-J) [6].

Alcian blue staining shows acidic components in the mucus-stained blue and an increasing mucus layer thickness as the ALI cultures progress from 1 week to 4 weeks. Cellular structures are stained in red, while the rest of the scaffold is discoloured.

Furthermore, a co-culture model of A549 cells and pFb on SIS-Muc revealed marginal staining of acidic structures (blue) at the end of 4 weeks (fig. 3.3 (A)) compared to the Calu-3 cell model (fig. 3.3 (C)). A549-pFb co-cultures on SIS-Muc, also showed cellular multilayering (more than 4 layers). Similarly, co-culture of A549 - pFb on PET membrane Thincerts®, used to mimic lower airways, was established and stained with alcian blue staining for 3, and 4 week models. Interestingly, by weeks 3 and 4, A549 cells were forming multiple layers (3-4 layers), while no mucus formation was verifiable in the alcian blue staining (fig. 3.3 (B)).

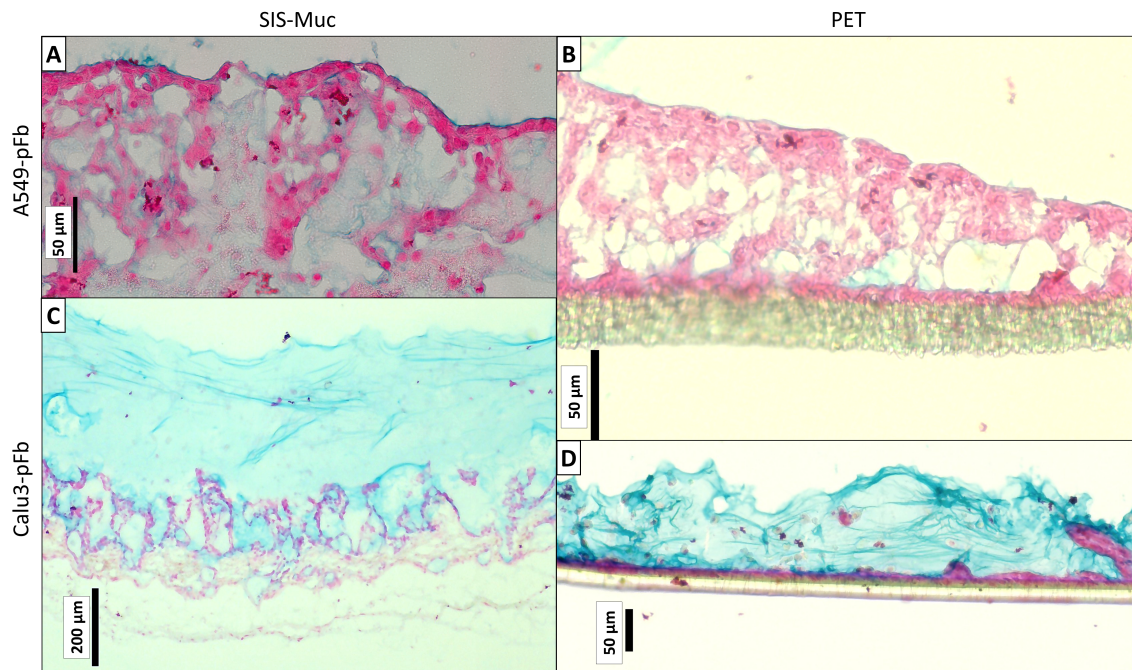


Figure 3.3: Distinct multi-layering patterns and mucus formation in co-cultured A549 and Calu3 tissue models on different scaffolds are shown by alcian blue staining [6].

(A, B) A549 cells co-cultured on SIS-Muc and PET membrane, respectively, after 4 weeks presenting marginal blue staining but strong red staining. In contrast (C, D) Calu-3 cells co-cultured on SIS-Muc and PET, respectively, after 4 weeks. Blue indicates acidic mucus formations, while cellular structures are stained in red.

Tissue sections from A549 co-culture models on PET membrane were stained for ZO-1 tight junction protein. As shown in the fig. 3.4 (B), in IHC staining, no distinct positive signal was present. This was also confirmed in IF staining against ZO-1. When stained for tight junction protein ZO-1 expression using TRITC conjugate secondary antibody (refer table 3.3), was also absent, but cells appeared multilayered as stained positively by DAPI-stained blue nuclei.

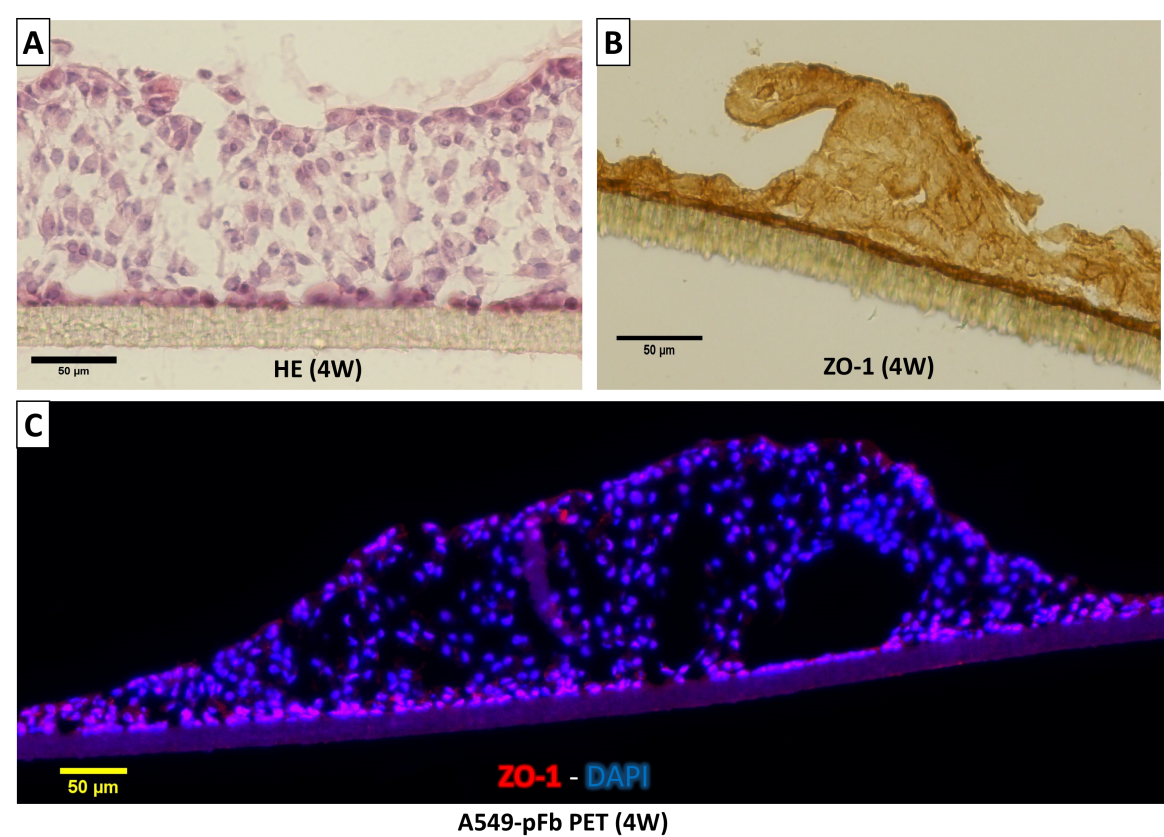


Figure 3.4: Lower airway models on PET membrane: coculture of A549-pFb: showing multilayering [6].

(A) HE staining showing multilayering of A549 epithelium. (B) IHC staining against ZO-1 showed no tight junction positive signals. (C) IF staining shows negatively stained ZO-1 (red) against the A549 epithelium layer along with the nucleus stained positively in DAPI (blue).

Table 3.3: Differences in mucus formation, cellular multi-layering, and ZO-1 expression in the airway models using standard cell lines for upper and lower respiratory tract [6].

Scaffold material	Epithelial cell line co-cultures	Mucus formation	Cell-multilayer (3 layers)	ZO-1 expression for tight junction
SIS-Muc	Calu3-pFb	+++	++	++
SIS-Muc	A549-pFb	+	+++ (>3 layers)	–
PET	Calu3-pFb	++	+	++
PET	A549-pFb	–	+++ (>3 layers)	–

(+++ :strongly present; ++ :present; + :weakly present; – :totally absent)

Table 3.3 summarises observations for PET and SIS-muc based Calu-3-pFb and A549-pFb co-cultures concerning mucus formation, cell multilayering, and ZO-1 expression. In comparing PET and SIS-Muc scaffolds with Calu-3 and A549 cell co-cultures, distinct differences were observed in mucus production, cellular layering, and ZO-1 expression. Calu-3 cells on SIS-Muc showed strong mucus formation,

moderate cellular multilayering (3 layers), and ZO-1 expression, indicative of tight junctions. On PET, Calu-3 cells demonstrated moderate mucus formation and ZO-1 expression but limited layering. In contrast, A549 cells on both SIS-Muc and PET exhibited extensive multilayering with over three cell layers. However, mucus production was weak with SIS-Muc and absent on PET, and no ZO-1 expression was detected in either A549 model.

3.4 Alveolar airway models

3.4.1 Alveolar 3D tissue models on PET membrane

The second concern, establishing cell-cell interactions crucial for epithelial-endothelial communication as well as the air-blood barrier, can be mitigated by decreasing the basement membrane thickness.

In the first attempt, following the Mattek Epi-Alveolar™ model approach, models were constructed using triple culture of huAEC-LbFB (apical) and hEC (basal) sides. It was found that endothelial cells were no longer seen attached in monolayer confluency. Pan-cytokeratin, a marker for epithelial cells, and E-cadherin, a marker for adherence junctions and epithelial phenotypes of cells, were used to characterise these models using IF staining.

Our models showed pan-cytokeratin-positive epithelial cells in tightly aligned layers along with positive E-cadherin. These layers were observed to form multiple layers sandwiching fibroblasts stained positive for vimentin, as evident in the fig. 3.5. Detailed findings are then summarised in fig. 3.13. Hence, such a model may be unsuitable for long-term culture up to 3 weeks, while profound control over the monolayer formation of epithelial cells and endothelial cells is difficult and crucial.

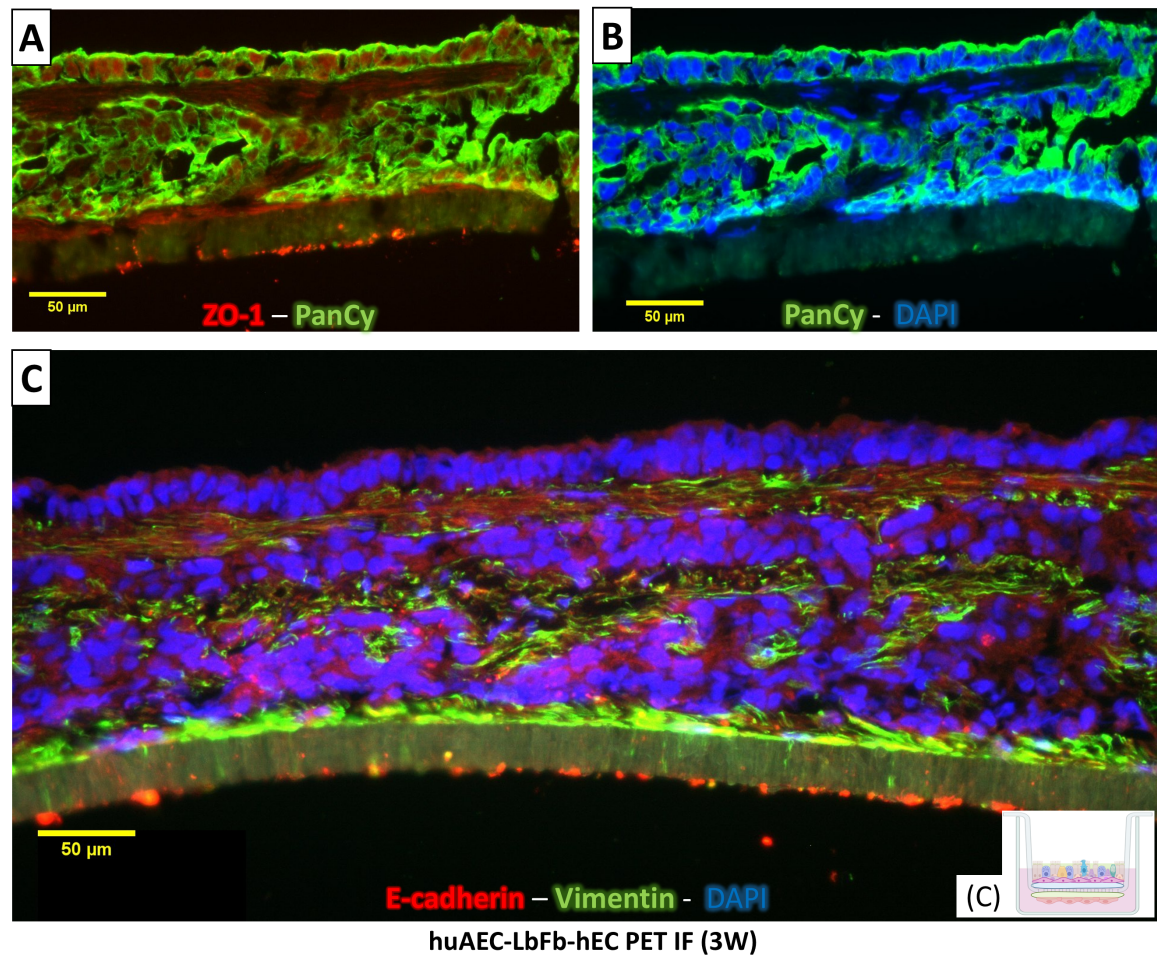


Figure 3.5: Mattek EPIAlveolar™ based models on PET membrane coculture of huAEC-LbFb-hEC: showing multilayering, as well as cellular crosstalk between epithelial as well as fibroblasts and no endothelial cell layer, be found on the basal side of the membrane [6].

(A) Pan-cytokeratin positively stained (green) huAEC with little to no ZO-1 (red) positive signals. (B) Pan-cytokeratin positively stained (green) huAEC with DAPI (blue) stained nucleus. (C) E-cadherin-positively stained (red) huAEC mixed with vimentin-positive (green) fibroblasts and nucleus stained in DAPI (blue).

3.4.2 PCL, PTMC membrane-based *in vitro* tissue models

A scaffold of approximately $0.2\ \mu\text{m}$ between the alveolar epithelium and endothelial layer is required that can facilitate gas exchange as seen in alveolar tissue structure. To achieve this, PCL and PTMC polymers were electrospun in two proportions. These membranes were then used to establish alveolar 3D *in vitro* tissue models.

Influence of inclusion of native fibroblasts and optimised coating

Initially, co-culture models based on PCL:PTMC electrospun membrane mixtures were established using huAEC coating solution for the apical side of the scaffold and 2 % gelatin coating on the basal side for hEC cells. HE staining revealed randomised cellular layers for co-culture of huAEC with hEC without the inclusion of lung biopsy-derived fibroblasts in the culture setup as shown in fig. 3.6 below. In the case of both membrane variants, the alignment of the endothelial and epithelial cell layers could not be seen.

Similar models were then established using an optimised coating solution consisting of essential proteins of human plasma protein, VEGF-165 factor. Additionally, the same co-culture model was exposed to pre-seeded lung biopsy-derived human fibroblasts (5×10^4 cells/ well) cultured in the well compartment at least for 7 days. HE staining was performed to assess cellular alignment and attachment for the co-culture models. As evident from the fig. 3.6 (C) above, the epithelial layer and endothelial layer appeared stacked and separated over each other. The epithelial cell layer appeared singularly layered, and the endothelial cells lined the bottom of the membrane.

Immune-histological staining were performed on the triple culture models hEC-huAEC-LbFb on PCL:PTMC 70:30 against CD31 endothelial cell markers for models fixed at days 7, 9, and 12. This was used to characterise endothelial cell distribution in triple-culture models on PCL:PTMC 70:30 scaffolds. In fig. 3.7 (A-C), a distinct huAEC layer is visible on the apical side, while CD31-positive hECs are seen on the basal side at day 7, with progressive migration into the scaffold by day 12. Figure D shows a negative control using mouse IgG against CD31, confirming specificity. This characterisation highlights the spatial arrangement and gradual integration of endothelial cells over the experimental period.

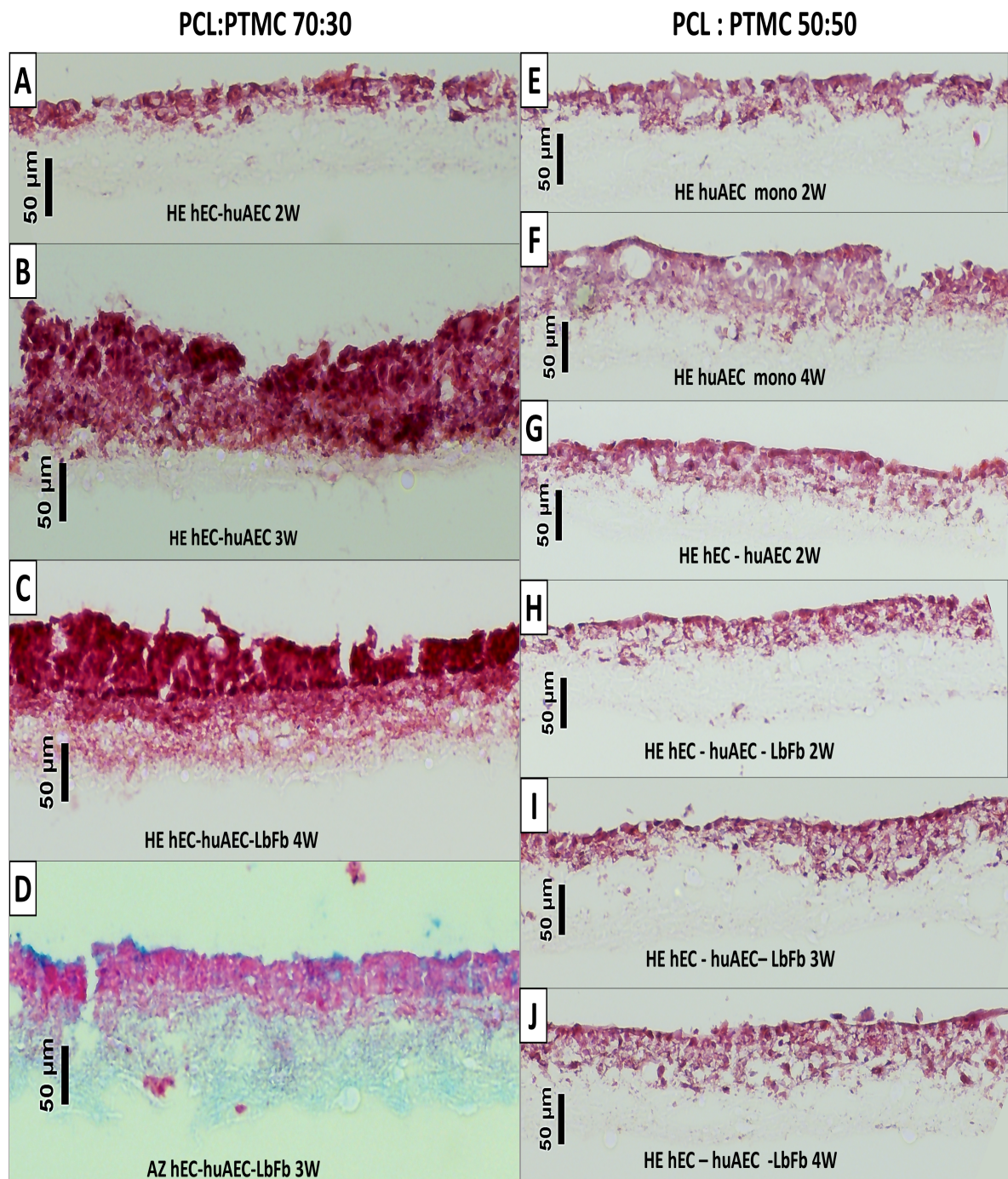


Figure 3.6: Comparison between cellular attachment behaviour for PCL:PTMC 50:50 and PCL:PTMC 70:30 membrane models. (A-D) PCL:PTMC 70:30-based models. (E-J) PCL:PTMC 50:50-based models [6].

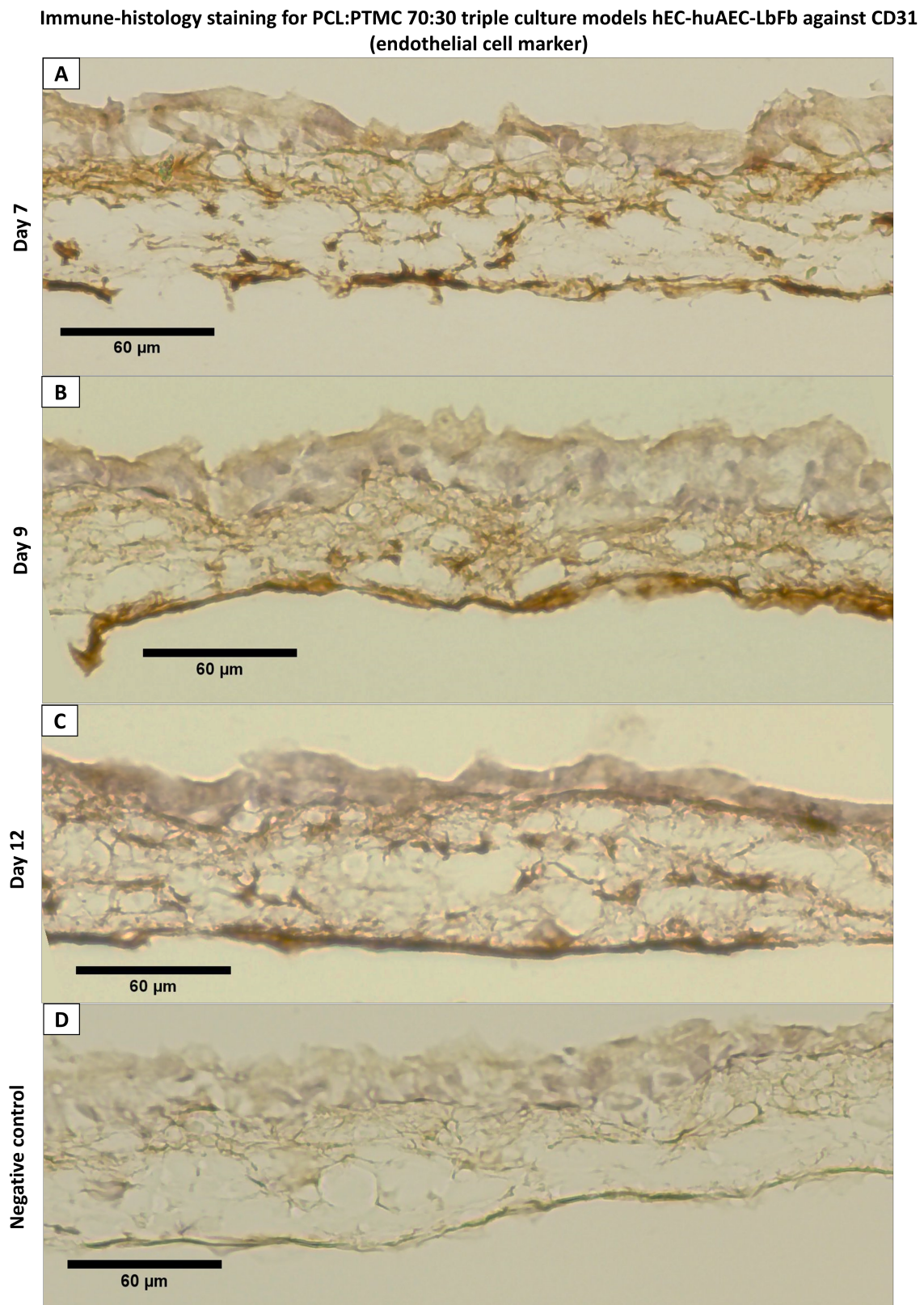


Figure 3.7: Immunehistochemical tissue characterisation against CD31 endothelial cell marker for triple culture models on PCL:PTMC 70:30 [6].

(A - C) huAEC layering on the apical side is seen clearly; CD31-positive hECs are seen on the basal side of the membrane at day 7 and gradually migrating inside until day 12 (D) negative control for host mouse (IgG mouse) against CD31.

For co-culture models established using PCL:PTMC 50:50 membrane, IHC staining was repeated for CD31 marker as well as E-cadherin to stain epithelial huAEC cells. At day 10 of the ALI culture, models showed monolayered epithelium with the epithelial cells forming a closed contact line on the apical side, as shown in fig. 3.8 (A). Although triple-culture models with PCL:PTMC 50:50 depict some blue-stained layer on top of the epithelial layer from day 10 to day 12, the epithelial layer appeared to be multi-layered by day 12 (fig. 3.8 (B)). Fig. 3.8 (C, D) shows immunofluorescence staining, done at day 12 against endothelial marker CD31 (green) and E-cadherin (red) as an epithelial marker as well as a cell-cell adhesion protein. hECs seeded on the basal side of the scaffold were found directly below the apically seeded huAECs layer, specifically on day 12, as seen in fig. 3.8(C).

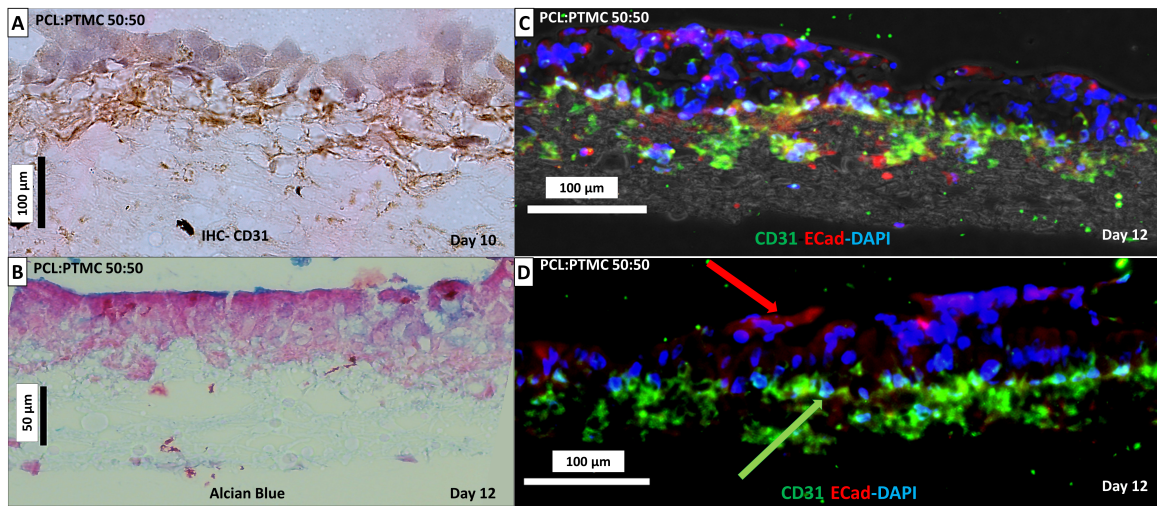


Figure 3.8: Characterisation of triple cultured tissue models (huAEC-hEC-LbFb) on PCL:PTMC 50:50 [6]

(A) Positive CD31 staining against hEC aligned below CD31-negative huAEC. (B) Alcian blue staining for models on PCL:PTMC 50:50 showing distinctive blue staining on top of multilayered epithelial layer at end of day 12, while endothelial cells were migrating inside (A,B,C). (C,D) IF staining, showing green stained CD31-positive hECs, blue DAPI-stained nucleus, and red E-cadherin-positive huAEC layers on top of PCL:PTMC 50:50.

Furthermore, tissue characterisation was performed by staining the sections against pan-cytokeratin as well as ZO-1 tight junction markers for both membranes, PCL:PTMC 70:30 and 50:50. In the PCL:PTMC 50:50 scaffolds, ZO-1 staining reveals tight junction formation between epithelial cells, as evident from fig. 3.9, while pan-cytokeratin expression highlights a confluent huAEC layer with green fluorescence on the apical side, with nuclei counterstained in blue (DAPI) (fig. 3.9 (C)). Similarly, ZO-1 staining on PCL:PTMC 70:30 (fig. 3.9 (D, E)) indicates consistent tight junctions, and the huAEC layer aligned atop the scaffold by day 12 shows

clear pan-cytokeratin positivity (fig. 3.9 (F)), illustrating well-organised epithelial structures in these triple-culture models.

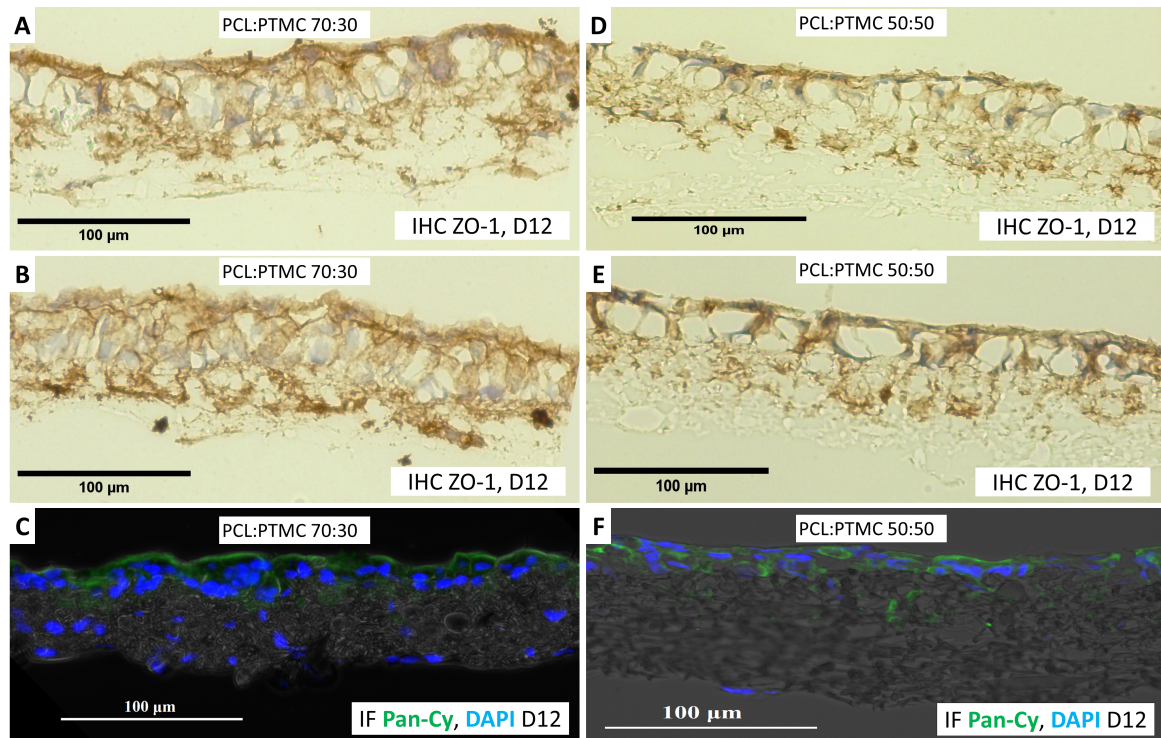


Figure 3.9: ZO-1 and Pan-Cytokeratin Staining in huAEC-LbFb-hEC Co-Cultures on PCL:PTMC 70:30 and PCL:PTMC 50:50 scaffolds [6].

IHC analysis of ZO-1 (A, B, D, E) shows the presence of tight junctions in huAEC-LbFb-hEC models on both 50:50 and 70:30 membrane variants. IF analysis of Pan-cytokeratin (green) and DAPI-stained nuclei (blue) confirms huAEC layer formation (C, F).

3.4.3 PA membrane-based *in vitro* models

PA electrospun membrane models with the co-culture of hEC and huAEC with LbFB were similarly set up using an optimised coating solution. Two types of cell seeding approaches were considered while establishing the co-culture models.

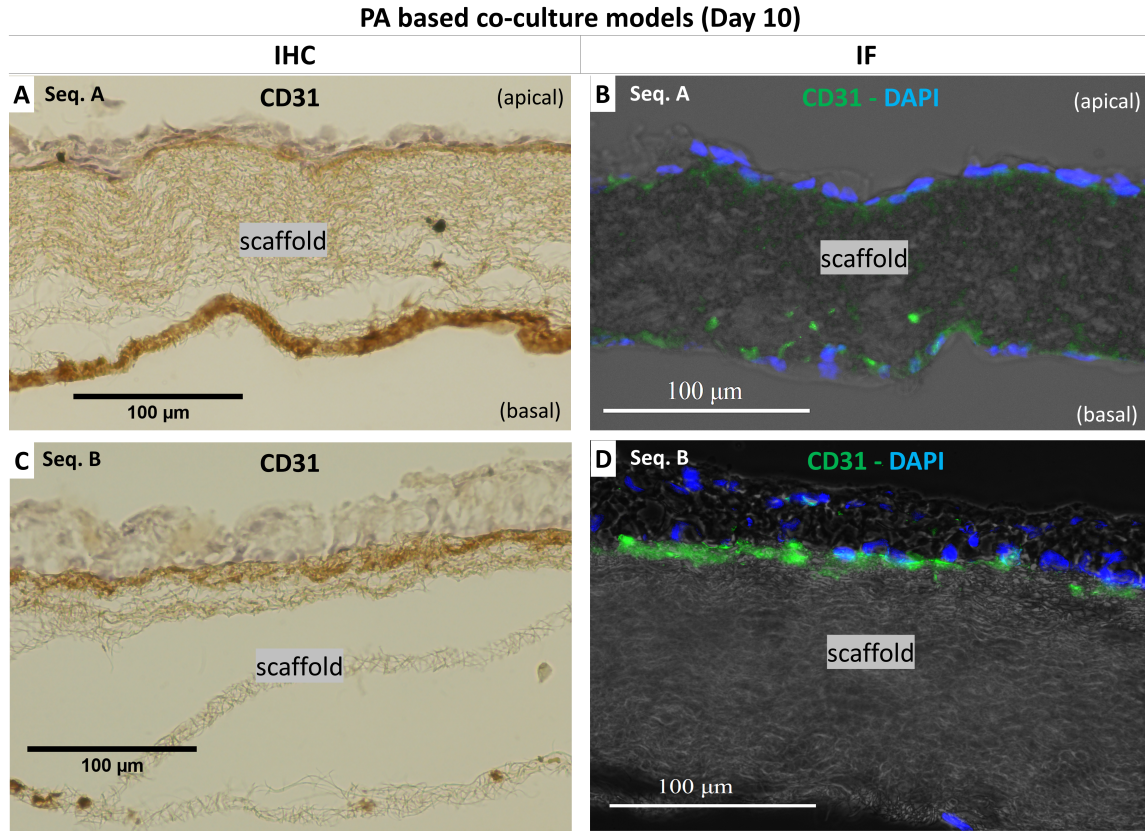


Figure 3.10: Migration behaviour of endothelial cells in PA membrane co-culture models, analysed via CD31 staining, reveals differential migration under two cell seeding sequences.

(A, C) show IHC staining; (B, D) show IF staining. In Sequence A (hEC-huAEC-LbFb), endothelial cells (CD31-positive) remain on the basal side as shown by IHC (A) and fluorescence (B). In Sequence B (huAEC-hEC-LbFb), endothelial cells migrate further inside the membrane, visible via CD31 staining in IHC (C) and IF (D).

Cell seeding scheme (similar to the models described above for PCL and PTMC membrane variants) of first hEC seeding on the basal side then followed by huAEC and LbFB in the wells (during ALI co-culture) is denoted as sequence A. Whereas, sequence B is the altered cell seeding scheme as described in the methods section. Briefly, in sequence B, huAEC cells are first seeded on the apical precoated side of the membrane and then followed by hEC and LbFB (during the start of ALI); for details of exact days please refer to the methods section, fig. 2.1.

CD31 staining was performed on tissue models at day 10 of ALI culture for both sequence A and sequence B. In Sequence A models (fig. 3.10 (A) and (B)), CD31-positive staining for endothelial cells was seen localised on the basal side of the membrane, as confirmed by IHC, which displayed CD31 in a brown stain. The same was confirmed in IF staining, where CD31-positive cells appeared in green fluorescence due to the conjugated secondary antibody. In Sequence B models, however, CD31-positive signals were observed localised directly beneath the apical epithelial layer (fig. 3.10 (C) and (D)). Negative control sections showed no positive signal for CD31, confirming the specificity of the staining.

3.4.4 Analysis of apparent permeability for electrospun membrane-based tissue models

Analysis of change in apparent permeability for models based on PCL:PTMC membrane variants:

In examining the apparent permeability (Papp) across the different membranes, distinct trends emerge, especially when comparing the cell seeding sequences (A and B) across the PCL:PTMC 70:30 and PCL:PTMC 50:50 membrane compositions.

For the PCL:PTMC 70:30 membrane with cell seeding sequence A, the initial Papp at Day 7 is $8.20448 \times 10^{-5} \text{ cm/s}$. At Day 10 Papp decreased to $4.93891 \times 10^{-5} \text{ cm/s}$ and to $4.22204 \times 10^{-5} \text{ cm/s}$ by Day 14. It slightly increased again on day 21 to $5.3442 \times 10^{-5} \text{ cm/s}$, eventually reaching $5.6389 \times 10^{-5} \text{ cm/s}$ by Day 28 and $5.60942 \times 10^{-5} \text{ cm/s}$ on Day 32. In contrast, the PCL:PTMC 70:30 membrane with cell seeding sequence B follows a slightly different trend. Here, the Papp is $6.10039 \times 10^{-5} \text{ cm/s}$ at Day 7, decreasing to $4.83177 \times 10^{-5} \text{ cm/s}$ by Day 10. By Day 14, the Papp rises to $5.99092 \times 10^{-5} \text{ cm/s}$. On Days 21 and 28, the Papp is $5.75839 \times 10^{-5} \text{ cm/s}$ and $4.16746 \times 10^{-5} \text{ cm/s}$, respectively, with another increase to $5.93724 \times 10^{-5} \text{ cm/s}$ on Day 32, hence showing the fluctuating trend.

For the PCL:PTMC 50:50 membrane with cell seeding sequence A, the initial permeability at Day 7 is $7.41145 \times 10^{-5} \text{ cm/s}$. A sharp decrease is observed by Day 10, with a Papp of $4.28332 \times 10^{-5} \text{ cm/s}$. The Papp continues to drop to $3.51918 \times 10^{-5} \text{ cm/s}$ by Day 14. However, this value increases on Day 21 to $5.11444 \times 10^{-5} \text{ cm/s}$, followed by a decrease $2.00641 \times 10^{-5} \text{ cm/s}$ on Day 28, and a further reduction to $1.66316 \times 10^{-5} \text{ cm/s}$ by Day 32.

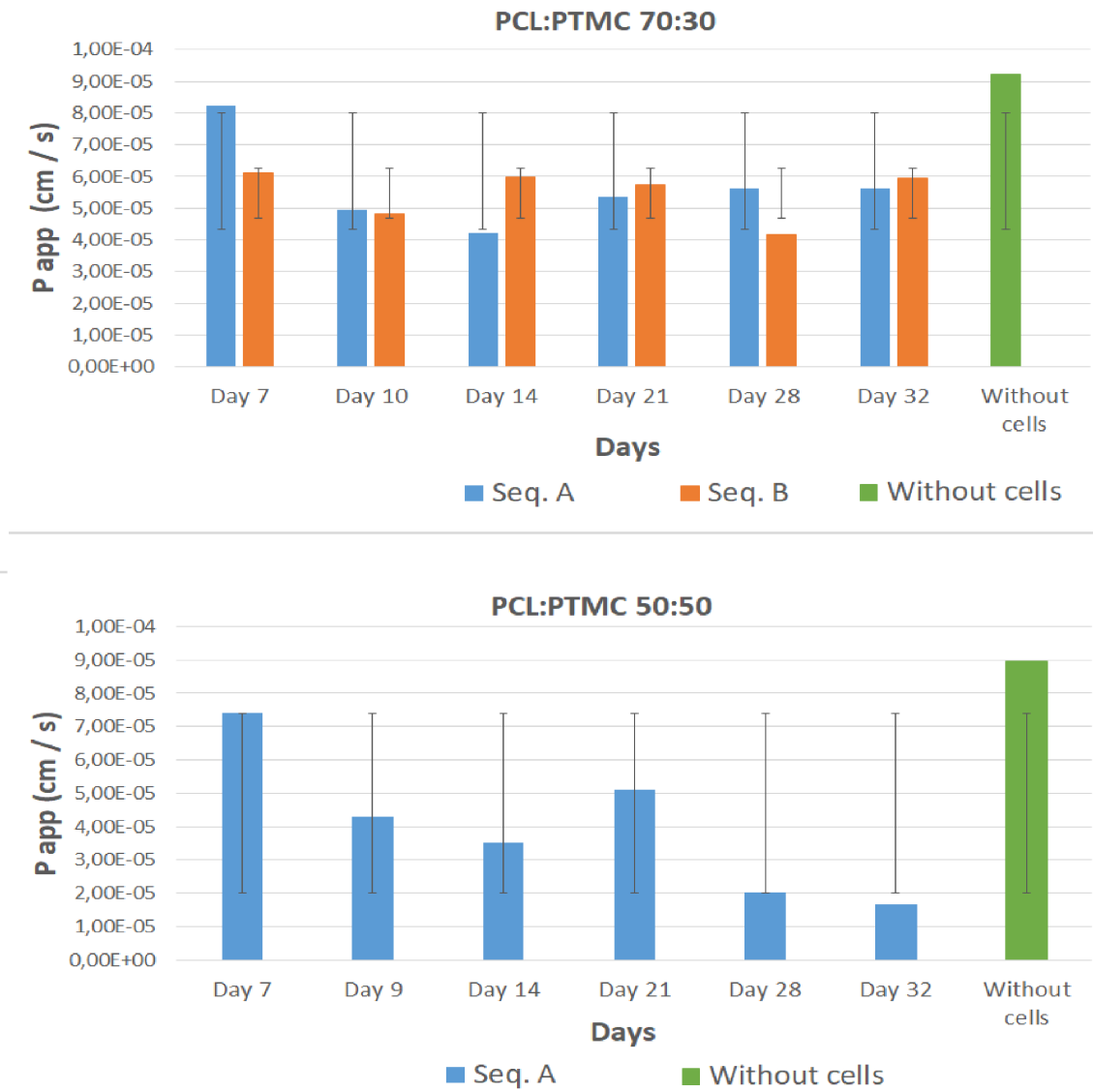


Figure 3.11: Comparison of apparent permeability for electrospun PCL, PTMC membrane-based *in vitro* tissue models

Analysis of change in apparent permeability for models based on PA membrane variants:

The PA membrane shows different permeability dynamics over time. At Day 7, the Papp for sequence A is $6.70257 \times 10^{-5} \text{ cm/s}$, while for sequence B, it is slightly lower at $5.55561 \times 10^{-5} \text{ cm/s}$. However, by Day 10, the Papp decreases to $2.87622 \times 10^{-5} \text{ cm/s}$ for sequence A and slightly increases to $3.4123 \times 10^{-5} \text{ cm/s}$ for sequence B. Interestingly, by Day 14, the permeability for cell seeding sequences A and B both Papp rose slightly to $4.75137 \times 10^{-5} \text{ cm/s}$, and $5.03732 \times 10^{-5} \text{ cm/s}$, respectively, depicting fluctuation.

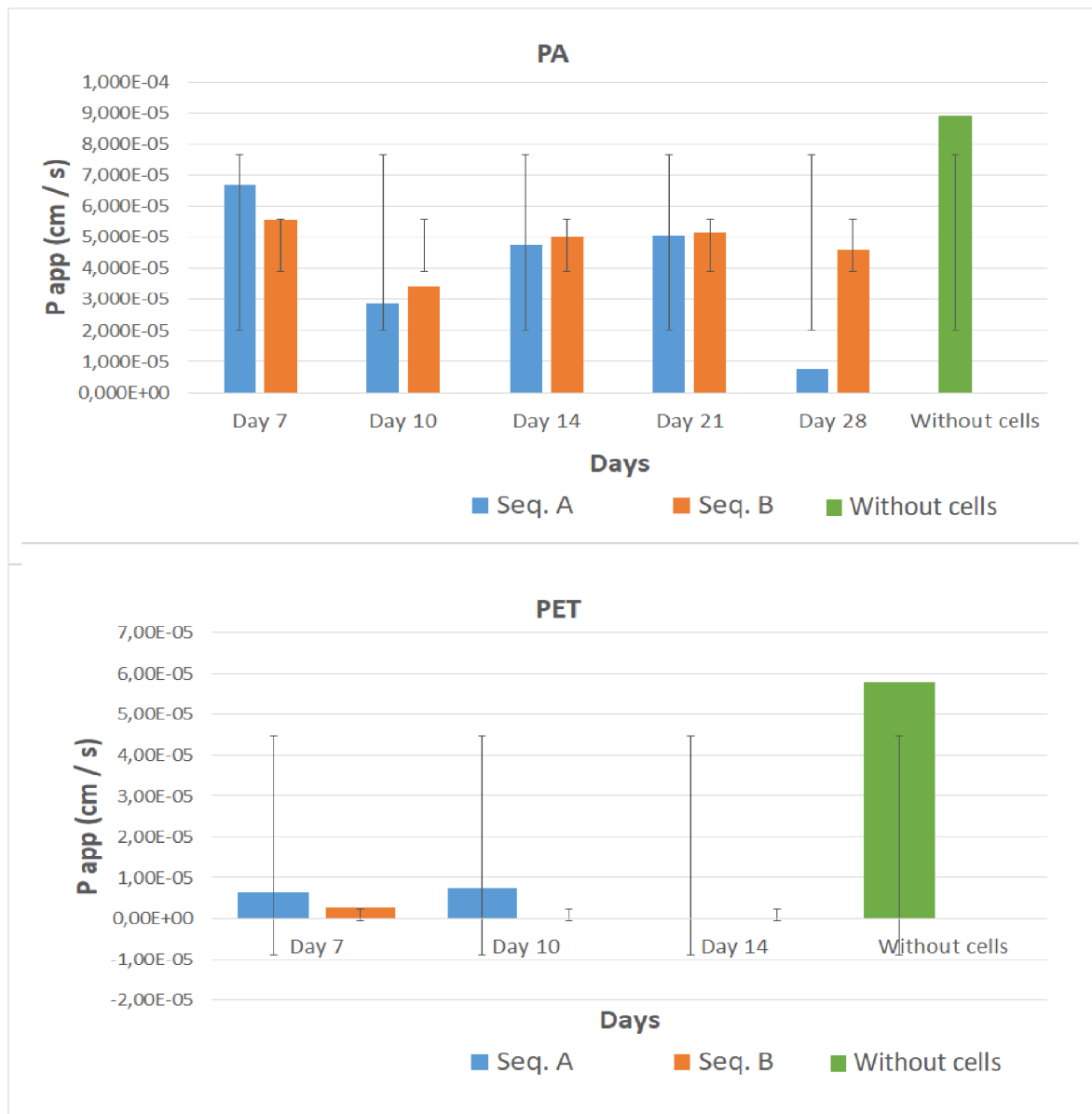


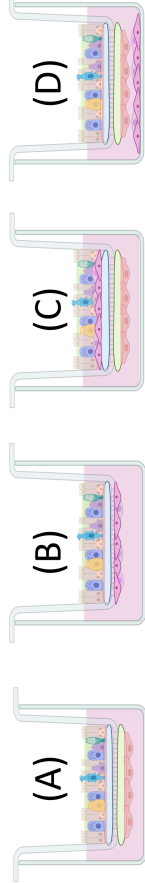
Figure 3.12: Comparison of apparent permeability for electrospun PA membrane and PET-based *in vitro* tissue models

On Day 21, Papp was seen stabilised for both the sequences, with Papp values of $5.06963 \times 10^{-5} \text{ cm/s}$ for sequence A and $5.16558 \times 10^{-5} \text{ cm/s}$ for sequence B. However, by Day 28, sequence A shows a drastic drop to $7.75793 \times 10^{-6} \text{ cm/s}$, while sequence B remains relatively high at $4.58835 \times 10^{-5} \text{ cm/s}$.

For the PET membrane, Papp at day 7 was measured to $6.45 \times 10^{-6} \text{ cm/s}$ for cell seeding sequence A, compared to $2.55 \times 10^{-6} \text{ cm/s}$ for sequence B. On Day 10, the Papp for sequence A showed an increase to $7.54 \times 10^{-6} \text{ cm/s}$. Given the negligible concentration of FITC, the Papp value was not calculated according to the non-linear curve analysis done by software analysis. Hence no values are listed for Day 10 or subsequent days for cell seeding sequence B, so it's unclear if this trend would continue under that condition.

The following figure summarises in a table format all the key findings for synthetic scaffold-based models used to establish co-culture of huAEC with hECs and LbFb.

Material	Coating	Cell types	ZO-1	pan-Cytokeratin	E-cadherin	Vimentin	CD31	Cell-layer (less than 3 layers)	Modulus of elasticity	Thickness (μm)
PET (Mattek*)	huAEC (Apical) + 2% gelatin (basal)	(C) huAEC-LbFb-hEC	+	++	++	++	-	--		
		(B) huAEC-LbFb	-	+	+	+	-	-	2-3 Gpa ⁴¹	22 \pm 3
PET	huAEC (Apical) + 2% gelatin (basal)	(A) huAEC-hEC	-	+	+	-	-	--		
		(D) huAEC-hEC-LbFb	+	++	+	-	++	--		
PCL:PTMC 50:50	huAEC (Apical) + 2% gelatin (basal) huAEC (Apical) + 2% gelatin + VEGF165 + hFN (basal)	(A) huAEC-hEC	-	++	+	-	-	-	0.1745 MPa (Std. dev 0,00995)	80-100
		(D) huAEC-hEC-LbFb	++	++	+	-	++	++		
PCL:PTMC 70:30	huAEC (Apical) + 2% gelatin (basal) huAEC (Apical) + 2% gelatin + VEGF165 + hFN (basal)	(A) huAEC-hEC	-	++	+	-	-	-	0.0911 MPa (Std. dev 0,0461)	60-80
		(D) huAEC-hEC-LbFb	++	++	+	-	++	++		
PA	huAEC (Apical) + 2% gelatin + VEGF165 + hFN (basal)	(D) huAEC-hEC-LbFb	++	++	+		++	++	0.588 MPa (Std. dev 0.0786)	60-80



Epithelium layer

Membrane

Primary fibroblasts

Endothelial layer

huAEC coating

Optimized coating

Figure 3.13: Summarised comparison of tissue models on synthetic scaffold materials: results in triple cultures with native fibroblasts and endothelial-epithelial co-cultures. Figure partially adapted using Biorender.com [6]

3.5 Characterisation of mucus

3.5.1 Visco-elastic behaviour analysis

All measurements were performed using a rheometer with a rotating 50 mm disc. After pipetting approximately 5 - 6 ml of mucus samples, they were carefully sandwiched between two discs, such that no air bubbles were formed in between and a continuous liquid layer could be seen around the rim. Given the non-homogeneity of mucus samples, initially, the samples were homogenised using 2 min of disc rotation at a frequency of 1 rad / sec, such that the particles are homogeneously separated all over the surface area of measurement. Measurements performed at two different temperature settings of room temperature (25 °C) and 37 °C did not show any measurable difference in the obtained values.

Amplitude sweep analysis:

The first step of amplitude sweep analysis, performed for extracting the linear region, was additionally performed for different values of angular frequencies: 1, 5, 10, 50, and 100 rad/sec. Storage modulus G' and loss modulus G'' measured were plotted as a function of strain amplitudes going from 0.1 to 10 % strain. Graph 3.14 (A, B) shows plots for storage modulus (G') and loss modulus (G'') for different angular frequencies.

In the case of storage modulus G' shown in graph 3.14 (A), for lower frequencies 1 and 5 rad/sec, it showed an initially sharp decrease. At lower strain amplitudes (0.0954 % - 0.63 %), G' is higher at lower frequencies (1 rad/s), whereas at high Strain (0.994 % - 9.97 %): G' decreases gradually as strain increases across all frequencies. However, as strain increases, the values tend to converge, particularly for 1 rad/s, 5 rad/s, and 10 rad/s, while 100 rad/s decreases sharply. In conclusion, it was seen that for small strains below 1 % strain the storage modulus was large, thus very elastic and for high strains it becomes a linear elastic material. After 1 %, appearing linear for angular frequencies of 1, 5, 10 rad/sec. From the plot, it can be said that from 2 % and higher strain, the material has almost a constant G' modulus or may be behaving like a linear elastic material.

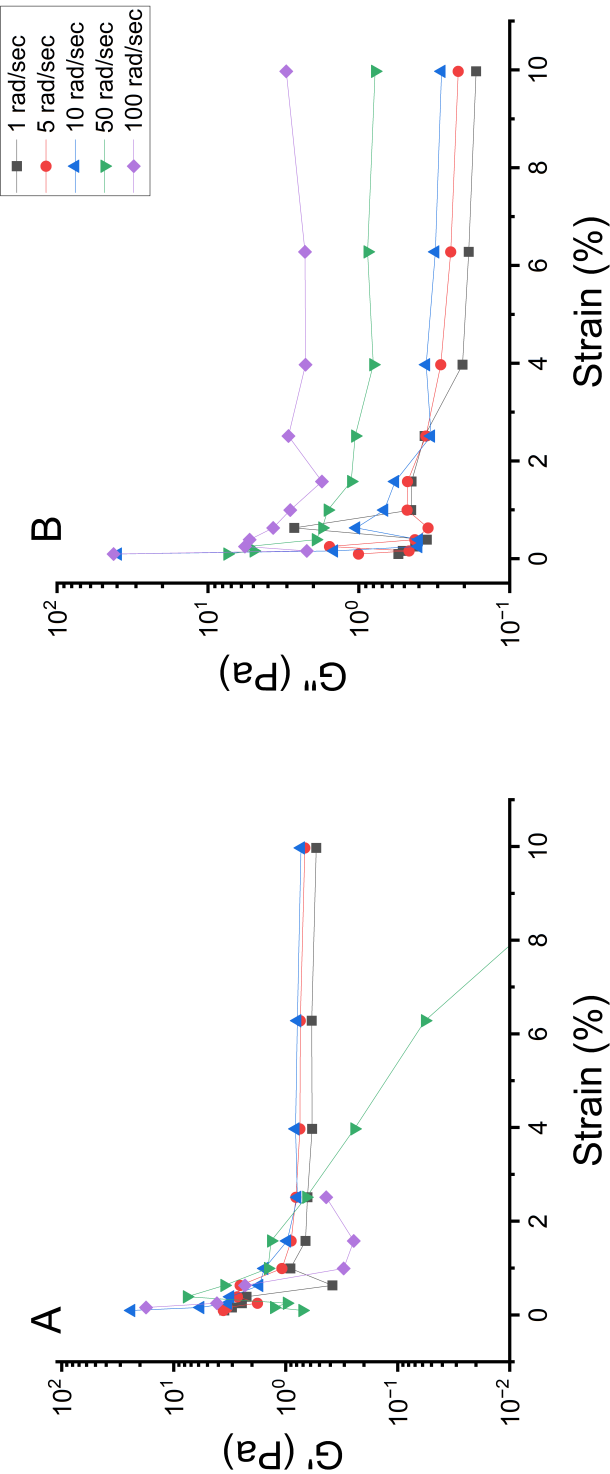


Figure 3.14: Amplitude sweep analysis for mucus sample extracted from 17× SIS-muc Calu-3 - pFb models at 4 weeks using the 500 μ l PBS-method.
(A, B) Amplitude sweep measurements repeated for different angular frequencies of 1, 5, 10, 50, and 100 rad/seconds; data plots for storage and loss modulus G' and G'' .

Loss modulus was plotted in graph 3.14 (B), measured against strain amplitude sweep for different angular frequencies. Across all frequencies in general, G'' decreased with an increase in the strain amplitude values, until a certain point. At lower strains, G'' is generally lower than G' , especially at low frequencies, reinforcing that the material behaves more elastically. Whereas at high strain values, G'' becomes comparable to or even higher than G' at certain frequencies (e.g., 100 rad/s), indicating a shift towards more viscous behaviour as the material is subjected to larger deformations. G'' decreases as strain increases, but the rate of decrease varies by frequency. The higher frequency curves (50 rad/s and 100 rad/s) drop more gradually, stabilising at a higher G'' value beyond 3 % strain. In contrast, the lower frequencies (1 rad/s and 5 rad/s) initially decrease rapidly, then stabilise at a lower G'' value as strain increases.

Frequency sweep analysis:

In the second step of frequency sweep analysis, ideally performed after finding the linear viscoelastic region, it was performed additionally for a range of strain amplitudes of 1, 2, 5, and 10 %, for a frequency sweep from 0.1 to 100 rad/sec. Graph 3.15 (A, B) shows a plot for storage modulus (G') and loss modulus (G'') for different strain amplitudes.

In the graph plot 3.15 (A), G' values are generally higher for lower strains. As strain amplitude is varied from 1 % to 10 %, G' tends to decrease across all frequency ranges, being relatively stable. At higher frequencies more than 10 rad/s, there is a very slight increase in G' value for lower strain amplitudes 1 and 2 %. However, at higher strain levels of 5 and 10 %, G' values tend to decrease and stay relatively low.

Graph plot 3.15 (B) shows loss modulus G'' as functions of frequency and strain amplitude. Similar to G' , G'' also shows higher values for lower strain amplitudes, particularly at 1 and 2 %. But with an increase in frequency, G'' values also increase in general. At higher frequencies, G'' increases initially for all strain levels, particularly for the 1 and 2 % strain amplitudes, but then shows less variation with frequency at lower frequencies for less than 1 rad/s.

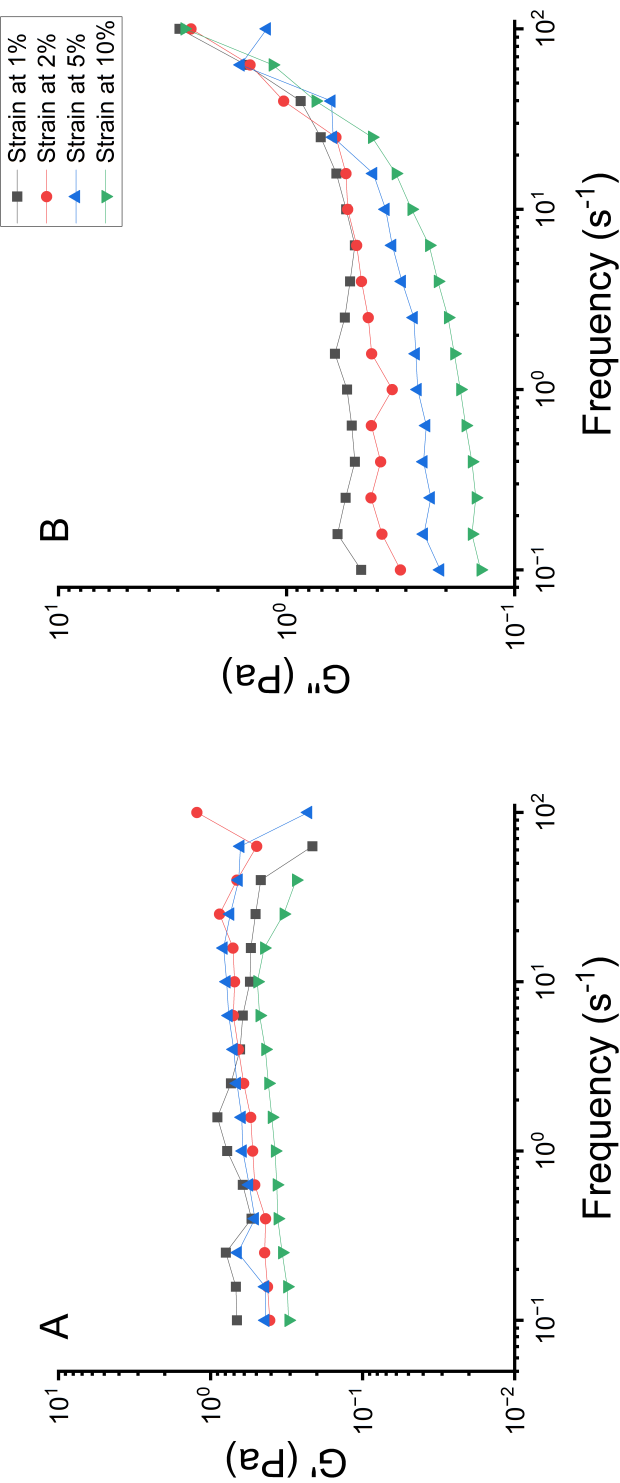


Figure 3.15: Frequency sweep analysis for mucus sample extracted from 17× SIS-muc Calu-3 - pFb models at 4 weeks using the 500 μ l PBS-method.

(A, B) Frequency sweep measurements at different strain amplitudes 1, 2, 5, 10 % data plots for G' and G'' .

Loss angle (δ) was calculated from frequency sweep data for G' and G'' . These δ values in radians were then converted to degrees and plotted against shear rate (frequency) as shown in graph 3.16 (A).

Graph 3.16 (A) depicts the calculated loss angle calculated across shear rates for the different strain amplitudes (1, 2, 5, and 10 %). Here the y-axis denoted the loss angle in degrees going from 0° to 90° . For the lowest strain amplitude and low shear rates of 1 %, the loss angle remained fluctuating between 35° and 45° . As the shear rate increases, the loss angle starts to increase significantly, reaching around 60° . For the highest strain amplitude of 10 %, the loss angle remains around 30° and 35° , lower than that for 1 % strain.

Above graph 3.16 (B) plots calculated dynamic viscosity η' (in Pa s) on the y-axis against shear rate (in s^{-1}) on the x-axis for various strain amplitudes (1, 2, 5, and 10 %). Viscosity and shear rate are presented on logarithmic scales. These values will help to understand the behaviour of mucus for its shear thinning or strain-dependent changes in viscosity value. The graph shows a consistent reduction in viscosity with increasing shear rate across all strain amplitudes, with a noticeable gap between different strain levels. At higher strain amplitudes of 5 and 10 %, calculated η' is consistently lower than observed at lower strains. At low strains of 1 %, viscosity starts relatively high at low shear rates but decreases more gradually than at higher strains of 10 %.

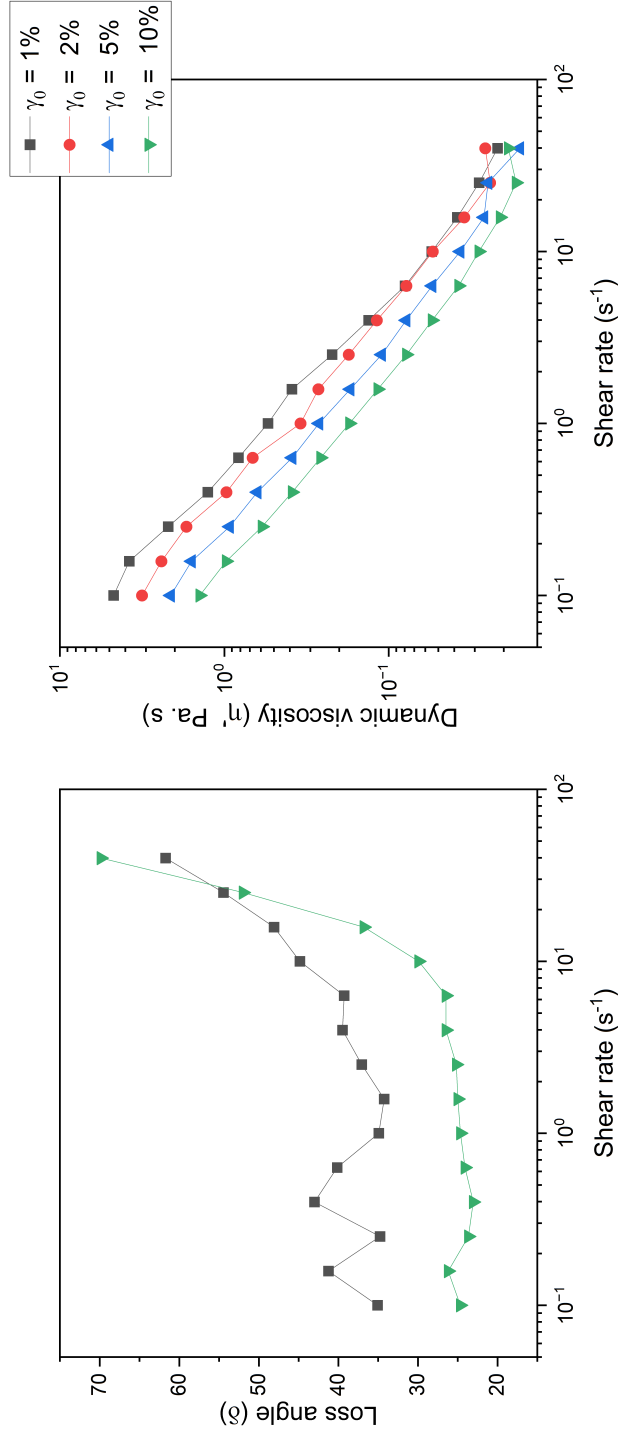


Figure 3.16: Loss angle (δ) and dynamic viscosity η' calculated for mucus sample extracted from 17x SIS-muc Calu-3 - pFb models at 4 weeks using the 500 μl PBS- method.

(A) Loss angle (δ) calculated for high strain of 10 % and 1 % at different shear rates. (B) Dynamic viscosity η' calculated from frequency sweep data measured at strain amplitudes γ_0 at 1, 2, 5, and 10 %. Viscosity and shear rate are presented on logarithmic scales.

3.5.2 Surface tension analysis for extracted mucus samples

Surface tension (ST) measurements of mucus samples were conducted using a tensiometer (Krüss), focusing on addressing challenges posed by gradual sample drying during testing. To maintain consistent humidity, a custom-designed, 3D-printed flat cylindrical vessel was used, containing a salt solution to achieve 100 % humidity. This setup was necessary as mucus drying impacts the accuracy of ST readings over time.

Two distinct procedures were applied based on the sample source and preparation. For mucus samples measured at weekly intervals directly on the *in vitro* tissue models (the models mounted on metal inserts two metal cylinders that secure the tissue in place, for air-liquid interface (ALI) cultures) as explained in the fig. 3.17 (D). Mucus gets generated on the apical side of these cultures, and then the entire mount was placed directly in the PTFE sample holder for ST assessment. The D. Noüy ring method was employed, with measurements performed by using a small ring electrode and a prewetting time of 5 seconds. This involved cyclic up-and-down motion of the ring through the sample to create a thin film, allowing repetitive measurements until achieving a low standard deviation. The software calculated ST values based on stabilised measurements, capturing the average ST values once variability diminished.

For other measurements, including lung lavage samples from pre-surgical tracheal cleaning, mucus was extracted from the tissue models using phosphate-buffered saline (PBS) before measurement. These extracted samples were spread on a PTFE holder with a 15 mm diameter, and a similar cyclic measurement method was applied as explained in fig. 3.17 (A - C). Initial static force measurements were also performed on these samples to determine lamella height and force exerted by the film, refining the ST measurement parameters for each sample.

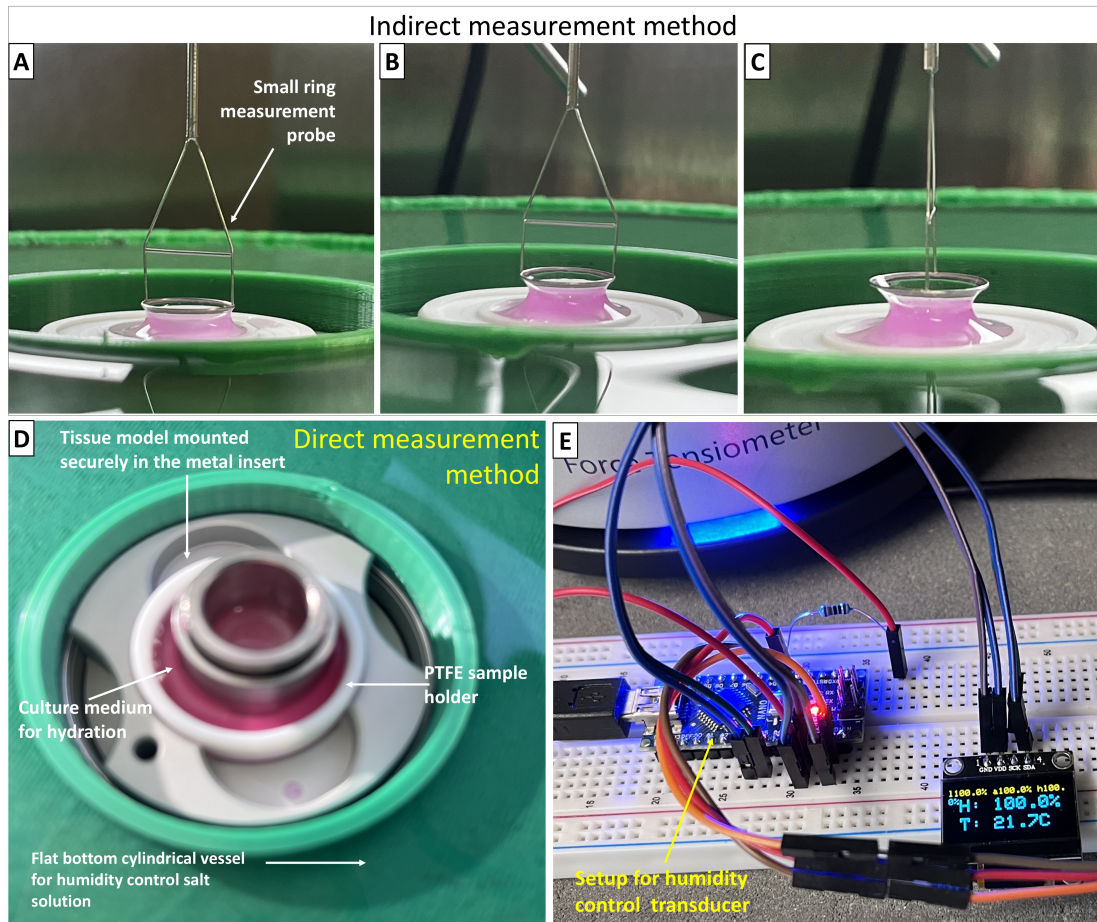


Figure 3.17: Surface tension measurement method using Force tensiometer.

(A- C) shows the indirect measurement setup with mucus samples of $200\ \mu\text{l}$ placed on the PTFE holder. Measurements for ST are done using a small ring with Noüy ring method in repetition cycles. (D) shows the setup for direct measurement using mounted *in vitro* airway tissue models with expressed mucus. (E) shows the setup used for measuring the controlled humidity using a transducer placed inside the measurement unit.

Fig. 3.18 shows the steps involved in analysing ST values for each measurement. The software-calculated data exhibiting consistent, repetitive cycles (highlighted in the red square in fig. 3.18 (A) was used to determine the average ST value. For statistical reasons, only six values from these repetitive cycles were selected to calculate the average of surface tension values each from week 1 to 4 as shown in the fig. 3.18 (B). This result was then compared to both the automatically calculated ST values provided by the software and the average derived from the entire dataset of consistent, repetitive cycles. The final summary of ST values based on repetitive measurement cycles versus software-calculated values illustrates this pattern fig. 3.18 (B).

Table shown in fig. 3.18 (B) shows ST values from *in vitro* mucus samples measured at different weekly intervals. The surface tension measured for mucus samples from the *in vitro* models at weekly intervals of weeks 1, 2, 3, and 4 showed some fluctuation in their average ST values (fig. 3.19 (A)). For the optimised calculation method considering only repetition cycles as highlighted in fig. 3.18 (A), values of ST fluctuated in a decreasing manner, going from 35 to 30 mN/m. Whereas the software calculated ST values suggested an increase in the ST from week 1 to week 4 mucus models.

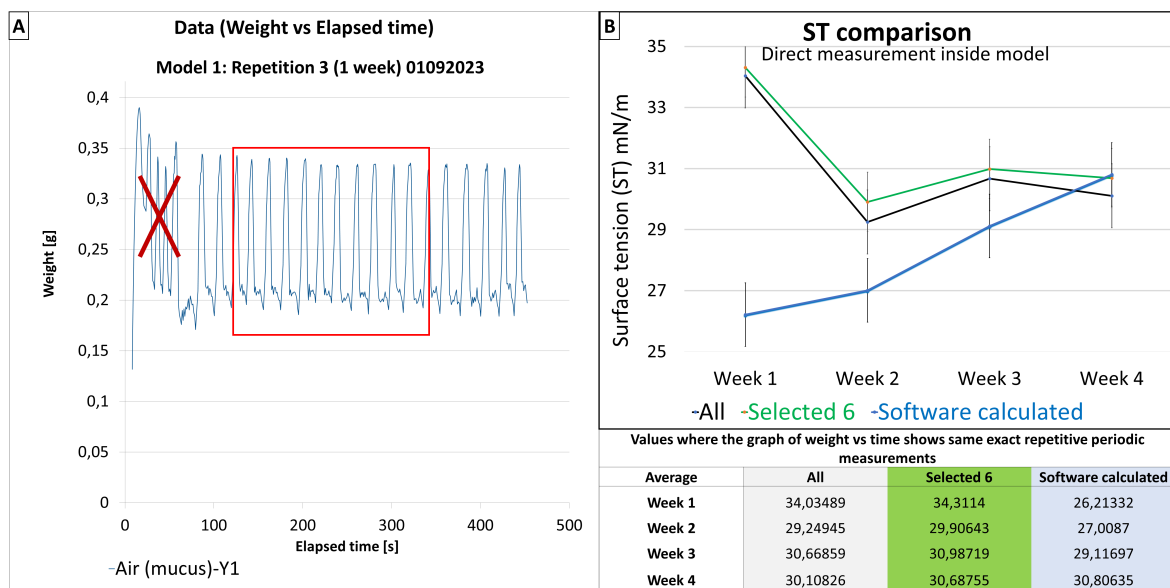


Figure 3.18: ST value analysis strategy represents data selection of only repeated cyclic measurements.

(A) Shows the data plot for the measured force exerted by the mucus on the ring vs. time, where only the highlighted repetition values are generated for surface tension is then considered for the further average calculation of the surface tension. (B) Graphical representation of changes in the ST values for mucus extracted from models stopped at week 1 of ALI, to 4 weeks ALI

Lung Lavage and PBS-extracted Mucus Samples: The tables below summarise the collected data, detailing ST values, standard deviations, and lamella heights across various sample types. Average ST values were generally lower than directly measured samples, with lung lavage values stabilising around 44.05–44.11 mN/m and similar lamella heights.

This data supports the effectiveness of using repeated cyclic measurements to enhance reliability in ST readings, particularly in distinguishing values from *in vitro* and *in vivo* (lung lavage) sources.

Indirect measurement on extracted mucus

Surface tension: Indirect measurement on extracted mucus					
Sample	Prewetting time (s)	Holder diameter (mm)	ST mN/m	Standard deviation	lamella height (mm)
S1	5	15	50,38705	0,104785	1,714
S1	5	15	50,892871	0,08518	1,611
S2	5	15	41,255411	0,09375	1,26
S2	5	15	42,496406	0,060852	1,458
S3	5	15	47,763771	0,094421	1,51
S3	5	15	44,990293	0,107614	1,575
S3	5	15	45,033535	0,094882	1,442
lung lavage	5	15	44,111367	0,137536	1,612
lung lavage	5	15	44,051508	0,085084	1,672

S1- Mucus ex. 400µl PBS-

S3- Mucus ex. 1ml PBS- (4Wk 15x models)

S2- Mucus ex. 500µl PBS- (17x samples)

Lung lavage – obtained from pre-surgery tracheal cleaning

Figure 3.19: Measured surface tension values using indirect method for mucus samples and lung lavage

Comparison of ST values from mucus extracted from 4 week tissue models but using different extraction strategies of varying volumes of PBS- as well as lung lavage sample obtained from patient from University Hospital Magdeburg with consent in preoperative process

4

Publications

1. Wiese-Rischke, C., **Murkar, R. S.**, Walles, H. (2021). Biological Models of the Lower Human Airways-Challenges and Special Requirements of Human 3D Barrier Models for Biomedical Research. *Pharmaceutics*, 13(12), 2115. <https://doi.org/10.3390/pharmaceutics13122115>

Abstract

In our review, we want to summarize the current status of the development of airway models and their application in biomedical research. We start with the very well characterized models composed of cell lines and end with the use of organoids. An important aspect is the function of the mucus as a component of the barrier, especially for infection research. Finally, we will explain the need for a nondestructive characterization of the barrier models using TEER measurements and live cell imaging. Here, organ-on-a-chip technology offers a great opportunity for the culture of complex airway models.

-
2. **Murkar, R.;** von Heckel, C.; Walles, H.; Moch, T.B.; Arens, C.; Davaris, N.; Weber, A.; Zuschmitter, W.; Baumann, S.; Reinhardt, J.; et al. Establishment of a Human Immunocompetent 3D Tissue Model to Enable the Long-Term Examination of Biofilm–Tissue Interactions. *Bioengineering* 2024, 11, 187. <https://doi.org/10.3390/bioengineering11020187>

Abstract

Different studies suggest an impact of biofilms on carcinogenic lesion formation in varying human tissues. However, the mechanisms of cancer formation are difficult to examine *in vivo* as well as *in vitro*. Cell culture approaches, in most cases, are unable to keep a bacterial steady state without any overgrowth. In our approach, we aimed to develop an immunocompetent 3D tissue model which can mitigate bacterial outgrowth. We established a three-dimensional (3D) co-culture of human primary fibroblasts with pre-differentiated THP-1-derived macrophages on an SIS-muc scaffold which was derived by decellularisation of a porcine intestine. After establishment, we exposed the tissue models to define the biofilms of the *Pseudomonas spec.* and *Staphylococcus spec.* cultivated on implant mesh material. After 3 days of incubation, the cell culture medium in models with M0 and M2 pre-differentiated macrophages presented a noticeable turbidity, while models with M1 macrophages presented no noticeable bacterial growth. These results were validated by optical density measurements and a streak test. Immunohistology and immunofluorescent staining of the tissue presented a positive impact of the M1 macrophages on the structural integrity of the tissue model. Furthermore, multiplex ELISA highlighted the increased release of inflammatory cytokines for all the three model types, suggesting the immunocompetence of the developed model. Overall, in this proof-of-principle study, we were able to mitigate bacterial overgrowth and prepared a first step for the development of more complex 3D tissue models to understand the impact of biofilms on carcinogenic lesion formation.

-
3. Spoddig, V. J.; Walles, T.; Walles, H.; **Murkar, R.** Entwicklung eines *in vitro* 3D – Modells zur Testung von Gewebereaktion auf Implantatabrieb (V-151). Kongress: 33. Jahrestagung der Deutschen Gesellschaft für Thoraxchirurgie Datum/Ort: 18 . – 20 . September 2024 , Magdeburg. Brustwandchirurgie (S93), Thieme ZBC 2024 ; 2024 : S85 – S131. DOI 10.1055/s-0044-1788103, <https://www.thieme-connect.de/products/ejournals/conferencepdf/132054/10.1055/s-00000104.pdf>
 4. **Murkar, R.**; Wiese-Rischke, C.; Weigel, T.; Kopp, S.; and Walles, H.;. Developing human upper, lower, and deep lung airway models: combining different scaffolds and developing complex co-cultures. *Journal of Tissue Engineering*.
 5. Spoddig, V. J.; Walles, H.; **Murkar, R.**. Hydrogel based 3D invitro foreign body reaction assay to test implant abrasion reaction to ceramic, steel , titanium implant particles materials. **Ongoing Publication**
 6. **Murkar, R.**; Ohl; Claus,D.; Walles, H.;. Influence of physical surface tension and rheological properties on thin film formation using mucus from invitro lung human tissue models. **in-preparation**

5

Discussion

Various systems have been researched and developed with the focus on 3D *in vitro* microenvironment with the aim to replace *in vivo* animal models, which lack relevant similarity and data compared to human biology [43, 85, 86]. Tissue-engineered systems have advanced, going from conventional 2D cell-based systems organoid culture to the more complex lab-on-chip / organ-on-chip methods. Among other 3D organ-specific biomimetic *in vitro* test systems, the human respiratory system is crucial to be modelled in 3D given its dynamic tissue architecture and cell type differentiation as one progresses from the upper airway region towards the minute alveolar regions [15, 19].

The development of tissue models is vital in various applications, including tumour study, bacterial infections, or viral mediation studies. An illustrative example is the investigation of how the viral super spread of SARS-CoV-2 via minute alveoli acts in context with the formation of aerosol-packed viral particles that transport the viral load. Understanding these processes is essential for uncovering how the virus spreads extensively [19]. In order to model lung area-specific 3D *in vitro* tissue models, this study delved deeper into crucial characteristics of airway area-specific ECM scaffolds and selection of cellular components, along with their functional characterisation for upper, lower, and alveolar airways.

Many studies have stressed the importance of three major components in Tissue Engineering namely, precisely engineered synthesis/selection of appropriate scaffold biomaterial niche and tissue-specific cellular components, along with the optimisation of the microenvironment for proper cellular differentiation and tissue growth [14, 79, 80]. Fabricating native ECM-like scaffolds is deemed necessary for enhancing cellular attachment, promoting cell growth and differentiation of primary human cells, and fostering physiological cell behaviour [87].

5.1 3D *in vitro* airway tissue models

Given the heterogeneity of airway epithelium with region-specific distinct specialised cells provides difficulties in *in vitro* modelling systems. The differentiation and pseudostratification of epithelium is influenced by the basal 3D microenvironment forming the extracellular matrix. This complex microenvironment required to provide tissue- or region-specific proteins embedded in collagenous polymer formations for cellular adhesion plays a vital role in ECM cell receptor signalling. Additionally, it must also include essential tissue-specific airway area-specific cell types, including sub-epithelial fibroblasts, endothelial cells, immune cells, and smooth muscle cells, essential for cell-cell communication [12].

2D gold standard ALI models exhibit limitations firstly regarding lack of cell-cell interactions of epithelium with non-epithelial cell subtypes [88] and secondly regarding the ECM scaffold like universally used PET or PC membranes with higher Young's modulus compared to native *in vivo* tissue counterpart. 2D planar microfluidic models also provide the possibility for developing air-lift-based co-cultures, however lack the essential biomechanical ECM resemblance to native tissue beyond additional collagen coatings of these stiff polymer membrane surfaces only aiding in cellular attachment [89–92]. In conclusion, the current design lack a biomechanical ECM environment may limit cell attachment and alter cell-matrix interaction (cellular behaviour).

A representative model should support well-differentiated human airway models at ALI and incorporate a 3D microenvironment with essential physiological cell-cell, ECM-cell, and biomechanical interactions. Among other crucial membrane properties like the presence of surface adhesion proteins, porosity, the tenability of pore densities, thickness, and elastic moduli (organ / native tissue-specific), in this study, we specifically underline the relevance of membrane mechanical properties like thickness, stiffness, and flexibility of the ECM that vary as the airway deepens, along with the cellular architecture and differentiation. It is known that (summarised in fig. 1), throughout the human respiratory tract, the ECM thickness is reduced from the upper airways to the deep lung alveoli. Hence, ECM thickness modification may be crucial to account for distinct structural and functional characteristics across different airway regions while developing region-specific airway models. It is approximated that the ECM is thicker with a thickness of approx. (50 – 100 μm) [5, 92, 93] in the upper airway region while it's reduced in thickness (10 - 50 μm) [5, 94] in the lower airway region, and ultra-thin (0.2 to 10 μm) [5, 95] in the alveolar airway. We accordingly selected different categories of scaffold material membranes for three main airway locations: upper/lower and alveolar.

5.1.1 Upper airway region:

In a recent study, a novel approach was published where native-lung-ECM-solubilised collagen hydrogel was used to develop airway tissue models, which does provide well-differentiated ALI epithelium and maintain barrier function [19].

In addition to the limitations, such as donor variability in ECM composition, lack of basolateral liquid flow and apical airflow, the thinness of the formed hydrogel ECM needs further optimisation. Our experimental models with the biologically derived SIS-Muc scaffold (200 μm thickness), are presented to be highly appropriate for modelling the upper airway region. Many applications of SIS-Muc include engineering liver-like tissue (BioCaM) using the advantage of the presence of capillarized matrix provided by SIS-Muc [81]. Having a collagen–elastin network provided the architecture for endothelial cells seeding to form capillary-like structures. Many applications like BioVaM, etc. followed [96].

Our SIS-Muc based models of co-culture of Calu-3 and primary human fibroblasts were able to produce increasing functional mucus over the period of 4 weeks, depicting successful cellular differentiation. The tissue models also developed tissue resistance with the presence of tight junctions. In addition, fibroblasts actively migrated into the scaffold fibres, which was only possible in the case of SIS-Muc scaffold and not possible in synthetic scaffold variants like PET. The Calu-3 cells initially formed a monolayer and gradually multilayered until 4 weeks of ALI while developing differentiated epithelium layers. Similarly, when cultured on a 33 μm thinner PET membrane, it also reproduced similar results with respect to functionally increasing mucus formation and tight junction expression.

SIS-Muc is equipped with the necessary mucosal architecture along with the fibrous network made of collagen and elastin fibres which make up the majority of the physiological ECM [81]. We believe that in our case, SIS-Muc shows exceptional behaviour when modelling upper airway systems using Calu-3 cell line along with fibroblasts in co-culture. SIS-muc provides biologically orientated ECM structures and a thickness in the range of 200 μm , which aligns with the requirements for the upper human airway, as demonstrated in fig. 1.1 (A). The characteristic multilayered epithelium (3–4 layers) in the upper airway, shown in fig. 1.1 (A), matches our findings of 2–3 epithelial layers, as summarised in Table 6. Additionally, the mucus layer in our model increased from $30 \pm 5 \mu m$ after 1 week to $505 \pm 5 \mu m$ by 4 weeks in ALI culture, mimicking the typical mucus thickness observed in the upper airway (30 – 100 μm) [97], making this a desired outcome for airway tissue models alongside the formation of ZO-1 positive tight junctions.

While PET scaffold models showed tight junction formation (ZO-1) and mucus expression fig. 3.13, they lacked the prominent epithelial multilayering and adequate mucus thickness found in SIS-muc models, which is crucial for mimicking both upper airway mucus properties and lower airway requirements, where mucus typically thins out to 10–30 μm in bronchioles [98].

5.1.2 Lower Airway region:

The lower airway region depicts a thinner ECM and, in concert with a thin mucus lining, is required to have greater flexibility and responsiveness to changes in airflow and ventilation demands. However, ECM thickness here is not required to be as thin as in alveoli to provide structural support for dynamic changes in airway diameter and resistance during breathing (refer fig. 1.1 (B)). Fibroblasts are not as abundantly present in the ECM as in the tracheal ECM but also play a role in airway tone and regulation [99, 100]. Scarce occurrence of the goblet epithelial cell types contributes towards a thinner mucus layer on top of the epithelium lining, while occurrences of club cells increase as one descends to the respiratory bronchiole.

In our experiments, thinner ECM, thinner mucus layer, and single-layered epithelium were crucial aspects we considered while developing a tissue model representing the lower airway [101–103]. We proposed to use commercially available PET membrane thincerts® given their thinness of approximately 33 μm . They have a characteristically stiff structure with controlled pore size and are available in different pore densities [29]. Porous membranes and pore size ensure exchange between the compartments but seem not to have a major influence on specific cellular functions. Moreover, PET thincerts® are also known to allow extensive co-cultivation of cells on both sides of the membrane, allowing direct cell-cell interactions. PET membrane also proved suitable for modelling the upper airway as well as lower bronchiolar structures of the lung, given the comparative lower thickness of approx. 10 μm .

Lower respiratory tract models are widely established using the A549 cell line co-cultured with fibroblasts. A549 cells, resembling alveolar type II pneumocytes, show enhanced cell-cell and cell-matrix interactions when co-cultured with fibroblasts, though they exhibit different characteristics compared to Calu-3 bronchial epithelial cells [104–107]. When cultured on a hydrogel-based matrix or collagenous biological scaffold-like SIS-Muc, the models were able to express comparable tight junction proteins to that of Calu-3 [49, 108], but when 2D cultured on plastic surfaces, there was a significant reduction in tight junction proteins, indicating reduced epithelial barrier integrity compared to Calu-3 cells [104, 107]. Our models on PET membrane

with Calu-3 cells (although derived from bronchial epithelium) were used to set up co-culture with fibroblasts (on the basal side) and revealed similar results as seen with SIS-Muc as a scaffold. A noticeable decreased mucus layer of $41 \pm 5 \mu m$ at 1 week of ALI to $128 \pm 5 \mu m$ after 4 weeks of ALI was observed. Although PET provides the desired thin ECM for the lower airway ($33 \mu m$) within the range of 10 - 60 μm , the mucus thickness is still not ideal as required for lower airway tissue models (10 - 30 μm in bronchioles [98]). The results from FITC dextran assay showed a dramatic reduction in the apparent permeability of these models right after 11 days underscoring the formation of a tight junction barrier. Co-culture of A549 and primary fibroblasts showed multilayered epithelium (> 3 layers, as summarised in fig. 3.13) formation at week 3 both in the case of SIS-Muc as well as PET-based models. The measured apparent permeability was approximately $8.85 \times 10^{-5} cm/s$ at day 9 of ALI culture, revealing its failure to form an intact, tight junction barrier. It is essential to have multilayering of the epithelial layer in bronchi and bronchioles to maintain a proper barrier function and facilitate mucociliary clearance. For instance, models of human bronchial epithelial cells cultured in 3D environments demonstrate that a pseudostratified layer with multiple cell types is necessary for mimicking *in vivo* function [109].

For a valid model for the lower airway, as shown in fig. 1 (B), typically, in the bronchioles, fewer layers are present compared to the trachea and larger bronchi, but a minimum of 2-3 layers is required to replicate the mucosal structure and ensure epithelial integrity [110]. Hence, despite the widespread use of co-culture of the A549 epithelial cell line with primary human fibroblasts, in our studies, a co-culture on PET membrane was unfortunately unable to form tight junctions (negative ZO-1) and hence no barrier formation was achieved. Better culture control is also necessary to achieve the desired 2 – 3 max multilayered epithelium.

The described standardised models were able to produce a differentiated epithelium layer and presented distinct functional mucus formation. In addition, cancer cell lines like Calu-3 and A549 maintain consistent properties across passages, presenting the advantage of experimental reproducibility and consistency. However, they may lack the ability to produce realistic biomimetic lung tissue models.

5.1.3 Deep lung alveolar region:

Alveolar epithelium shares an ultra-thin basement membrane (approx. 0.2 - 0.62 μm) with the endothelial cell layer from the surrounding blood capillaries via the septum, which is crucial for the air-blood barrier [7]. The previously thicker ECM is remodelled by fibroblasts to form a thin fibrous network through which blood

capillaries pass. Hence, to develop a 3D alveolar tissue model, we focused on two main aspects: synthesis of ultrathin basement membrane, having the possibility for lower Young's modulus of elasticity in the range of kPa, and secondly, optimisations for the establishment of co-culture of endothelial cells with alveolar epithelial cells [101, 102, 111, 112].

Commercially available Epi-AlveolarTM models from Mattek GmbH depicted co-culture alveolar primary epithelial cells and endothelial cells, with the inclusion of fibroblasts on the PET membrane. Here, epithelial cells were grown on top of the fibroblast layer, and the endothelial cells were seeded on the basal side in contact with the medium. The possible drawback of such cellular layers can be unavoidable multi-layering of fibroblasts and the epithelial cell layer, as well as higher elastic modulus of the PET membrane (fig. 3.5). Given the high elastic modulus of PET in the range of 2 - 3 GPa, which is more or less similar to that of cancellous bone tissue, it is much higher than required for modelling lung tissue [92, 113]. Meanwhile, the pores can become a disadvantage when co-cultured with endothelial cells because endothelial cells can also find ways to migrate through the pores to the other side of the membrane, increasing unwanted cell-cell crosstalk. Hence, it may not be able to specifically mimic physiological conditions as in alveoli.

For alveolar models, it is not only crucial to set up a co-culture system to have epithelial and endothelial crosstalk but also includes the fibroblasts. Our models with electrospun membranes were able to demonstrate direct co-culture of endothelial cells (on the basal side membrane) and epithelial cells (apical), along with the influence of native lung fibroblasts on the cellular alignment (fig. 3.6, comparing (B) & (C), (G) & (H)). The porous membranes not only provided the advantage of aligned endothelial migration and direct contact with the epithelial layer but also the added advantage of relatively lower Young's modulus of 0.0911 MPa (PCL:PTMC 70:30) and 0.1795 MPa (PCL:PTMC 50:50) than to that of flat-PET.

Upcoming *in vitro* models also stress the advantage of building stem cell-based organoid cultures using induced pluripotent stem cells (iPSCs), which can serve as better human lung models than cancer cell lines [114]. However, these organoids have limitations, such as the absence of certain epithelial phenotypes. Additional inclusion of macrophages or fibroblasts along with co-culture of iPSC-derived lung cell models is crucial for differentiation, but this also increases the timeline for attaining the required differentiation into alveolar-specific lung cell types [115, 116]. It is known that both proximal and distal airway components play a role in viral infectivity and the host immune response. Previous models lacked diverse cell types and did not incorporate both proximal and distal airway epithelia in a single construct [114]. Novel 3D organoids created using adult lung stem cells were compared to

models using primary human airway epithelial cells and induced pluripotent stem cells (hiPSCs) in one of the research studies. These organoids expressed various lung cell markers and demonstrated multicellularity. The same models were also cultured either submerged or with an air-liquid interface (ALI) and assessed for SARS-CoV-2 infection and gene expression. The submerged models showed a weak barrier, while the ALI models formed a more effective epithelial barrier but showed decreased alveolar signatures. However, the models have limitations, such as the undefined composition of the culture media, questioning the reproducibility and standardisation measures, and the absence of immune cells and other components.

Influence of optimised coating solutions in in-vitro tissue models

Besides cell-cell interactions, the impact of the niche on cellular behaviour is considered important while designing precision-engineered tissue systems. The novel precision-engineered niche approach addressed strategic manipulation of the niche elements to modulate specific stem cell outcomes, whether for maintaining stemness or promoting lineage-specific differentiation, is a promising approach [14]. We formulated a coating solution, including the essential ECM proteins such as fibronectin, VEGF-165, and collagen in gelatin. With modulated concentrations, we observed enhanced cellular attachment and co-culture formations over the membrane models. These components enhance stem cell signalling, self-renewal, and differentiation while providing structural support and biochemical cues crucial for cellular maintenance [15]. Additionally, mechanical forces and physical properties of the niche further influence stem cell behaviour [14]. This approach has been effectively used in humanised, vascularised 3D bone marrow niches, which support the expansion of haematopoietic stem and progenitor cells (HSPCs) by mimicking the *in vivo* environment [117, 118]. However, challenges remain, including the complexity, cost, and potential immune responses, which may limit clinical applications [21]. Different *in vitro* alternatives expanded towards the 3D co-culture systems can now provide improved possibilities of mimicking the cell-cell as well as cell-extracellular matrix interactions using the generation of co-cultures and microphysiological models built on biological as well as polymeric porous platforms [86]. We have explored a range of niches matched to specific airway regions based on the requirements of the ECM and selected cellular components for developing co-culture tissue systems. We studied different mechanical properties and employed coating strategies for the implementation of synthetic PET membranes for developing the co-culture of endothelial and epithelial cells. Gelatin coating for endothelial cells and specialised huAEC coating for epithelial cells can prove useful in this context to help establish the co-culture models, but the thickness, stiffness, and higher modulus

of elasticity (in the GPa range) remain of concern. PET membrane pore size of 0.4 μm was observed to be optimal for endothelial cell culture to avoid migration of endothelial cells through the pores towards the apical side of the culture consisting of the epithelial layer.

A recent study demonstrated the development of an *in vitro* airway epithelial-endothelial cell culture model using a scaffold synthesised out of flexible porous PTMC membrane based on Calu-3 airway epithelial cells and lung microvascular endothelial cells [29]. PCL and PTMC polymeric materials have recently gained interest given their tunability and control over mechanical properties depending on the molecular weight modulations. Both polymers are known to be non-cytotoxic and provide excellent cell adhesion properties. Especially PTMC is known to be able to adsorb specific cell culture components to enhance cell adhesion. PTMC is known to be highly biodegradable and does not produce any toxic substance, whereas PCL has low biodegradability, and given the moderate stiffness characteristics, it has been applied in skin as well as bone Tissue Engineering applications. PTMC-based structures are known to have good mechanical properties, including relatively low elastic moduli than PET, lower water uptake, and maintaining the structure's integrity even when wet against PCL membranes, which are highly hydrophilic in nature. Electrospinning such polymer solutions delivers freedom to adjust these properties for fabricating membranes using two different proportions of the mixture from PCL and PTMC namely 70:30 and 50:50. PCL:PTMC 50:50 was seen to have more homogenous fibrous strands and dense fibrous networks when compared to that of the 70:30 mix. Given the highly hydrophilic nature of pure PCL membrane, unstable fibre architecture, and compromised suitability towards various histochemical analysis steps (xylol solubility), it was seen as unsuitable for the establishment of the co-culture; hence, data are not shown. Coatings of the membrane with the mixture of VEGF-165 at 0.5 ng/ml + human plasma fibronectin protein + collagen 1 + BSA in 2 % gelatin revealed better cellular adhesion to the membrane. The co-culture medium, when optimised to a 2:1 concentration of hEC to huAEC medium with VEGF-165 0.5 ng/ml, was optimised for enhanced cell growth in ALI conditions.

Influence of native fibroblasts on co-culture

The noticeable effect of the presence of fibroblasts in the wells with co-culture models was evident (fig. 3.6 (C), (H)) with a uniform epithelial lining over the top of a finely based membrane-like structure separating the endothelial cells, as shown in the immunofluorescence staining against CD31 marker for endothelial cells (fig. 3.9 (C), (F)). The models without the fibroblast did not appear aligned (fig. 3.6 (A), (B),

(G)). With PCL:PTMC 50:50, the epithelial layer appeared more intact and showed the presence of the thinnest blue-stained mucosal lining on top in alcian blue staining results at the end of day 12 (fig. 3.8 (B)). A valid alveolar tissue model (similar to fig. 1.1 (C)) requires monolayers of both epithelial with endothelial layers connected through ultra-thin membrane. In order to achieve this, to avoid multilayering, we ended the co-culture after day 12 to achieve an epithelium monolayer; however, further optimisation needs to be taken as the cell seeding density can be taken into account. Additionally, specifically at day 12, it suggested a possibility of endothelial cells migrating through the membrane from the basal sides towards making contact with the epithelial cell layer. This may reinstate the vital presence of fibroblasts in the co-culture of endothelial and epithelial cells. Hence, we believe that the scaffold membrane mix of 50:50 PCL:PTMC was found to be suitable for generating a (triple) co-culture model of alveolar epithelium and endothelium, and the scaffold thickness can also be further thinned to make it more biomimetic to that of native alveoli. The choice of huAEC cells appears to be superior over the commonly available commercial cell lines as well as cells derived from biopsies, which are also difficult to culture for longer culture durations. Alveolar airway huAEC cells also provided the advantage of their dynamic polarisation towards AT1 phenotype when exposed to the micro-environmental stimuli and hence were selected for developing these models. Moreover, fibroblasts positively affecting the cellular polarisation of epithelial and endothelial cells were derived and cultured from native human lung biopsies, which may be one reason for their influence of polarisation among the role of providing necessary stimulations for ECM remodelling.

Influence of optimised co-culturing strategies

Complex co-cultures while generating *in vitro* lung models have been researched extensively. For instance, the development of an alveoli-capillary barrier using lung epithelial cell lines in co-culture with human pulmonary microvascular endothelial cells has shown promising results in the formation of a tight epithelial barrier and reduced permeability in alveolar tissue models [119, 120]. Or more complex triple co-culture of human alveolar epithelium, endothelium, and macrophages was shown to establish a significant biological barrier [120]. Models developed using a new human alveolar epithelial cell line (hAELVi—human Alveolar Epithelial Lentivirus immortalised) (derived from human primary alveolar epithelial cells) with type I-like characteristics expressed functional tight junctions to replicate the air-blood barrier accurately [112]. In contrast to traditional cell lines, this model was able to not only show selective permeability with intercellular barrier function, but the cell line could be kept in culture over several days, up to passage 75, in addition

to liquid-liquid as well as air-liquid conditions. Thus making them a promising candidate to mimic the functional properties of the human alveolar epithelium more reliably, considering reproducibility while offering a valuable tool for lung research [112]. Further investigation using co-culturing of huAEC with endothelial as well as native lung biopsy-derived fibroblasts thus may help gain a newer perspective when used in conjunction with selective scaffold materials. Co-culturing sequences may also significantly impact barrier formation and permeability in *in vitro* tissue models, particularly in complex, multi-cellular constructs like alveolar tissues [119]. In this study, two cell seeding sequences were explored to assess their influence on apparent permeability (Papp). Cell seeding sequence A is where, hECs were seeded first on the basal side, followed by huAECs on the apical side. Cell seeding sequence B was with huAECs seeded first on the apical side, followed by hECs on the basal side.

The effects of each cell seeding sequence across different synthetic scaffold materials showed changes in apparent permeability measured over time along the co-cultured models. The following paragraphs summarise Papp changes observed in each membrane variant under these seeding strategies in order to understand their suitability for establishing effective *in vitro* alveolar tissue models.

PCL:PTMC 70:30 combination, showed a higher Papp for cell seeding sequence A at $8.20 \times 10^{-5} \text{ cm/s}$, compared to $6.10 \times 10^{-5} \text{ cm/s}$ for sequence B on Day 7, suggesting that sequence B provides a stronger early barrier. By Day 10, both sequences show reductions in permeability, reaching $4.94 \times 10^{-5} \text{ cm/s}$ and $4.83 \times 10^{-5} \text{ cm/s}$ for sequences A and B, respectively, which likely indicates tight junction formation and enhanced barrier function as cells settle on the scaffold. Observed early reduction in Papp may point towards the high flexibility and elasticity offered by both PCL and PTMC. The generated mixtures with high PCL content did promote initial cell attachment and spreading, with a reduction in Papp suggesting barrier formation through dynamic cell-matrix interactions [29]. Fluctuations in Papp after Day 14, particularly with sequence A, suggest ongoing cell remodelling processes, reflecting adaptability to the substrate's mechanical properties and permeability over time, as documented in studies on electrospun PCL scaffolds [121].

On day 7, the Papp for sequence A for the PCL:PTMC 50:50 membrane models was $7.41 \times 10^{-5} \text{ cm/s}$; and reduced to $4.28 \times 10^{-5} \text{ cm/s}$ by day 10, comparable to the Papp for PCL:PTMC 70:30 membrane models with sequence B. Thus promoting the balanced blend membrane with its flexibility and enhanced cellular adhesion properties with regards to increased PTMC content, enhancing barrier function. By Day 28, Papp dropped significantly to $2.01 \times 10^{-5} \text{ cm/s}$, which may also indicate the formation of a stable and mature barrier until 28 days, consistent with findings on

PCL's and PTMC's effectiveness in enhancing cell attachment and barrier properties [109] [29].

PA membrane-based co-culture models showed lower Papp of about $5.56 \times 10^{-5} \text{ cm/s}$ with cell seeding sequence B, compared to sequence A of $6.70 \times 10^{-5} \text{ cm/s}$ at day 7. In comparison to the above PCL:PTMC 70:30 it may suggest that PA was able to generate a better early barrier effect. By Day 10, sequence A models showed a significant decrease in Papp to $2.88 \times 10^{-5} \text{ cm/s}$, demonstrating strong barrier formation as cells mature and establish junctions. PA is known to show hydrophilic properties to promote cell adhesion in response to cell-matrix interactions [121]. With the observed measurable reduction in Papp value by day 10 of culture in comparison to PCL, PTMC membrane variants may make it better suited for long-term cultures.

Formerly, research studies based on *in vitro* models on PET membranes are known to promote tighter cell junctions and strong barrier formations. In our observation, the co-cultured PET membrane models with huAEC and hECs did show initial Papp values of $6.45 \times 10^{-6} \text{ cm/s}$ (sequence A) and $2.55 \times 10^{-6} \text{ cm/s}$ (sequence B) at day 7. Noticeably, sequence B with reduced Papp indicated tighter cell organisation and initial barrier formation. However, by day 10, Papp increased slightly for sequence A. This variability can be justified by PET's hydrophobic nature, which may impact cell adhesion and junction stability. PET's high initial permeability without cells ($5.79 \times 10^{-5} \text{ cm/s}$) shows that adding cells greatly improves its barrier function. This aligns with PET's known properties, which are generally resistant and support cellular layers well under the right conditions [122].

5.1.4 Interpretation of scaffold mechanical properties

Analysing the tensile strength and Young's modulus of these membranes shows how each material meets the mechanical needs of *in vitro* alveolar tissue models.

PET, with its high modulus of elasticity typically around 2-4 GPa in studies, offers strong structural support due to its rigidity, but this may reduce flexibility and limit its use in dynamic models like alveolar tissues. The material's resistance and high barrier function, however, make it an excellent candidate for models focused on maintaining a stable, impermeable barrier, particularly in shorter-term or static cultures where elasticity is less critical [122].

The PCL:PTMC 70:30 membrane, with its even lower average Young's modulus (0.0910 MPa) and tensile strength (0.183 MPa), provides a more elastic scaffold but may lack the strength necessary to maintain structural stability over long-term cultures. The hollow pores observed in this variant suggest possible inconsistencies in electrospinning, which might affect its uniformity. These features imply it may work well for short-term applications or models requiring high elasticity, but its structural strength might be inadequate for long-term use [29]. The PCL:PTMC 50:50 membrane offers a more balanced option, with a lower Young's modulus of about 0.1745 MPa, giving it added flexibility from PTMC. This flexibility could help it mimic the expansion and contraction of alveolar regions. Its tensile strength is 0.3225 MPa, which is lower than PA but may still support cell attachment and barrier formation, as shown by its stable Papp over time. This membrane's mechanical adaptability combined with favourable permeability trends makes it particularly suitable for alveolar tissue modelling, where dynamic stretching is needed for physiologic accuracy [109].

The PA membrane shows a high average tensile strength of 3.2075 MPa and an average Young's modulus of 0.5881 MPa, indicating considerable stiffness and resistance to tension. Such mechanical properties suggest that PA could provide a stable and supportive scaffold, though its rigidity may limit its flexibility in replicating the complex mechanical dynamics of alveolar tissues, which typically require more flexibility [121].

5.2 Standardisation challenges with mucus characterisation methodologies

5.2.1 Protein quantification and mucin content analysis

Extracting and measuring large mucin proteins like Muc5AC and Muc5B is difficult due to their size and complex properties. In our experiments, traditional SDS-PAGE gel electrophoresis didn't successfully separate these high-molecular-weight proteins. When stained with Coomassie blue, no distinct bands for Muc5AC or Muc5B were visible, even when using a protein ladder range of 15–250 kDa and gel concentrations of 4-7 % and 4-8 %. This outcome matches the known limits of SDS-PAGE for enormous proteins, which often exceed their weight capacity.

To address this issue, we used incubation with ACC (acetylcysteine) solution across multiple incubation times (M0 through M6, corresponding to 0–60 minutes of treatment). Although ACC effectively solubilises mucins by reducing disulphide bonds, protein quantification via Bradford assay showed variability in protein concentration. Even repeated gel electrophoresis runs continued to show limited success in resolving these mucins. Bands were either faint or absent. In initial western blot analysis stained for Muc5AC in selected samples (M0, M2, and M4), the mucins positive for Muc5AC appeared as high-intensity bands clustered near the top of the gel, indicating incomplete migration due to their large molecular size. The ACC treatment, while partially effective, could not sufficiently lower the molecular weight or allow complete electrophoretic migration of these mucins. Similar problems were also depicted in some research studies, where large mucins like Muc5AC and Muc5B, exhibiting complex glycosylation patterns and extensive polymerisation, tend to impede migration even when reduced and denatured [67].

Our results show the need for better methods to reliably measure and separate large mucins in airway mucus studies. Using gels with lower cross-linking or switching to agarose gels may improve separation. Other methods, like microfluidic or capillary electrophoresis, may also help by providing clearer results and potentially providing better resolution and quantification reliability [67, 123].

5.2.2 Physical characterisation methods

Surface tension analysis challenges

In our experiments for surface tension (ST) the values measured across various mucus samples stabilised over time through repetitive cyclic measurements. This underlines the importance of dynamic testing for mucus characterisation. The observed stabilisation trend was found to be consistent with prior studies highlighting that initial ST values of mucus samples can vary significantly due to factors like humidity, evaporation, and mucin interactions, which tend to stabilise as the measurement environment equilibrates [67].

In our observation, the mucus directly measured on *in vitro* models presented slightly higher average ST values compared to mucus samples extracted with PBS and lung lavage samples. Previous studies also suggest that *ex vivo* or hydrated mucus samples may exhibit reduced surface tension due to the altered rheological and hydration conditions introduced by extraction fluids [123]. We believe that higher surface tension in intact mucus layers may play a critical role in maintaining the airway surface liquid (ASL) structure, which is a key factor for effective barrier properties and clearance of foreign particles [124].

Interestingly, our data show that ST values across weekly intervals (directly measured on the model) tend to stabilise, suggesting that repetitive movement cycles reduce variability in measurements by balancing surface tension forces. The consistent ST values likely show a stable mucus layer structure at ALI interface, which is essential for simulating realistic airway conditions [124]. Similar results have been seen in studies on how surface tension affects mucus transport and stability, where steady values improve the predictability of mucus behaviour under airflow conditions [125].

Our comparison between software-calculated values and selected cycle averages suggests that custom measurement protocols are preferable for establishing accurate ST values in biofluids. While the software provided initial estimations, manually selected stable values proved more reliable for depicting true mucus surface tension properties, as previously recommended for precise surface and interfacial tension measurements in complex fluids [126].

In summary, our results show that cyclic testing is important for getting stable ST measurements in mucus samples, especially when comparing direct *in vitro* mucus with extracted and lavage samples. These findings point to the need for specific surface tension protocols to accurately describe mucus properties, which helps in developing airway models and designing respiratory treatments.

Viscoelasticity analysis*Storage G' and loss modulus G'' behaviour of mucus sample at varying frequencies:*

In the first step of amplitude sweep analysis, G' showed a sharp decrease at lower frequencies of 1 and 5 rad/s as strain amplitude increased to 0.63 %. At higher strains from 0.994 % to 9.97 %, G' decrease was not very profound for frequencies 1 to 10 rad/s. Here, as strain increases, G' values tend to converge. From the observed trend in G' , it was clear that the mucus exhibited a strong elastic response at strains below 1 %, where the material resisted deformation, suggesting the presence of yield stress. This solid-like behaviour was especially evident at low frequencies, where the internal structure providing elasticity likely breaks down more quickly under strain, leading to a strain-softening effect. After 1 % strain, the material transitioned to a more linear viscoelastic response, showing typical behaviour for a viscoelastic material. This transition is consistent with the expected strain-softening behaviour at low frequencies, where the material's elasticity decreases as strain increases

Loss modulus G'' also showed a decrease with increasing strain amplitude and then stabilised at a certain point for all frequencies. At lower strains until 1 % amplitude, G'' values are generally lower than G' , especially at low frequencies, indicating more elastic behaviour at small deformations. As strain amplitude increases, G'' approaches or exceeds G' , particularly at 100 rad/s, indicating a shift toward more viscous behaviour. The rate of G'' reduction with strain amplitude was seen varying by frequency. Higher frequencies (50 rad/s and 100 rad/s) show a gradual decline in G'' , stabilising at higher G'' values beyond 3 % strain. Whereas for lower frequencies (1, 5 and 10 rad/s) G'' exhibits a sharper initial decrease, followed by almost stables around 4 % strain but at lower values compared to higher frequencies 50 and 100 rad/s. This suggests that the material's viscous response depends strongly on frequency, with a shift toward higher viscosity under rapid oscillatory motion at higher strains, which may be important for applications requiring controlled energy dissipation across different frequencies.

Storage G' and loss modulus G'' behaviour of mucus sample at varying strain amplitudes:

In the second step of frequency sweep analysis, G' remained generally higher for lower strain amplitudes, with a decrease in G' as strain amplitude increases from 1 to 10 %. This indicates a reduction in the material's elasticity at higher strains. G' values remain relatively stable across different frequencies, suggesting a plateau in the material's elastic response. G' did show some slight increase at higher frequencies ($>10 \text{ s}^{-1}$), especially for lower strain amplitudes (1 and 2 %), but stayed mostly

constant for low frequencies ($< 1 \text{ s}^{-1}$). In conclusion, mucus showed stable elastic properties in this range.

G'' values were also initially higher for lower strain amplitudes with increasing frequency. This may indicate more energy dissipation at higher frequencies. At higher frequencies, G'' increases across all strain levels. A more pronounced increase in G'' was seen for strain amplitudes of 1 and 2 %, suggesting a higher energy dissipation (viscous behaviour). However, since viscosity in oscillatory shear is given by $G''(\omega)/\omega$, the increasing G'' at higher frequencies does not necessarily mean an increase in viscosity. Instead, it suggests shear-thinning behaviour, as viscosity decreases with increasing frequency. Whereas at low frequencies, G'' remains relatively stable, with high values for low strain amplitudes (1 and 2 %) and measurably lower values for 5 and 10 % strain. This trend suggests that at lower strain amplitudes, the system exhibits greater energy dissipation, but as strain amplitude increases, G'' decreases, suggesting reduced viscous dissipation at higher strains.

In general, at lower strain amplitudes, both G' and G'' are higher, with G' dominating slightly. This may primarily indicate an elastic response with some viscous dissipation. As strain amplitude increased, both the G' (elastic) and G'' (viscous) moduli decreased over the frequency range. The decrease in both moduli with increasing strain amplitude suggests a softening behaviour, consistent with shear thinning. Overall, the mucus showed a frequency-dependent response. At higher strains, it becomes less elastic and shows reduced viscosity (as inferred from $G''(\omega)/\omega$), particularly at higher frequencies, reflecting its shear-thinning behaviour.

Viscoelastic Response of Mucus Depicting "Shear-Thinning" Behaviour:

Further calculation of the loss angle δ , provides the understanding of the elastic (storage) and viscous (loss) behaviour of mucus samples extracted from *in vitro* tissue models. It shows the lag between the applied stress and the resulting strain. To summarise, δ of 0° represents a purely elastic response, and $\delta = 90^\circ$ indicates a purely viscous response.

For 1 % strain amplitude, the loss angle fluctuated between 35° and 45° at lower shear rates, showing the material behaves viscoelastically at small strains. The δ value showed a noticeable increase with the increase in shear rate from 10 s^{-1} and reached around 60° at 1 % strain, shifting towards more viscous behaviour. Comparing 10 and 1 % strain amplitude, the loss angle remained generally lower for 10 % strain, between 20° and 35° , up to a shear rate of 10 s^{-1} . Beyond this, it δ begins to rise to 70° at high shear rates, but this increase is less noticeable than at 1 % strain. At low strain, mucus was highly viscoelastic and behaved like a more viscous fluid at higher shear rates. Whereas at high strain, mucus tries to retain its

elasticity, even at increased shear rates. In conclusion, it can be said that higher strain amplitudes result in more elastic behaviour, likely due to structural alignment or strain-hardening effects that stabilise the material.

From the same frequency sweep data, dynamic viscosity (loss) was calculated for different strain amplitudes. This helps to gain insight into flow behaviour as well as how mucus tries to resist deformation under shear stress at different frequencies. By analysing such a viscosity trend change with frequency, it is possible to understand how mucus behaves more like a solid or a liquid under different conditions. This can also be correlated to the behaviour of mucus under different physiological or mechanical conditions, such as in the respiratory or digestive systems, where it needs to be both elastic (to trap particles) and viscous (to flow smoothly).

In general, dynamic viscosity showed a decreasing trend with increasing shear rate, analogous to a shear-thinning behaviour. This trend is observed across all strain amplitudes (1, 2, 5, and 10 %), with viscosity decreasing in a power-law manner as the shear rate increased. Interestingly, at a shear rate of 100 s^{-1} , measured dynamic viscosity for each % strain amplitude closed in. Hence, at high shear rates, the strain amplitude may have very little effect on the viscosity. This is typical for materials with both elastic and viscous characteristics, where higher shear rates disrupt the material's internal structure, leading to similar flow behaviour regardless of strain amplitude. Mucus, as a non-newtonian fluid, did show shear-thinning behaviour that may be caused by the alignment of structural components or breakdown of interactions under shear.

In conclusion, at low shear rates, mucus showed more solid-like behaviour with high viscosity but a moderate viscoelastic balance, especially at low strain. A decrease in the shear viscosity at high shear rates shows that mucus tries to transition to a more flowable state. The loss angle increases at 1 % strain, showing more viscous behaviour, while at 10 % strain, the loss angle remains lower, indicating that the material retains more elasticity. Higher strain amplitudes (10 %) result in lower δ , suggesting a more elastic and less dissipative response, likely due to structural rearrangements or increased interparticle interactions. These findings highlight how the mucus responds to varying shear and strain conditions, exhibiting shear-thinning behaviour and a shift from elastic to viscous behaviour with increasing shear rate.

6

Conclusion

Generating 3D *in vitro* tissue models of human airway and especially deep lung tissue equivalents is crucial to studying aerosol generation as a pre-requisite for virus encapsulation. The region-specific and functional tissue constructs need to mimic the inherent heterogeneity and mechanical properties of the respiratory tract. The lung's complex structure and mix of cells make it challenging to create models that accurately represent different parts of the airways and their ability to regenerate.

In airway models, the heterogeneous and regenerative nature of the human airway system complicates stem cell source identification, necessitating critical improvements in source identification and stem cell expansion to reduce variability in *in vitro* outcomes [127–129]. 3D co-culture tissue models using niches selected based on essential properties of the airway region can help replicate cell-cell and cell-ECM interactions [130]. A critical compromise should be attained in the fabrication of region-specific niches and cellular components when developing airway models.

The use of adult stem cells in generating 3D lung organoids marks a significant advancement in Tissue Engineering, especially for modelling respiratory diseases like COVID-19. Organoids do provide reproducible results concerning disease response compared to preclinical animal models. However critical reviews of such adult stem cell-derived models have found them to often rely on undefined media compositions and lack non-epithelial components like immune and endothelial cells, which are essential for comprehensive disease modelling and therapeutic testing [131].

A universal 3D *in vitro* model cannot meet all the diverse requirements needed to replicate the entire human lung airway system. Therefore, distinct tissue models are essential for different regions of the human airway, specifically the upper airway, lower airway, and deep lung alveoli.

A key outcome of this work is the successful application of optimised co-culture strategies using electrospun polymeric membranes, designed to closely approximate the native extracellular matrix (ECM) and promote functional cellular organisation.

Key characteristics required for biomimetic and region-specific ECM modelling were considered, including thinness and the ability to form functional mucus. Nearly all models from the upper airway to deep lung alveoli demonstrated functional mucus/surfactant production, with observed thickening of the mucus layer after four weeks of culture. In addition to the available scaffold options like biologically derived SIS-Muc and commercially available PET, this study introduced novel electrospun membrane variants. For the first time, flexible porous membranes using PTMC and PCL polymer mixtures, namely PCL:PTMC 70:30 and 50:50 and PA, fabricated via electrospinning technology, were employed to create co-cultures of primary human endothelial cells with human airway alveolar epithelial cells. Both PCL:PTMC mixtures-based membrane models as well as PA showed promising results, displaying important characteristics such as CD31-positive endothelial cells aligning with E-cadherin-positive epithelial cells.

This work also highlights the importance of fibroblast inclusion in co-culture, as native lung-derived fibroblasts contribute to mechanical alignment and structural organisation within the tissue models. By enabling the formation of layered cell arrangements and ECM remodelling, fibroblasts enhance tissue maturation, bringing these models closer to mimicking the architecture and function of native lung tissues.

Additionally, the influence of optimised cell seeding sequences on apparent permeability demonstrated how cellular arrangement affects barrier function, with the huAEC first sequence promoting better early barrier formation across several membrane types. These insights emphasise that tailored scaffold properties and seeding configurations are critical for creating stable, functional barriers that can replicate alveolar behaviour.

6.1 Suitability for *in vitro* Alveolar Tissue Models Based on Mechanical Properties and Apparent Permeability

Evaluating both mechanical properties and apparent permeability (Papp) trends for each membrane variant provides insights into their suitability for *in vitro* alveolar tissue models. Considering each membrane's ability to support stable tissue formation and effective barrier function based on Young's modulus, tensile strength, and permeability changes over time with specific cell seeding sequences, we arrived at the following conclusions.

Various studies have suggested that commercially available PET membranes, with their notably high modulus of elasticity (2-4 GPa), provide strong structural support but limited flexibility. However, this could limit their application in dynamic tissue models like alveolar tissue. We replicated our models with the co-culture of hEC-huAEC with LbFb under the same conditions with optimised coating solutions and medium mixtures on PET membrane. The initial Papp for sequence B was found to be significantly lower to $2.55 \times 10^{-6} \text{ cm/s}$ compared to sequence A, reflecting stronger early barrier formation. In our conclusion, we believe that PET's high structural rigidity effectively supports impermeable barriers, but its low flexibility may restrict its applicability in models requiring dynamic motion. PET's high barrier function and resistance make it a strong candidate for applications emphasising barrier stability over mechanical flexibility [122].

PA Membrane: The PA membrane showed an average Young's modulus of 0.5880 MPa and tensile strength of 3.2075 MPa. In our analysis with both cell seeding sequences of co-culture of hECs and huAECs, the membrane offered a stable and robust structure and improved handling. Additionally, it supported the migration of hECs in the case of sequence B of cell seeding. The initial Papp values were lower in cell seeding sequence B, where huAECs were seeded first on the apical side, followed by endothelial cells hECs on the basal side. This configuration facilitated early tight junction formation, as reflected by the low Papp at Day 7 ($5.56 \times 10^{-5} \text{ cm/s}$) and further reductions over time. By Day 10, sequence A achieves a stable and even lower Papp ($2.88 \times 10^{-5} \text{ cm/s}$), indicating that PA's hydrophilic surface promotes consistent cell adhesion and barrier formation as cells mature. These stable permeability trends and PA's supportive mechanical profile make it suitable for applications requiring robust, long-term barrier integrity in alveolar models [121].

PCL:PTMC 50:50 membrane samples measured an average Young's modulus of 0.1745 MPa and tensile strength of 0.3225 MPa. This suggests that the membrane offers greater flexibility, which is advantageous for modelling alveolar tissue me-

chanics where dynamic expansion and contraction are vital. With the sequence A cell seeding approach, Papp trends show a marked reduction from $7.41 \times 10^{-5} \text{ cm/s}$ Day 7 to $4.28 \times 10^{-5} \text{ cm/s}$ by day 10, indicating robust barrier formation likely facilitated by PCL and PTMC's cell-supportive properties. By Day 28, Papp further reduced to $2.01 \times 10^{-5} \text{ cm/s}$, confirming that the membrane can sustain a stable barrier over time as tight junctions develop. For long-term, flexible alveolar models, scaffolds need similar attributes with flexibility as well as necessary tensile strength as provided by this membrane variant.[29, 109].

PCL:PTMC 70:30 membrane variant showed a lower Young's modulus (0.0910 MPa) and tensile strength (0.183 MPa), providing high elasticity but potentially reduced durability under stress. Noticeable differences were observed in samples of this membrane variant, with pronounced hollow areas in later sections of the membrane contributing to variability in the measured values for tensile strength and Young's modulus. Hence further modifications are necessary in the production process and post-processing steps for this particular mixture with a high proportion of PCL electrospun membrane. The reliability of the mechanical property measurements for this membrane variant remains inconclusive. Furthermore, the initial Papp in sequence B was lower ($6.10 \times 10^{-5} \text{ cm/s}$) than in sequence A. This may indicate that seeding huAECs first supports early tight junction formation. However, after Day 14, high variations were also seen with sequence A models. This may indicate that the 70:30 blend may struggle to maintain a stable barrier over prolonged culture periods. The higher elasticity and fluctuating permeability may limit its suitability for applications requiring long-term barrier stability, though it could work well in short-term, elasticity-prioritised models [29].

In conclusion, PET, with its rigidity and high Young's modulus, does provide a high barrier function. Hence, it could work best for barrier-centric, static tissue models. However, the same qualities limit its suitability for use in demanding human alveolar tissue models requiring intentional flexibility for ECM along with the required tensile strength and thinness. Hence, it may also not be suitable while transferring the *in vitro* tissue to dynamic bioreactor systems with the provision of mechanical stimulation such as breathing mechanics.

The PCL:PTMC mixture membranes, specifically the 50:50 membrane with cell seeding sequence A, emerge as the most balanced choice for alveolar models requiring sustained flexibility and barrier integrity. Although PCL:PTMC 70:30 does provide similar advantages as the 50:50 variant but possesses the limitation of reduced durability on account of increased PCL content. Further optimisation in relation to the electrospun strategy is required to manipulate the mechanical performance of the 70:30 variant. Finally, the last electrospun membrane tested, PA, did provide

stable permeability in the overall co-culture setup, and its high tensile strength suits applications needing robust, long-term barriers, while the 70:30 blend may be more suitable for short-term, elasticity-focused models.

6.2 Challenges to mucus physical characterization methods

Characterising mucus is challenging. One difficulty is quantifying and identifying important mucin proteins like Muc5AC and Muc5B. Standard SDS-PAGE methods had trouble migrating these mucins, even after adding ACC treatment. In western blot staining for Muc5AC, incomplete migration and protein buildup at the gel entry were observed. Hence there is the need for optimised methodologies capable of accommodating the distinct biochemical properties of mucins.

Also, the characterisation of mucus surface tension in airway models requires a controlled and repetitive measurement approach. The influence of environmental conditions, particularly given the variability caused by sample drying and preparation methods, are possible limitations. This work also provides a reliable ST measurement methodology that is applicable for *in vitro* airway models, which is essential for the development of therapeutic interventions targeting mucus-related respiratory conditions.

Our rheological analysis of mucus using amplitude and frequency sweeps for a range of strain amplitude as well as a range of frequencies, in contrast to other studies, did provide a deeper understanding of the mucus's behaviour. In our experiments, the mucus sample showed a frequency-dependent viscoelastic response, moving from elastic to viscous behaviour as strain and frequency increased. At low strain amplitudes, mucus behaved more elastically, with higher storage modulus (G') and lower loss modulus (G''), suggesting that it behaves more like a solid. As strain amplitude increased, both G' and G'' decreased, showing the mucus becoming more viscous and less elastic. This trend is noticeable at higher frequencies, where mucus shows a shift towards more viscous behaviour, with energy dissipation increasing as strain amplitude and frequency rise.

Loss angle δ calculations showed that at low strains (1 %), mucus was able to maintain a more balanced viscoelastic character. At higher strains (10 %), it became more elastic, even at increased shear rates. This can be because of structural rearrangements of the heavy mucins or strain-hardening effects stabilizing the mucus at higher strains.

In terms of shear viscosity, the mucus displays typical shear-thinning behaviour, where viscosity decreases with increasing shear rate. This behaviour is observed across different strain amplitudes and indicates that the material becomes more flowable and less resistant to shear stress at higher frequencies and shear rates. The curves generated for shear viscosities also depicted a diminishing effect of strain amplitude on viscosity under rapid shear conditions. This combination of properties

makes mucus an adaptable material, capable of both trapping particles and flowing smoothly under varying physiological conditions. Understanding these behaviours is crucial for applications that involve mucus, as it helps predict its performance in biological and mechanical systems where it must respond to changing forces and flow dynamics.

7

Future work

Building on the advancements made in developing 3D *in vitro* lung models, future work should focus on the following points:

1. Exploration of alternative fabrication methods (e.g., bioprinting, for increased control over ECM-like structures
2. Adjustment of polymer ratios (e.g., varying PCL ratios) to tailor degradation rates, considering how increased PTMC content could affect mechanical stability.
3. Investigation of fibre orientation and porosity, particularly the effects of PCL fibre alignment on cell behaviour and scaffold properties, with randomised fibres potentially offering better ECM mimicry.
4. Development of 3D curved structures to replicate the morphology of alveolar sacs, which could be incorporated into dynamic models to simulate airflow.
5. Incorporation of breathing mechanics in a bioreactor setup to simulate respiratory motion, affecting cell interaction, ECM behaviour, and integration of immune cells (e.g., THP-1-derived macrophages).
6. Real-time, label-free imaging (e.g., multi-photon microscopy) to monitor cell behaviour and tissue development within the bioreactor.
7. Application to disease modelling and drug testing, using enhanced, region-specific lung models for applications like COVID-19, COPD, and asthma research.

Electrospinning provided a practical and bioactive method for making scaffolds in this study. However, newer technologies like bioprinting offer more control over scaffold design. These newer methods could improve our ability to mimic complex ECM structures. But bioprinting may also increase fabrication time and cost. Future

research should look into using these new technologies, possibly together, to create better membranes that more closely match the features of native lung tissue. These membranes should mimic the structure, thickness, and pathways for cell migration. This could help overcome current challenges like inconsistent pore sizes and structural differences.

Another avenue for future exploration is optimising polymer blending ratios to tune scaffold degradation rates for specific experimental time frames. Adjusting PCL and PTMC ratios, for example, could tailor the scaffold's mechanical properties and lifespan to match the requirements of short- or long-term studies. Higher PTMC ratios, while potentially improving degradation rates, may compromise mechanical integrity; thus, they need additional investigation to carefully balance polymer content to maintain membrane durability without compromising model stability during cell culture. Such refinements could create scaffolds that align with diverse study needs, from rapid testing to extended *in vitro* experiments.

The effects of fibre alignment on scaffold performance cannot be neglected, particularly with high PCL content. Highly aligned fibres can influence cellular orientation and mechanical anisotropy, potentially affecting both cell behaviour and barrier properties in tissue models. Randomised fibre arrangements, as in our membrane variants, may prove to be more advantageous for simulating the natural, non-directional structure of lung ECM, while controlled pore size and fibre distribution might better facilitate cell adhesion, nutrient diffusion, and waste removal.

The current scaffold models are layered, which provides large areas for interaction. However, they do not have the 3D curvature and depth found in alveolar sacs. In the future, making scaffolds with curved or dome shapes could make them more like alveolar structures. This would increase the accuracy of lung models. Adding these 3D shapes to bioreactor systems could allow studies on airflow and mechanical stretching. These factors are important for mimicking the breathing process. Future studies should incorporate these 3D models into bioreactor systems that support airflow dynamics and simulate lung tissue stretching. This could help recreate the air-blood interface, improving cell-to-cell and cell-to-ECM interactions. Testing these models with controlled airflow and humidity could give valuable information about how respiratory movement affects barrier function, cell differentiation, and immune cell behaviour. For example, adding THP-1-derived macrophages to the bioreactor medium would allow immune response studies in more realistic conditions.

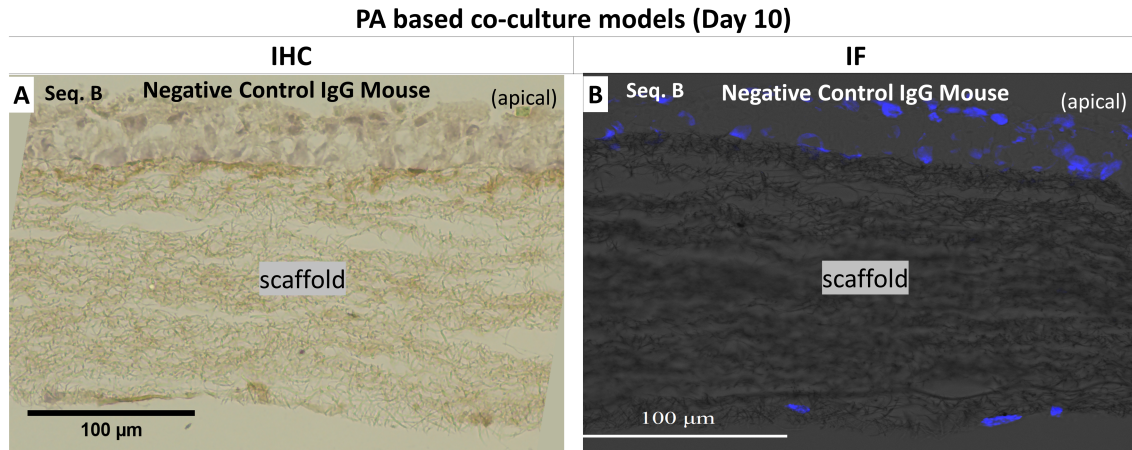
Another promising area for research is the use of label-free imaging techniques, like multi-photon microscopy. This technique lets researchers observe tissue development without needing to apply labels. It can track how cells behave and how the

ECM forms over time. Future studies using label-free, real-time imaging in conjunction with bioreactor systems would allow continuous tracking of tissue growth, cell arrangement, and their response to mechanical changes. This noninvasive imaging would also simplify monitoring tissue development and allow for adjustments during experiments.

Advanced models hold significant potential for understanding respiratory conditions like COVID-19, COPD, and asthma. The next crucial step for improvising these model constructs can be focused on including immune cells and blood vessels. This will make them more suitable for drug testing and treatment development.

Supplementary figures

Supplementary Figure 1:



Supplementary Figure 7.1: PA based 3D *in vitro* co-culture models of hEC-huAEC-LbFb, showing negative control staining for IHC and IF done against CD31 endothelial marker. Negative control staining was performed using primary antibody specific host serum, here IgG mouse in the same concentration of primary antibody CD31. No positive signals were present in case of both IHC (brown) and IF (green fluorescence conjugated) stainings as seen in figure A and B resp..

Supplementary Figure 2:

6 values associated with exact repetitive periodic movements (weight vs time) cycles are considered for averaging the ST values							
Week1		Week 2		Week 3		Week 4	
Average 1	STDev 1	Average 1	STDev 1	Average 1	STDev 1	Average 1	STDev 1
32,497	0,509063	30,4884	1,51054	31,46432	1,684922	30,05406	0,183391
37,565	1,085121	26,0778	1,894296	30,4	1,136508	31,58931	2,371933
34,706	2,037612	30,96905	0,745939	23,69661	0,828175	31,26656	0,41376
31,946	2,907596	29,69413	1,809058	30,3356	2,422115	29,96691	2,984705
34,841	1,484363	32,30278	2,503053	32,36842	1,504825	30,49092	2,786377
				35,07036	1,864015	30,98469	1,517784
				30,22551	0,786092	31,3254	0,404321
				32,78134	0,697484	29,82254	0,584793
				32,54257	1,34768		
34,3114		29,90643		30,98719		30,68755	
2,230953		2,340609		3,433545		0,725732	

Supplementary Figure 7.2: Data selection and analysis after multiple ST measurements for mucus samples from *in vitro* tissue models at weeks 1, 2, 3 and 4. Table highlights the selected data values measured for Surface tension. Only the values corresponding to the repetitive cycles measurements are selected as depicted in fig. 3.18 (A)

Bibliography

- [1] Caitlin E. Edwards, Aleksandra Tata, and Ralph S. Baric. “Human lung organoids as a model for respiratory virus replication and countermeasure performance in human hosts”. In: *Translational Research* 250 (Dec. 2022). Publisher: Elsevier, pp. 36–45. ISSN: 1931-5244. DOI: 10.1016/j.trsl.2022.07.002. URL: <https://doi.org/10.1016/j.trsl.2022.07.002> (visited on 10/12/2024).
- [2] Aditya R. Kolli et al. “Pulmonary Delivery of Aerosolized Chloroquine and Hydroxychloroquine to Treat COVID-19: In Vitro Experimentation to Human Dosing Predictions”. en. In: *AAPS J* 24.1 (Jan. 2022), p. 33. ISSN: 1550-7416. DOI: 10.1208/s12248-021-00666-x. URL: <https://link.springer.com/10.1208/s12248-021-00666-x> (visited on 10/12/2024).
- [3] W Allaerts. “Biophysical parameters affecting lung surfactant function, surface tension and the transition from aerosol to droplet exhalation (in relation to COVID-19 infection)”. In: *J. Phys.: Conf. Ser.* 1730.1 (Jan. 2021), p. 012059. ISSN: 1742-6588, 1742-6596. DOI: 10.1088/1742-6596/1730/1/012059. URL: <https://iopscience.iop.org/article/10.1088/1742-6596/1730/1/012059> (visited on 10/12/2024).
- [4] Yunchen Bu, Ryoza Ooka, Hideki Kikumoto, and Wonseok Oh. “Recent research on expiratory particles in respiratory viral infection and control strategies: A review”. en. In: *Sustainable Cities and Society* 73 (Oct. 2021), p. 103106. ISSN: 22106707. DOI: 10.1016/j.scs.2021.103106. URL: <https://linkinghub.elsevier.com/retrieve/pii/S2210670721003899> (visited on 10/12/2024).
- [5] Natalie Heinen, Mara Klöhn, Eike Steinmann, and Stephanie Pfaender. “In Vitro Lung Models and Their Application to Study SARS-CoV-2 Pathogenesis and Disease”. en. In: *Viruses* 13.5 (Apr. 2021), p. 792. ISSN: 1999-4915. DOI: 10.3390/v13050792. URL: <https://www.mdpi.com/1999-4915/13/5/792> (visited on 04/11/2024).
- [6] Rasika S Murkar, Cornelia Wiese-Rischke, Tobias Weigel, Sascha Kopp, and Heike Walles. “Developing human upper, lower, and deep lung airway models: Combining different scaffolds and developing complex co-cultures”. In: *Journal of Tissue Engineering* 16 (2024). DOI: 10.1177/20417314241299076. URL: <https://doi.org/10.1177/20417314241299076>.
- [7] Barbara Rothen-Rutishauser, Matthew Gibb, Ruiwen He, Alke Petri-Fink, and Christie M. Sayes. “Human lung cell models to study aerosol delivery - considerations for model design and development”. eng. In: *Eur J Pharm Sci* 180 (Jan. 2023), p. 106337. ISSN: 1879-0720. DOI: 10.1016/j.ejps.2022.106337.
- [8] R. Pouliot et al. “Development and characterization of a naturally derived lung extracellular matrix hydrogel.” In: *Journal of biomedical materials research. Part A* 104 8 (2016), pp. 1922–35. DOI: 10.1002/jbm.a.35726.

- [9] E. Marhuenda et al. "Lung Extracellular Matrix Hydrogels Enhance Preservation of Type II Phenotype in Primary Alveolar Epithelial Cells". In: *International Journal of Molecular Sciences* 23 (2022). DOI: 10.3390/ijms23094888.
- [10] Di Huang et al. "Reversed-engineered human alveolar lung-on-a-chip model". In: *Proceedings of the National Academy of Sciences of the United States of America* 118 (2021). DOI: 10.1073/pnas.2016146118.
- [11] Mathieu Maisani, Daniele Pezzoli, Olivier Chassande, and Diego Mantovani. "Cellularizing hydrogel-based scaffolds to repair bone tissue: How to create a physiologically relevant micro-environment?" en. In: *J Tissue Eng* 8 (Jan. 2017), p. 204173141771207. ISSN: 2041-7314, 2041-7314. DOI: 10.1177/2041731417712073. URL: <http://journals.sagepub.com/doi/10.1177/2041731417712073> (visited on 05/26/2024).
- [12] Hans Kresse and Elke Schönherr. "Proteoglycans of the extracellular matrix and growth control". en. In: *Journal Cellular Physiology* 189.3 (Dec. 2001), pp. 266–274. ISSN: 0021-9541, 1097-4652. DOI: 10.1002/jcp.10030. URL: <https://onlinelibrary.wiley.com/doi/10.1002/jcp.10030> (visited on 05/26/2024).
- [13] Cornelia Kasper, Verena Charwat, and Antonina Lavrentieva, eds. *Cell Culture Technology*. Learning Materials in Biosciences. Cham: Springer International Publishing, 2018. ISBN: 978-3-319-74853-5 978-3-319-74854-2. DOI: 10.1007/978-3-319-74854-2. URL: <http://link.springer.com/10.1007/978-3-319-74854-2> (visited on 04/15/2024).
- [14] Saeed Ur Rahman, Sasikumar Ponnusamy, Malvika Nagrath, and Praveen R Arany. "Precision-engineered niche for directed differentiation of MSCs to lineage-restricted mineralized tissues". en. In: *J Tissue Eng* 13 (Jan. 2022), p. 204173142110739. ISSN: 2041-7314, 2041-7314. DOI: 10.1177/20417314211073934. URL: <http://journals.sagepub.com/doi/10.1177/20417314211073934> (visited on 05/26/2024).
- [15] Patricia A Redondo, Marina Pavlou, Marilena Loizidou, and Umber Cheema. "Elements of the niche for adult stem cell expansion". en. In: *J Tissue Eng* 8 (Jan. 2017), p. 204173141772546. ISSN: 2041-7314, 2041-7314. DOI: 10.1177/2041731417725464. URL: <http://journals.sagepub.com/doi/10.1177/2041731417725464> (visited on 05/26/2024).
- [16] Alican Kuşoğlu et al. "Different Decellularization Methods in Bovine Lung Tissue Reveals Distinct Biochemical Composition, Stiffness, and Viscoelasticity in Reconstituted Hydrogels". In: *ACS Applied Bio Materials* 6 (2023), pp. 793–805. DOI: 10.1021/acsabm.2c00968.
- [17] M. Nizamoglu and J. Burgess. "Current possibilities and future opportunities provided by three-dimensional lung ECM-derived hydrogels". In: *Frontiers in Pharmacology* 14 (2023). DOI: 10.3389/fphar.2023.1154193.

- [18] R. D. de Hilster et al. "Human lung extracellular matrix hydrogels resemble the stiffness and viscoelasticity of native lung tissue". In: *American Journal of Physiology - Lung Cellular and Molecular Physiology* 318 (2020), pp. L698–L704. DOI: 10.1152/ajplung.00451.2019.
- [19] Timothy Leach et al. "Development of a novel air–liquid interface airway tissue equivalent model for in vitro respiratory modeling studies". en. In: *Sci Rep* 13.1 (June 2023), p. 10137. ISSN: 2045-2322. DOI: 10.1038/s41598-023-36863-1. URL: <https://www.nature.com/articles/s41598-023-36863-1> (visited on 05/26/2024).
- [20] B. Chuenjitkuntaworn et al. "Polycaprolactone/hydroxyapatite composite scaffolds: preparation, characterization, and in vitro and in vivo biological responses of human primary bone cells." In: *Journal of biomedical materials research. Part A* 94 1 (2010), pp. 241–51. DOI: 10.1002/jbm.a.32657.
- [21] Francesca Gattazzo, Anna Urciuolo, and Paolo Bonaldo. "Extracellular matrix: A dynamic microenvironment for stem cell niche". en. In: *Biochimica et Biophysica Acta (BBA) - General Subjects* 1840.8 (Aug. 2014), pp. 2506–2519. ISSN: 03044165. DOI: 10.1016/j.bbagen.2014.01.010. URL: <https://linkinghub.elsevier.com/retrieve/pii/S0304416514000129> (visited on 08/19/2024).
- [22] Yunzhu Qian et al. "Triple PLGA/PCL scaffold modification including silver-impregnation, collagen-coating, and electrospinning significantly improve biocompatibility, antimicrobial, and osteogenic properties for oro-facial tissue regeneration." In: *ACS applied materials & interfaces* (2019). DOI: 10.1021/acsami.9b07053.
- [23] J. Ferreira, A. Gloria, S. Cometa, J. Coelho, and M. Domingos. "Effect of in Vitro Enzymatic Degradation on 3D Printed Poly(ϵ -Caprolactone) Scaffolds: Morphological, Chemical and Mechanical Properties". In: *Journal of Applied Biomaterials & Functional Materials* 15 (2017), pp. 185–195. DOI: 10.5301/jabfm.5000363.
- [24] Juliana R. Dias, Aureliana Sousa, Ana Augusto, Paulo J. Bártolo, and Pedro L. Granja. "Electrospun Polycaprolactone (PCL) Degradation: An In Vitro and In Vivo Study". en. In: *Polymers* 14.16 (Aug. 2022), p. 3397. ISSN: 2073-4360. DOI: 10.3390/polym14163397. URL: <https://www.mdpi.com/2073-4360/14/16/3397> (visited on 04/11/2024).
- [25] Tyler Nelson, Jed Johnson, and J. Lannutti. "Media-based effects on the hydrolytic degradation and crystallization of electrospun synthetic-biologic blends". In: *Journal of Materials Science: Materials in Medicine* 25 (2014), pp. 297–309. DOI: 10.1007/s10856-013-5077-0.
- [26] C. Lam, D. Hutmacher, J. Schantz, M. Woodruff, and S. Teoh. "Evaluation of polycaprolactone scaffold degradation for 6 months in vitro and in vivo." In: *Journal of biomedical materials research. Part A* 90 3 (2009), pp. 906–19. DOI: 10.1002/jbm.a.32052.

- [27] I. Castilla-Cortázar et al. "Hydrolytic and enzymatic degradation of a poly(ϵ -caprolactone) network". en. In: *Polymer Degradation and Stability* 97.8 (Aug. 2012), pp. 1241–1248. ISSN: 01413910. DOI: 10.1016/j.polymdegradstab.2012.05.038. URL: <https://linkinghub.elsevier.com/retrieve/pii/S0141391012002121> (visited on 04/11/2024).
- [28] Qingchun Zhang et al. "Effect of porosity on long-term degradation of poly (ϵ -caprolactone) scaffolds and their cellular response". In: *Polymer Degradation and Stability* 98 (2013), pp. 209–218. DOI: 10.1016/J.POLYMDEGRADSTAB.2012.10.008.
- [29] Thijs Pasma et al. "Development of an In Vitro Airway Epithelial–Endothelial Cell Culture Model on a Flexible Porous Poly(Trimethylene Carbonate) Membrane Based on Calu-3 Airway Epithelial Cells and Lung Microvascular Endothelial Cells". en. In: *Membranes* 11.3 (Mar. 2021), p. 197. ISSN: 2077-0375. DOI: 10.3390/membranes11030197. URL: <https://www.mdpi.com/2077-0375/11/3/197> (visited on 04/18/2024).
- [30] J. Y. Park et al. "Development of a functional airway-on-a-chip by 3D cell printing". In: *Biofabrication* 11 (2018). DOI: 10.1088/1758-5090/aae545.
- [31] E. Bat et al. "Ultraviolet light crosslinking of poly(trimethylene carbonate) for elastomeric tissue engineering scaffolds." In: *Biomaterials* 31 33 (2010), pp. 8696–705. DOI: 10.1016/j.biomaterials.2010.07.102.
- [32] Jier Y. Han, Tian-Xiang Chen, C. Branford-White, and Li-Min Zhu. "Electrospun shikonin-loaded PCL/PTMC composite fiber mats with potential biomedical applications." In: *International journal of pharmaceutics* 382 1-2 (2009), pp. 215–21. DOI: 10.1016/j.ijpharm.2009.07.027.
- [33] Ana Paula Pêgo, Dirk W. Grijpma, and Jan Feijen. "Enhanced mechanical properties of 1,3-trimethylene carbonate polymers and networks". In: *Polymer* 44.21 (Oct. 2003), pp. 6495–6504. ISSN: 0032-3861. DOI: 10.1016/S0032-3861(03)00668-2. URL: <https://www.sciencedirect.com/science/article/pii/S0032386103006682> (visited on 04/15/2024).
- [34] Erhan Bat et al. "Trimethylene Carbonate and ϵ -Caprolactone Based (co)Polymer Networks: Mechanical Properties and Enzymatic Degradation". In: *Biomacromolecules* 9.11 (Nov. 2008). Publisher: American Chemical Society, pp. 3208–3215. ISSN: 1525-7797. DOI: 10.1021/bm8007988. URL: <https://doi.org/10.1021/bm8007988> (visited on 04/15/2024).
- [35] M. Zhuravleva et al. "In vitro assessment of electrospun polyamide-6 scaffolds for esophageal tissue engineering." In: *Journal of biomedical materials research. Part B, Applied biomaterials* 107 2 (2019), pp. 253–268. DOI: 10.1002/jbm.b.34116.
- [36] Tobias Weigel et al. "Fully Synthetic 3D Fibrous Scaffolds for Stromal Tissues Replacement of Animal-Derived Scaffold Materials Demonstrated by Multilayered Skin". en. In: *Advanced Materials* 34.10 (Mar. 2022), p. 2106780. ISSN: 0935-9648, 1521-4095. DOI: 10.1002/adma.202106780. URL: <https://onlinelibrary.wiley.com/doi/10.1002/adma.202106780> (visited on 08/30/2024).

- [37] Qiu Li Loh and C. Choong. "Three-dimensional scaffolds for tissue engineering applications: role of porosity and pore size." In: *Tissue engineering. Part B, Reviews* 19 6 (2013), pp. 485–502. DOI: 10.1089/ten.TEB.2012.0437.
- [38] G. Morris et al. "A novel electrospun biphasic scaffold provides optimal three-dimensional topography for in vitro co-culture of airway epithelial and fibroblast cells". In: *Biofabrication* 6 (2014). DOI: 10.1088/1758-5082/6/3/035014.
- [39] Tobias Weigel et al. "Flexible tissue-like electrode as a seamless tissue-electronic interface". In: *BioNanoMaterials* 18.3-4 (Jan. 2017). ISSN: 2193-066X. DOI: 10.1515/bnm-2017-0002. URL: <https://www.degruyter.com/document/doi/10.1515/bnm-2017-0002/html> (visited on 10/31/2024).
- [40] Yuehua Yuan and T. Randall Lee. "Contact Angle and Wetting Properties". en. In: *Surface Science Techniques*. Ed. by Gianangelo Bracco and Bodil Holst. Berlin, Heidelberg: Springer, 2013, pp. 3–34. ISBN: 978-3-642-34243-1. DOI: 10.1007/978-3-642-34243-1_1. URL: https://doi.org/10.1007/978-3-642-34243-1_1 (visited on 04/15/2024).
- [41] Li-Chong Xu and Christopher A. Siedlecki. "Effects of surface wettability and contact time on protein adhesion to biomaterial surfaces". In: *Biomaterials* 28.22 (Aug. 2007), pp. 3273–3283. ISSN: 0142-9612. DOI: 10.1016/j.biomaterials.2007.03.032. URL: <https://www.sciencedirect.com/science/article/pii/S014296120700261X> (visited on 04/15/2024).
- [42] Finn J. Hawkins et al. "Derivation of Airway Basal Stem Cells from Human Pluripotent Stem Cells." In: *Cell stem cell* (2020). DOI: 10.1016/j.stem.2020.09.017.
- [43] Zuzanna Bukowy-Bieryłło. "Long-term differentiating primary human airway epithelial cell cultures: how far are we?" en. In: *Cell Commun Signal* 19.1 (Dec. 2021), p. 63. ISSN: 1478-811X. DOI: 10.1186/s12964-021-00740-z. URL: <https://biosignaling.biomedcentral.com/articles/10.1186/s12964-021-00740-z> (visited on 05/30/2024).
- [44] Mahboobe Ghaedi et al. "Human iPS cell-derived alveolar epithelium repopulates lung extracellular matrix". en. In: *J. Clin. Invest.* 123.11 (Nov. 2013), pp. 4950–4962. ISSN: 0021-9738. DOI: 10.1172/JCI68793. URL: <http://www.jci.org/articles/view/68793> (visited on 10/12/2024).
- [45] J. Kerschner et al. "A functional genomics approach to investigate the differentiation of iPSCs into lung epithelium at air-liquid interface". In: *Journal of Cellular and Molecular Medicine* 24 (2020), pp. 9853–9870. DOI: 10.1111/jcmm.15568.
- [46] Krishanu Saha and R. Jaenisch. "Technical challenges in using human induced pluripotent stem cells to model disease." In: *Cell stem cell* 5 6 (2009), pp. 584–95. DOI: 10.1016/j.stem.2009.11.009.
- [47] Viola Volpato and C. Webber. "Addressing variability in iPSC-derived models of human disease: guidelines to promote reproducibility". In: *Disease Models & Mechanisms* 13 (2020). DOI: 10.1242/dmm.042317.

- [48] B. Forbes and C. Ehrhardt. "Human respiratory epithelial cell culture for drug delivery applications." In: *European journal of pharmaceuticals and biopharmaceutics : official journal of Arbeitsgemeinschaft fur Pharmazeutische Verfahrenstechnik e.V* 60 2 (2005), pp. 193–205. DOI: 10.1016/J.EJPB.2005.02.010.
- [49] Marion Möckel et al. "Human 3D Airway Tissue Models for Real-Time Microscopy: Visualizing Respiratory Virus Spreading". en. In: *Cells* 11.22 (Nov. 2022), p. 3634. ISSN: 2073-4409. DOI: 10.3390/cells11223634. URL: <https://www.mdpi.com/2073-4409/11/22/3634> (visited on 04/18/2024).
- [50] J. Harcourt and L. Haynes. "Establishing a liquid-covered culture of polarized human airway epithelial Calu-3 cells to study host cell response to respiratory pathogens in vitro." In: *Journal of visualized experiments : JoVE* 72 (2013). DOI: 10.3791/50157.
- [51] I. George, S. Vranic, S. Boland, A. Courtois, and A. Baeza-Squiban. "Development of an in vitro model of human bronchial epithelial barrier to study nanoparticle translocation." In: *Toxicology in vitro : an international journal published in association with BIBRA* 29 1 (2015), pp. 51–8. DOI: 10.1016/j.tiv.2014.08.003.
- [52] Andrea D. Lehmann et al. "An in vitro triple cell co-culture model with primary cells mimicking the human alveolar epithelial barrier". en. In: *European Journal of Pharmaceuticals and Biopharmaceutics* 77.3 (Apr. 2011), pp. 398–406. ISSN: 09396411. DOI: 10.1016/j.ejpb.2010.10.014. URL: <https://linkinghub.elsevier.com/retrieve/pii/S0939641110002882> (visited on 04/11/2024).
- [53] Hanyu Li, Kazuki Kuga, and Kazuhide Ito. "SARS-CoV-2 Dynamics in the Mucus Layer of the Human Upper Respiratory Tract Based on Host–Cell Dynamics". In: *Sustainability* (2022). DOI: 10.3390/su14073896.
- [54] Louisa Elizabeth Wallace, Mengying Liu, F. V. van Kuppeveld, E. de Vries, and C. D. de Haan. "Respiratory mucus as a virus-host range determinant". In: *Trends in Microbiology* 29 (2021), pp. 983–992. DOI: 10.1016/j.tim.2021.03.014.
- [55] S. Lai, Ying-Ying Wang, D. Wirtz, and J. Hanes. "Micro- and macrorheology of mucus." In: *Advanced drug delivery reviews* 61 2 (2009), pp. 86–100. DOI: 10.1016/j.addr.2008.09.012.
- [56] M. Echaide, C. Autilio, Raquel Arroyo, and J. Pérez-Gil. "Restoring pulmonary surfactant membranes and films at the respiratory surface." In: *Biochimica et biophysica acta. Biomembranes* 1859 9 Pt B (2017), pp. 1725–1739. DOI: 10.1016/j.bbamem.2017.03.015.
- [57] Raju Bej et al. "Mucus-Inspired Self-Healing Hydrogels: A Protective Barrier for Cells against Viral Infection". In: *Advanced Materials* 36.32 (2024), p. 2401745. DOI: <https://doi.org/10.1002/adma.202401745>. eprint: <https://onlinelibrary.wiley.com/doi/pdf/10.1002/adma.202401745>. URL: <https://onlinelibrary.wiley.com/doi/abs/10.1002/adma.202401745>.

- [58] R. Hamed, D. Schenck, and J. Fiegel. "Surface rheological properties alter aerosol formation from mucus mimetic surfaces." In: *Soft matter* (2020). DOI: 10.1039/d0sm01232g.
- [59] Vassilis Karageorgiou and David Kaplan. "Porosity of 3D biomaterial scaffolds and osteogenesis". In: *Biomaterials* 26.27 (Sept. 2005), pp. 5474–5491. ISSN: 0142-9612. DOI: 10.1016/j.biomaterials.2005.02.002. URL: <https://www.sciencedirect.com/science/article/pii/S0142961205001511> (visited on 04/15/2024).
- [60] H. L. Halliday. "Surfactants: past, present and future". In: *Journal of Perinatology* 28 (2008), S47–S56. DOI: 10.1038/jp.2008.50.
- [61] E. Corazza et al. "Human Lactobacillus Biosurfactants as Natural Excipients for Nasal Drug Delivery of Hydrocortisone". In: *Pharmaceutics* 14 (2022). DOI: 10.3390/pharmaceutics14030524.
- [62] T. Curstedt and J. Johansson. "New Synthetic Surfactant – How and When?" In: *Neonatology* 89 (2006), pp. 336–339. DOI: 10.1159/000092871.
- [63] C. Moysidou, C. Barberio, and R. Owens. "Advances in Engineering Human Tissue Models". In: *Frontiers in Bioengineering and Biotechnology* 8 (2021). DOI: 10.3389/fbioe.2020.620962.
- [64] Puja Jain, S. Rauer, M. Möller, and Smriti Singh. "Mimicking the Natural Basement Membrane for Advanced Tissue Engineering". In: *Biomacromolecules* 23 (2022), pp. 3081–3103. DOI: 10.1021/acs.biomac.2c00402.
- [65] A. Lechanteur, José das Neves, and B. Sarmento. "The role of mucus in cell-based models used to screen mucosal drug delivery". In: *Advanced Drug Delivery Reviews* 124 (2017), pp. 50–63. DOI: 10.1016/j.addr.2017.07.019.
- [66] M. Jory et al. "Mucus from human bronchial epithelial cultures: rheology and adhesion across length scales". In: *Interface Focus* 12 (2022). DOI: 10.1098/rsfs.2022.0028.
- [67] Zhenglong Chen et al. "Determination of rheology and surface tension of airway surface liquid: a review of clinical relevance and measurement techniques". In: *Respiratory Research* 20 (2019). DOI: 10.1186/s12931-019-1229-1.
- [68] J. Wykoff et al. "Rapid Viscoelastic Characterization of Airway Mucus using a Bench-top Rheometer." In: *Journal of visualized experiments : JoVE* 182 (2022). DOI: 10.3791/63876.
- [69] Jorge Bernardino de la Serna et al. "Segregated ordered lipid phases and protein-promoted membrane cohesivity are required for pulmonary surfactant films to stabilize and protect the respiratory surface." In: *Faraday discussions* 161 (2013), 535–48, discussion 563–89. DOI: 10.1039/C2FD20096A.
- [70] D. Schürch, O. L. Ospina, A. Cruz, and J. Pérez-Gil. "Combined and independent action of proteins SP-B and SP-C in the surface behavior and mechanical stability of pulmonary surfactant films." In: *Biophysical journal* 99 10 (2010), pp. 3290–9. DOI: 10.1016/j.bpj.2010.09.039.

- [71] D. Song et al. "Modeling airway dysfunction in asthma using synthetic mucus biomaterials". In: *bioRxiv* (2020). DOI: 10.1101/2020.10.16.342766.
- [72] K. Miyazaki et al. "Mucins are Involved in the Intestinal Permeation of Lipophilic Drugs in the Proximal Region of Rat Small Intestine". In: *Pharmaceutical Research* 36 (2019). DOI: 10.1007/s11095-019-2701-9.
- [73] S. Komatsu. "Western Blotting Using PVDF Membranes and Its Downstream Applications." In: *Methods in molecular biology* 1312 (2015), pp. 227–36. DOI: 10.1007/978-1-4939-2694-7_24.
- [74] S. Takehara, M. Yanagishita, K. A. Podyma-Inoue, and Y. Kawaguchi. "Degradation of MUC7 and MUC5B in Human Saliva". In: *PLoS ONE* 8 (2013). DOI: 10.1371/journal.pone.0069059.
- [75] N. Chirwa et al. "A 40-50kDa Glycoprotein Associated with Mucus is Identified as α -1-Acid Glycoprotein in Carcinoma of the Stomach". In: *Journal of Cancer* 3 (2012), pp. 83–92. DOI: 10.7150/jca.3737.
- [76] Leah Wright, T. Barnes, P. Joyce, and C. Prestidge. "Optimisation of a High-Throughput Model for Mucus Permeation and Nanoparticle Discrimination Using Biosimilar Mucus". In: *Pharmaceutics* 14 (2022). DOI: 10.3390/pharmaceutics14122659.
- [77] R. L. Howard et al. "Biochemical and rheological analysis of human colonic culture mucus reveals similarity to gut mucus". In: *Biophysical Journal* 120 (2021), pp. 5384–5394. DOI: 10.1016/j.bpj.2021.10.024.
- [78] M. Völler et al. "An optimized protocol for assessment of sputum macrorheology in health and muco-obstructive lung disease". In: *Frontiers in Physiology* 13 (2022). DOI: 10.3389/fphys.2022.912049.
- [79] Gordian Born et al. "Engineering of fully humanized and vascularized 3D bone marrow niches sustaining undifferentiated human cord blood hematopoietic stem and progenitor cells". en. In: *J Tissue Eng* 12 (Jan. 2021), p. 204173142110448. ISSN: 2041-7314, 2041-7314. DOI: 10.1177/20417314211044855. URL: <http://journals.sagepub.com/doi/10.1177/20417314211044855> (visited on 05/26/2024).
- [80] Moritz Kolster et al. "Outgrowing endothelial and smooth muscle cells for tissue engineering approaches". en. In: *J Tissue Eng* 8 (Jan. 2017), p. 204173141769885. ISSN: 2041-7314, 2041-7314. DOI: 10.1177/2041731417698852. URL: <http://journals.sagepub.com/doi/10.1177/2041731417698852> (visited on 05/26/2024).
- [81] Kirstin Linke et al. "Engineered Liver-Like Tissue on a Capillarized Matrix for Applied Research". en. In: *Tissue Engineering* 13.11 (Nov. 2007), pp. 2699–2707. ISSN: 1076-3279, 1557-8690. DOI: 10.1089/ten.2006.0388. URL: <https://www.liebertpub.com/doi/10.1089/ten.2006.0388> (visited on 04/11/2024).
- [82] Heike Mertsching, Thorsten Walles, Michael Hofmann, Johanna Schanz, and Wolfram H. Knapp. "Engineering of a vascularized scaffold for artificial tissue and organ generation". en. In: *Biomaterials* 26.33 (Nov. 2005), pp. 6610–6617. ISSN: 01429612. DOI: 10.1016/j.biomaterials.2005.04.048. URL: <https://linkinghub.elsevier.com/retrieve/pii/S0142961205003169> (visited on 04/11/2024).

- [83] Rasika Murkar et al. "Establishment of a Human Immunocompetent 3D Tissue Model to Enable the Long-Term Examination of Biofilm–Tissue Interactions". en. In: *Bioengineering* 11.2 (Feb. 2024), p. 187. ISSN: 2306-5354. DOI: 10.3390/bioengineering11020187. URL: <https://www.mdpi.com/2306-5354/11/2/187> (visited on 09/02/2024).
- [84] Thomas G. Mezger. *4th Edition*. Hannover, Germany: Vincentz Network, 2012. ISBN: 9783748600367. DOI: doi:10.1515/9783748600367. URL: <https://doi.org/10.1515/9783748600367>.
- [85] Sigrid A. Langhans. "Three-Dimensional in Vitro Cell Culture Models in Drug Discovery and Drug Repositioning". English. In: *Front. Pharmacol.* 9 (Jan. 2018). Publisher: Frontiers. ISSN: 1663-9812. DOI: 10.3389/fphar.2018.00006. URL: <https://www.frontiersin.org/journals/pharmacology/articles/10.3389/fphar.2018.00006/full> (visited on 04/11/2024).
- [86] Rasheena Edmondson, Jessica Jenkins Broglie, Audrey F. Adcock, and Liju Yang. "Three-Dimensional Cell Culture Systems and Their Applications in Drug Discovery and Cell-Based Biosensors". en. In: *ASSAY and Drug Development Technologies* 12.4 (May 2014), pp. 207–218. ISSN: 1540-658X, 1557-8127. DOI: 10.1089/adt.2014.573. URL: <http://www.liebertpub.com/doi/10.1089/adt.2014.573> (visited on 05/26/2024).
- [87] Róisín M. Owens. "Advanced tissue engineering for in vitro drug safety testing". en. In: *MRS Communications* 13.5 (Oct. 2023), pp. 685–694. ISSN: 2159-6867. DOI: 10.1557/s43579-023-00421-7. URL: <https://doi.org/10.1557/s43579-023-00421-7> (visited on 04/11/2024).
- [88] Xuefei Cao et al. "Invited review: human air-liquid-interface organotypic airway tissue models derived from primary tracheobronchial epithelial cells—overview and perspectives". en. In: *In Vitro Cell.Dev.Biol.-Animal* 57.2 (Feb. 2021), pp. 104–132. ISSN: 1071-2690, 1543-706X. DOI: 10.1007/s11626-020-00517-7. URL: <http://link.springer.com/10.1007/s11626-020-00517-7> (visited on 05/26/2024).
- [89] Kambez H. Benam et al. "Small airway-on-a-chip enables analysis of human lung inflammation and drug responses in vitro". en. In: *Nat Methods* 13.2 (Feb. 2016), pp. 151–157. ISSN: 1548-7091, 1548-7105. DOI: 10.1038/nmeth.3697. URL: <https://www.nature.com/articles/nmeth.3697> (visited on 05/26/2024).
- [90] Kambez H. Benam et al. "Matched-Comparative Modeling of Normal and Diseased Human Airway Responses Using a Microengineered Breathing Lung Chip". en. In: *Cell Systems* 3.5 (Nov. 2016), 456–466.e4. ISSN: 24054712. DOI: 10.1016/j.cels.2016.10.003. URL: <https://linkinghub.elsevier.com/retrieve/pii/S2405471216303222> (visited on 05/26/2024).
- [91] Katelyn L. Sellgren, Elizabeth J. Butala, Brian P. Gilmour, Scott H. Randell, and Sonia Grego. "A biomimetic multicellular model of the airways using primary human cells". en. In: *Lab Chip* 14.17 (2014), pp. 3349–3358. ISSN: 1473-0197, 1473-0189. DOI: 10.1039/C4LC00552J. URL: <https://xlink.rsc.org/?DOI=C4LC00552J> (visited on 05/26/2024).

- [92] Roberto Plebani et al. "Modeling pulmonary cystic fibrosis in a human lung airway-on-a-chip". en. In: *Journal of Cystic Fibrosis* 21.4 (July 2022), pp. 606–615. ISSN: 15691993. DOI: 10.1016/j.jcf.2021.10.004. URL: <https://linkinghub.elsevier.com/retrieve/pii/S1569199321021068> (visited on 05/26/2024).
- [93] Michał Szpinda et al. "Experimental research The normal growth of the tracheal wall in human foetuses". In: *Archives of Medical Science* 5 (2013), pp. 922–929. ISSN: 1734-1922. DOI: 10.5114/aoms.2012.31411. URL: <http://www.termedia.pl/doi/10.5114/aoms.2012.31411> (visited on 10/22/2024).
- [94] Stanisława Bazan-Socha et al. "Reticular Basement Membrane Thickness Is Associated with Growth- and Fibrosis-Promoting Airway Transcriptome Profile-Study in Asthma Patients". en. In: *International Journal of Molecular Sciences* 22.3 (Jan. 2021), p. 998. ISSN: 1422-0067. DOI: 10.3390/ijms22030998. URL: <https://www.mdpi.com/1422-0067/22/3/998> (visited on 10/22/2024).
- [95] Ali Doryab and Otmar Schmid. "Bioactive Cell-Derived ECM Scaffold Forms a Unique Cellular Microenvironment for Lung Tissue Engineering". en. In: *Biomedicines* 10.8 (July 2022), p. 1791. ISSN: 2227-9059. DOI: 10.3390/biomedicines10081791. URL: <https://www.mdpi.com/2227-9059/10/8/1791> (visited on 10/22/2024).
- [96] D. Schultheiss et al. "Biologische vaskularisierte Matrix (BioVaM)". de. In: *Urologe [A]* 43.10 (Oct. 2004), pp. 1223–1228. ISSN: 1433-0563. DOI: 10.1007/s00120-004-0702-7. URL: <https://doi.org/10.1007/s00120-004-0702-7> (visited on 04/11/2024).
- [97] Troy D. Rogers et al. "Regional Differences in Mucociliary Clearance in the Upper and Lower Airways". In: *Frontiers in Physiology* 13 (Mar. 2022), p. 842592. ISSN: 1664-042X. DOI: 10.3389/fphys.2022.842592. URL: <https://www.frontiersin.org/articles/10.3389/fphys.2022.842592/full> (visited on 10/14/2024).
- [98] W. Michael Foster. "Mucociliary Function". en. In: *Comparative Biology of the Normal Lung*. Elsevier, 2015, pp. 561–579. ISBN: 978-0-12-404577-4. DOI: 10.1016/B978-0-12-404577-4.00029-1. URL: <https://linkinghub.elsevier.com/retrieve/pii/B9780124045774000291> (visited on 10/14/2024).
- [99] Mereena George Ushakumary, Matthew Riccetti, and Anne-Karina T. Perl. "Resident Interstitial Lung Fibroblasts and their Role in Alveolar Stem Cell Niche Development, Homeostasis, Injury, and Regeneration". en. In: *Stem Cells Translational Medicine* 10.7 (July 2021), pp. 1021–1032. ISSN: 2157-6564, 2157-6580. DOI: 10.1002/sctm.20-0526. URL: <https://academic.oup.com/stcltm/article/10/7/1021/6516487> (visited on 05/30/2024).
- [100] Puja Jain et al. "Reconstruction of Ultra-thin Alveolar-capillary Basement Membrane Mimics". en. In: *Advanced Biology* 5.8 (2021), p. 2000427. ISSN: 2701-0198. DOI: 10.1002/adbi.202000427. URL: <https://onlinelibrary.wiley.com/doi/abs/10.1002/adbi.202000427> (visited on 04/11/2024).

- [101] Herbert B. Schiller et al. "The Human Lung Cell Atlas: A High-Resolution Reference Map of the Human Lung in Health and Disease". en. In: *Am J Respir Cell Mol Biol* 61.1 (July 2019), pp. 31–41. ISSN: 1044-1549, 1535-4989. DOI: 10.1165/rcmb.2018-0416TR. URL: <https://www.atsjournals.org/doi/10.1165/rcmb.2018-0416TR> (visited on 05/30/2024).
- [102] Matthias Ochs and Ewald R. Weibel. "Functional Design of the Human Lung for Gas Exchange". In: *Fishman's Pulmonary Diseases and Disorders*, 5e. Ed. by Michael A. Grippi et al. New York, NY: McGraw-Hill Education, 2015. URL: accessmedicine.mhmedical.com/content.aspx?aid=1122354263 (visited on 05/30/2024).
- [103] Elizabeth J. Kovacs. "Wheater's Functional Histology: A Text and Colour Atlas". en. In: *Archives of Pathology & Laboratory Medicine* 125.5 (May 2001), pp. 708–708. ISSN: 1543-2165, 0003-9985. DOI: 10.5858/2001-125-708b-WFHATA. URL: <https://meridian.allenpress.com/aplm/article/125/5/708/453064/Wheater-s-Functional-Histology-A-Text-and-Colour> (visited on 05/30/2024).
- [104] Cornelia Wiese-Rischke, Rasika S. Murkar, and Heike Walles. "Biological Models of the Lower Human Airways—Challenges and Special Requirements of Human 3D Barrier Models for Biomedical Research". en. In: *Pharmaceutics* 13.12 (Dec. 2021), p. 2115. ISSN: 1999-4923. DOI: 10.3390/pharmaceutics13122115. URL: <https://www.mdpi.com/1999-4923/13/12/2115> (visited on 04/18/2024).
- [105] Oliver Brookes et al. "Co-culture of type I and type II pneumocytes as a model of alveolar epithelium". en. In: *PLoS ONE* 16.9 (Sept. 2021). Ed. by Wei Shi, e0248798. ISSN: 1932-6203. DOI: 10.1371/journal.pone.0248798. URL: <https://dx.plos.org/10.1371/journal.pone.0248798> (visited on 09/05/2024).
- [106] Michael Lieber, George Todaro, Barry Smith, Andras Szakal, and Walter Nelson-Rees. "A continuous tumor-cell line from a human lung carcinoma with properties of type II alveolar epithelial cells". en. In: *Intl Journal of Cancer* 17.1 (Jan. 1976), pp. 62–70. ISSN: 0020-7136, 1097-0215. DOI: 10.1002/ijc.2910170110. URL: <https://onlinelibrary.wiley.com/doi/10.1002/ijc.2910170110> (visited on 04/18/2024).
- [107] C. Ehrhardt et al. "Drug Absorption by the Respiratory Mucosa: Cell Culture Models and Particulate Drug Carriers". en. In: *Journal of Aerosol Medicine* 15.2 (June 2002), pp. 131–139. ISSN: 0894-2684, 1557-9026. DOI: 10.1089/089426802320282257. URL: <http://www.liebertpub.com/doi/10.1089/089426802320282257> (visited on 04/18/2024).
- [108] Werner E. G. Müller et al. "Morphogenetic (Mucin Expression) as Well as Potential Anti-Corona Viral Activity of the Marine Secondary Metabolite Polyphosphate on A549 Cells". en. In: *Marine Drugs* 18.12 (Dec. 2020), p. 639. ISSN: 1660-3397. DOI: 10.3390/md18120639. URL: <https://www.mdpi.com/1660-3397/18/12/639> (visited on 11/02/2024).

- [109] G E Morris et al. "A novel electrospun biphasic scaffold provides optimal three-dimensional topography for *in vitro* co-culture of airway epithelial and fibroblast cells". In: *Biofabrication* 6.3 (June 2014), p. 035014. ISSN: 1758-5082, 1758-5090. DOI: 10.1088/1758-5082/6/3/035014. URL: <https://iopscience.iop.org/article/10.1088/1758-5082/6/3/035014> (visited on 10/14/2024).
- [110] Aadil Kaisani et al. "Branching morphogenesis of immortalized human bronchial epithelial cells in three-dimensional culture". en. In: *Differentiation* 87.3-4 (Mar. 2014), pp. 119–126. ISSN: 03014681. DOI: 10.1016/j.diff.2014.02.003. URL: <https://linkinghub.elsevier.com/retrieve/pii/S0301468114000073> (visited on 10/14/2024).
- [111] Peter Gehr, Marianne Bachofen, and Ewald R. Weibel. "The normal human lung: ultrastructure and morphometric estimation of diffusion capacity". en. In: *Respiration Physiology* 32.2 (Feb. 1978), pp. 121–140. ISSN: 00345687. DOI: 10.1016/0034-5687(78)90104-4. URL: <https://linkinghub.elsevier.com/retrieve/pii/0034568778901044> (visited on 05/30/2024).
- [112] Anna Kuehn. "Human alveolar epithelial cells expressing tight junctions to model the air-blood barrier". en. In: *ALTEX* (2016). ISSN: 1868596X. DOI: 10.14573/altex.1511131. URL: <http://www.altex.org/index.php/altex/article/view/155> (visited on 04/11/2024).
- [113] Carlos F. Guimarães, Luca Gasperini, Alexandra P. Marques, and Rui L. Reis. "The stiffness of living tissues and its implications for tissue engineering". en. In: *Nat Rev Mater* 5.5 (Feb. 2020), pp. 351–370. ISSN: 2058-8437. DOI: 10.1038/s41578-019-0169-1. URL: <https://www.nature.com/articles/s41578-019-0169-1> (visited on 05/29/2024).
- [114] Kristine M. Abo et al. "Human iPSC-derived alveolar and airway epithelial cells can be cultured at air-liquid interface and express SARS-CoV-2 host factors". eng. In: *bioRxiv* (June 2020), p. 2020.06.03.132639. ISSN: 2692-8205. DOI: 10.1101/2020.06.03.132639.
- [115] Fuyu Duan et al. "Modeling COVID-19 with Human Pluripotent Stem Cell-Derived Cells Reveals Synergistic Effects of Anti-inflammatory Macrophages with ACE2 Inhibition Against SARS-CoV-2". eng. In: *Res Sq* (Sept. 2020), rs.3.rs-62758. ISSN: 2693-5015. DOI: 10.21203/rs.3.rs-62758/v1.
- [116] Yuling Han et al. "Identification of SARS-CoV-2 inhibitors using lung and colonic organoids". eng. In: *Nature* 589.7841 (Jan. 2021), pp. 270–275. ISSN: 1476-4687. DOI: 10.1038/s41586-020-2901-9.
- [117] Hynda K Kleinman, Deborah Philp, and Matthew P Hoffman. "Role of the extracellular matrix in morphogenesis". en. In: *Current Opinion in Biotechnology* 14.5 (Oct. 2003), pp. 526–532. ISSN: 09581669. DOI: 10.1016/j.copbio.2003.08.002. URL: <https://linkinghub.elsevier.com/retrieve/pii/S0958166903001186> (visited on 08/19/2024).

- [118] Matthias P. Lutolf, Penney M. Gilbert, and Helen M. Blau. “Designing materials to direct stem-cell fate”. en. In: *Nature* 462.7272 (Nov. 2009), pp. 433–441. ISSN: 0028-0836, 1476-4687. DOI: 10.1038/nature08602. URL: <https://www.nature.com/articles/nature08602> (visited on 08/19/2024).
- [119] M. Hermanns, R. Unger, K. Kehe, K. Peters, and C. Kirkpatrick. “Lung epithelial cell lines in coculture with human pulmonary microvascular endothelial cells: development of an alveolo-capillary barrier in vitro”. In: *Laboratory Investigation* 84 (2004), pp. 736–752. DOI: 10.1038/labinvest.3700081.
- [120] Ana Costa, C. de Souza Carvalho-Wodarz, V. Seabra, B. Sarmento, and C. Lehr. “Triple co-culture of human alveolar epithelium, endothelium and macrophages for studying the interaction of nanocarriers with the air-blood barrier.” In: *Acta biomaterialia* 91 (2019), pp. 235–247. DOI: 10.1016/j.actbio.2019.04.037.
- [121] Puja Jain et al. “Peptide-Functionalized Electrospun Meshes for the Physiological Cultivation of Pulmonary Alveolar Capillary Barrier Models in a 3D-Printed Micro-Bioreactor”. en. In: *ACS Biomaterials Science & Engineering* 9.8 (Aug. 2023), pp. 4878–4892. ISSN: 2373-9878, 2373-9878. DOI: 10.1021/acsbomaterials.3c00047. URL: <https://pubs.acs.org/doi/10.1021/acsbomaterials.3c00047> (visited on 11/02/2024).
- [122] Ali Doryab et al. “A Bioinspired in vitro Lung Model to Study Particokinetics of Nano-/Microparticles Under Cyclic Stretch and Air-Liquid Interface Conditions”. In: *Frontiers in Bioengineering and Biotechnology* 9 (Jan. 2021), p. 616830. ISSN: 2296-4185. DOI: 10.3389/fbioe.2021.616830. URL: <https://www.frontiersin.org/articles/10.3389/fbioe.2021.616830/full> (visited on 11/02/2024).
- [123] A. Mikos and N. Peppas. “Measurement of the surface tension of mucin solutions”. In: *International Journal of Pharmaceutics* 53 (1989), pp. 1–5. DOI: 10.1016/0378-5173(89)90354-2.
- [124] Md. Anwarul Hasan, C. Lange, and M. King. “Effect of artificial mucus properties on the characteristics of airborne bioaerosol droplets generated during simulated coughing”. In: *Journal of Non-newtonian Fluid Mechanics* 165 (2010), pp. 1431–1441. DOI: 10.1016/J.JNNFM.2010.07.005.
- [125] D. Gaver, R. Samsel, and J. Solway. “Effects of surface tension and viscosity on airway reopening.” In: *Journal of applied physiology* 69 1 (1990), pp. 74–85. DOI: 10.1152/JAPPL.1990.69.1.74.
- [126] Rania Hamed, Rania Hamed, and Jennifer Fiegel. “Synthetic tracheal mucus with native rheological and surface tension properties.” In: *Journal of biomedical materials research. Part A* 102 6 (2014), pp. 1788–98. DOI: 10.1002/jbm.a.34851.
- [127] Rui Wang, Jiahui Chen, Yuta Hozumi, Changchuan Yin, and Guo-Wei Wei. “Decoding Asymptomatic COVID-19 Infection and Transmission”. eng. In: *J Phys Chem Lett* 11.23 (Dec. 2020), pp. 10007–10015. ISSN: 1948-7185. DOI: 10.1021/acs.jpcclett.0c02765.

- [128] Adrián Jaén-Gil et al. “An automated on-line turbulent flow liquid-chromatography technology coupled to a high resolution mass spectrometer LTQ-Orbitrap for suspect screening of antibiotic transformation products during microalgae wastewater treatment”. eng. In: *J Chromatogr A* 1568 (Sept. 2018), pp. 57–68. ISSN: 1873-3778. DOI: 10.1016/j.chroma.2018.06.027.
- [129] Constantine D. Troupes et al. “Role of STIM1 (Stromal Interaction Molecule 1) in Hypertrophy-Related Contractile Dysfunction”. eng. In: *Circ Res* 121.2 (July 2017), pp. 125–136. ISSN: 1524-4571. DOI: 10.1161/CIRCRESAHA.117.311094.
- [130] Sangeeta N. Bhatia and Donald E. Ingber. “Microfluidic organs-on-chips”. eng. In: *Nat Biotechnol* 32.8 (Aug. 2014), pp. 760–772. ISSN: 1546-1696. DOI: 10.1038/nbt.2989.
- [131] Courtney Tindle et al. *Adult Stem Cell-derived Complete Lung Organoid Models Emulate Lung Disease in COVID-19*. en. Oct. 2020. DOI: 10.1101/2020.10.17.344002. URL: <http://biorxiv.org/lookup/doi/10.1101/2020.10.17.344002> (visited on 07/15/2024).

I List of Abbreviations and Notations

Acronym	Meaning
°C	Degree Celcius Temperature
µm	Micrometer
2D	Two Dimensional
3D	Three Dimensional
ALI	Air Liftt Culture
APS	Ammonium Persulfate
BM	Basement Membrane
cm/s	Centimeter Per Seconds
δ	Loss angle / phase shift
DAB	3,3' - Diaminobenzidin
DAPI	4' ,6- Diamidin – 2 - Phenlindol
DMEM	Dulbecco'S Modified Eagle Medium
DMSO	Dimethyl Sulfoxide
ECM	Extracellularmatrix
EZM	Extrazelluläre Matrix
EDTA	Ethylenediamintetraacetate
FBS	Fetal Bovine Sera
FITC	Fluorescein Isothiocyanate
FITC	Fluoresceinisothiocyanat
FN	Fibronectin
Gpa	Gigapascals
G'	Elastic Modulus
G''	Loss Modulus
$G^*(\omega)$	Complex Modulus
γ_0	Strain amplitudes
h	Hours
hEC	Human Primary Endothelial Cells
HFP	(1,1,1,3,3,3-Hexafluor-2-Propanol)
HPSCs	Hematopoetic Stem Cells
HRP	Horseradish Peroxidase
huAEC	Human Airway Epithelial Cells
IF	Immunofluorescence
IHC	Immune-Histo-Chemistry

Acronym	Meaning
iPSCs	Induced Pluripotent Stem Cells
kPa	Kilopascals
LbFb	Primary Lung Biopsy Derived Human Fibroblasts
MEM	Modifies Eagle'S Medium
Mpa	Megapascals
NaPyr	Sodium Pyruvate
nm	Nanometer
η'	Dynamic viscosity
$\eta^*(\omega)$	Complex Viscosity
PA	Polyamide
Papp	Apparent Permeability
PCL	Poly-(ϵ -Caprolactone)
PET	Poly-Ethylene-Teraphthalate
pFb	Primary Human Dermal Fibroblasts
PS	Pencillin-Streptomycin
PTMC	Poly(Trimethylene Carbonate
RPMI	Rosswell Park Memorial Institute
RT	Room Temperature
SDS	Sodium Dodecyl Sulfate
SIS-Muc	Small Intestinal Submucosa With Mucosa
ST	Surface Tension
TBS	Tris-Buffered Saline
TBST	Tris-Buffered Saline With Tween20
TEMED	Tetramethylethylenediamine
TRITC	Tetramethylrhodamine
VEGF165	Vascular Endothelial Growth Factor-165
ZO-1	Zona-Occludins-1

II List of Figures

1.1 Typical tissue architecture for the human respiratory tract	3
2.1 Summarized co-culture models establishment timeline for synthetic scaffold-based models [6].	49
3.1 SEM images of the polymeric scaffold structures; pure PCL (A,B), PCL:PTMC 50:50 (C,D), PCL:PTMC 70:30 (E,F), PA (G,H) [6].	65
3.2 3D airway models using Calu-3 cells and human primary fibroblasts cultivated over 4 weeks <i>in vitro</i> on SIS-Muc scaffold (A- D) and PET Thincerts® membranes (E-J) [6].	70
3.3 Distinct multi-layering patterns and mucus formation in co-cultured A549 and Calu3 tissue models on different scaffolds are shown by alcian blue staining [6].	71
3.4 Lower airway models on PET membrane: coculture of A549-pFb: showing multilayering [6].	72
3.5 Mattek EPIAlveolar™ based models on PET membrane coculture of huAEC-LbFb-hEC: showing multilayering, as well as cellular crosstalk between epithelial as well as fibroblasts and no endothelial cell layer, be found on the basal side of the membrane [6].	74
3.6 Comparison between cellular attachment behaviour for PCL:PTMC 50:50 and PCL:PTMC 70:30 membrane models. (A-D) PCL:PTMC 70:30-based models. (E-J) PCL:PTMC 50:50-based models [6].	76
3.7 Immunohistochemical tissue characterisation against CD31 endothelial cell marker for triple culture models on PCL:PTMC 70:30 [6].	77
3.8 Characterisation of triple cultured tissue models (huAEC-hEC-LbFb) on PCL:PTMC 50:50 [6]	78
3.9 ZO-1 and Pan-Cytokeratin Staining in huAEC-LbFb-hEC Co-Cultures on PCL:PTMC 70:30 and PCL:PTMC 50:50 scaffolds [6].	79
3.10 Migration behaviour of endothelial cells in PA membrane co-culture models, analysed via CD31 staining, reveals differential migration under two cell seeding sequences.	80
3.11 Comparison of apparent permeability for electrospun PCL, PTMC membrane-based <i>in vitro</i> tissue models	83

3.12 Comparison of apparent permeability for electrospun PA membrane and PET-based <i>in vitro</i> tissue models	84
3.13 Summarised comparison of tissue models on synthetic scaffold materials: results in triple cultures with native fibroblasts and endothelial-epithelial co-cultures. Figure partially adapted using Biorender.com [6]	86
3.14 Amplitude sweep analysis for mucus sample extracted from 17× SIS-muc Calu-3 - pFb models at 4 weeks using the 500 μ l PBS- method. .	88
3.15 Frequency sweep analysis for mucus sample extracted from 17× SIS-muc Calu-3 - pFb models at 4 weeks using the 500 μ l PBS- method. .	90
3.16 Loss angle (δ) and dynamic viscosity η' calculated for mucus sample extracted from 17x SIS-muc Calu-3 - pFb models at 4 weeks using the 500 μ l PBS- method.	92
3.17 Surface tension measurement method using Force tensiometer. . . .	94
3.18 ST value analysis strategy represents data selection of only repeated cyclic measurements.	95
3.19 Measured surface tension values using indirect method for mucus samples and lung lavage	96

III List of supplementary figures

List of Supplementary Figures

7.1 PA based 3D *in vitro* co-culture models of hEC-huAEC-LbFb, showing negative control staining for IHC and IF done against CD31 endothelial marker. Negative control staining was performed using primary antibody specific host serum, here IgG mouse in the same concentration of primary antibody CD31. No positive signals were present in case of both IHC (brown) and IF (green fluorescence conjugated) stainings as seen in figure A and B respc.. . . . 127

7.2 Data selection and analysis after multiple ST measurements for mucus samples from *in vitro* tissue models at weeks 1, 2, 3 and 4. Table highlights the selected data values measured for Surface tension. Only the values corresponding to the repetitive cycles measurements are selected as depicted in fig. 3.18 (A) 128

IV List of Tables

1.1 Qualitative comparison between PCL and PTMC synthetic polymers based on their mechanical properties [6, 33, 34]	11
2.1 Tissue & cellular materials	28
2.2 Cells and tissue culture mediums	28
2.3 Cell and tissue culture supplements	29
2.4 Biological and Chemical substances	29
2.4 Biological and Chemical substances	30
2.4 Biological and Chemical substances	31
2.4 Biological and Chemical substances	32
2.5 Enzyme & substrate solutions	32
2.6 Reference biomaterials for synthetic scaffold	33
2.7 Primary and secondary antibodies	34
2.8 Analytical kits and components	36
2.9 Analytical solutions and buffer compositions for various applications	36
2.9 Analytical solutions and buffer compositions for various applications	37
2.10 Equipments	38
2.10 Equipments	39
2.11 Softwares	39
2.12 Lab consumables	39
2.13 Cells or cell line-specific culture medium composition	45
3.1 Calculated Young's modulus of elasticity and tensile strength for each synthetic electrospun membrane variant	67
3.2 Overview of biological and polymeric scaffolds for culturing different lung tissue locations. Upper lung location comprised of trachea/bronchi (conducting airways) and lower lung location consisting of terminal bronchioles and Alveolar locations (gas exchange area) [6]	68
3.3 Differences in mucus formation, cellular multi-layering, and ZO-1 expression in the airway models using standard cell lines for upper and lower respiratory tract [6].	72

Declaration of Honor

I hereby declare that I produced this thesis without prohibited external assistance and that none other than the listed references and tools have been used.

In the case of co-authorship, especially in the context of a cumulative dissertation, the own contribution is correctly and completely stated. I did not make use of any commercial consultant concerning graduation. A third party did not receive any non-monetary perquisites neither directly nor indirectly for activities which are connected with the contents of the presented thesis. All sources of information are clearly marked, including my own publications.

In particular I have not consciously:

- Fabricated data or rejected undesired results
- Misused statistical methods with the aim of drawing other conclusions than those warranted by the available data
- Plagiarized data or publications
- Presented the results of other researchers in a distorted way

I do know that violations of copyright may lead to injunction and damage claims of the author and also to prosecution by the law enforcement authorities.

I hereby agree that the thesis may need to be reviewed with an electronic data processing for plagiarism.

This work has not yet been submitted as a doctoral thesis in the same or a similar form in Germany or in any other country. It has not yet been published as a whole.

Place:

Datum:

.....

(Signature)

Declaration on criminal acts

I hereby declare that I have not been convicted of, or am not a defendant, or charged with, any criminal offense involving science.

Ich erkläre hiermit, nicht wegen einer Straftat mit Wissenschaftsbezug verurteilt worden zu sein oder wegen einer solchen Straftat Beschuldigter oder Beschuldigte, Angeklagter oder Angeklagte zu sein.

.....
(Place, Date on application for the opening of the doctoral procedure)

Place:

Datum:

.....
(Name, Surname, Signature)

List of Publications

1. Wiese-Rischke, C.; **Murkar, R. S.**; Walles, H. (2021). Biological Models of the Lower Human Airways-Challenges and Special Requirements of Human 3D Barrier Models for Biomedical Research. *Pharmaceutics*, 13(12), 2115. <https://doi.org/10.3390/pharmaceutics13122115>
2. **Murkar, R.**; von Heckel, C.; Walles, H.; Moch, T.B.; Arens, C.; Davaris, N.; Weber, A.; Zuschmitter, W.; Baumann, S.; Reinhardt, J.; et al. Establishment of a Human Immunocompetent 3D Tissue Model to Enable the Long-Term Examination of Biofilm–Tissue Interactions. *Bioengineering* 2024, 11, 187. <https://doi.org/10.3390/bioengineering11020187>
3. Spoddig, V. J.; Walles, T.; Walles, H.; **Murkar, R.** Entwicklung eines *in vitro* 3D – Modells zur Testung von Gewebereaktion auf Implantatabrieb (V-151). Kongress: 33. Jahrestagung der Deutschen Gesellschaft für Thoraxchirurgie Datum/Ort: 18 . – 20 . September 2024 , Magdeburg. Brustwandchirurgie (S93), Thieme ZBC 2024 ; 2024 : S85 – S131. DOI 10.1055/s-0044-1788103, <https://www.thieme-connect.de/products/ejournals/conferencepdf/132054/10.1055/s-00000104.pdf>
4. **Murkar, R.**; Wiese-Rischke, C.; Weigel, T.; Kopp, S.; and Walles, H;. Developing human upper, lower, and deep lung airway models: combining different scaffolds and developing complex co-cultures. *Journal of Tissue Engineering*. 2025;16. doi:10.1177/20417314241299076.
5. Marchal, S.; Dittrich, A.; Vogel, K.; Fickenscher, L.; Cortés-Sánchez, L. J.; Kahlert, S.; **Murkar, R.**; Brunner-Weinzierl, M.; Grimm, D. and Krüger, M. Random Positioning Has a Temporary Effect Only on Proliferating Monocytes' Functionality and Plasticity. *MDPI Journal of Molecular Sciences*. (**Submitted**)
6. Spoddig, V. J.; Walles, H.; **Murkar, R.**. Hydrogel based 3D invitro foreign body reaction assay to test implant abrasion reaction to ceramic, steel , titanium implant particles materials. **Ongoing Publication**